Università degli Studi di Firenze
European Laboratory for Non-Linear Spectroscopy (LENS)
Corso di Dottorato in Atomic and Molecular Photonics

Hybrid optomechanical states in the quantum motion of a levitated nanosphere

Candidate:
Andrea Ranfagni

Supervisor
Prof. Francesco Marin

---

ciclo XXXV, 2019-2022

To my family

To Francesca

abstract

Trapping and levitation of micrometric objects in strongly focused light beams (optical tweezers) was introduced in the pioneering works by Arthur Ashkin in the early 1970s, and the major impact of such techniques in a multidisciplinary environment earned him the Nobel Prize in Physics 2018. In most applications, optical trapping occurs in a strongly damping background.

The idea of operating in a high vacuum, thus reducing the interaction with the environment, and bringing levitating and oscillating nano-particles into the quantum regime was boosted about 10 years ago and has since developed into a fruitful research topic. Optically levitating nanoparticles in high vacuum offer a quite natural platform for the study of quantum mechanical features in all three spatial dimensions and the achievement of quantum coherent control of their motion, with applications ranging from quantum foundations and information processing to directional quantum sensing.

In this thesis we have demonstrated the experimental realization of a quantum platform based on a levitating silica nanoparticle coupled to a mode of a high finesse optical cavity in a room temperature environment. The optical potential experienced by the nano-particle is proportional to the light intensity. As a consequence, its oscillatory motion is characterized by a lower frequency along the tweezer propagation axis, where the characteristic length is the Rayleigh range, with respect to the transverse plane, where the characteristic length is the beam waist. The two-dimensional motion on the plane orthogonal to the tweezer axis and the optical cavity mode define an optomechanical system with three degrees of freedom.

With the protocol developed at the early stage of the doctoral work, based on the transfer of a levitated particle between two optical tweezers, we have been able to systematically levitate the particle in high vacuum on the axis of a high Finesse optical cavity and observe strong non classical signatures in the motional spectrum. Thanks to the coherent scattering setup, the oscillatory motion was strongly coupled to the cavity field thus leading to the observation of the hybrid optomechanical states, whose signature is a double avoided crossing between the eigenfrequencies of the three-body system.

In high vacuum, where the mechanical oscillator is weakly coupled to the environment, the energy flows coherently between the optomechanical components and the collective excitations are described in terms of polaritonic modes. Here we have explored the two dimensional motion of the nanoparticle close to its minimum uncertainty state, characterised by peculiar non classical features. We have reached

the mean phononic occupation number along the *coldest* motional direction below unity, thus achieving the 1D ground state cooling. Rotating the polarization of the trapping beam with respect to the cavity optical axis, we have strongly cooled the 2D motion achieving an effective occupancy below 1.5 along any motional direction. Moreover, the strongly broadened mechanical transfer function has allowed the observation of the quantum asymmetry on a bandwidth larger than the cavity linewidth, thus resolving the cavity mediated quantum back action noise, showing a distinctive modification due to the cavity mediated interference between the two mechanical oscillators.

Acknowledgements

Special thanks go to my academic Supervisor **Prof. Francesco Marin**, in whose laboratory I had the privilege and pleasure of working in these three years. I am deeply grateful for the support and guidance provided me throughout my dissertation.

Many thanks go to **Paolo Vezio**, **Francesco Marino**, **Massimo Calamai** and **Avishek Chowdhury**, with whom I shared a significant portion of the last three years.

For a period of six months I was a guest in the group conducted by **Professor Nikolai Kiesel** at the University of Wien. There I got to work under the direction of Nikolai and **Mario Arnolfo Ciampini**, working alongside **Jakob Rieser** in a stimulating environment. My thanks go to them too.

I am also grateful to **Professor Peter Barker** who, like professor Kiesel, reviewed the thesis work.

Outside of Unifi, I am grateful to my family that has supported me from the start. My special thanks go to **Francesca Pulcinelli**, whose presence has been fundamental along the path. I am deeply grateful to her family, that has genuinely supported me.

Contents

List of Figures

1 Introduction

According to Newtonian laws, the motion of an object is fully predicted if its motional state is known at a certain time. The classical theory describes a deterministic world, where every phenomenon can be described with infinite precision. Since the late 19th century, its application together with the classical theory of electromegnetism (James Clerk Maxwell, 1865) failed to explain phenomena such as the black body radiation (ultraviolet catastrophe), the atomic stability (the Rutherford planetary atom) and cutting edge experimental observations as the photoelectric effect observed by H.Hertz or the X-ray scattering pattern studied by Compton. These discrepancies led to the fundation of the quantum theory between 1925 and 1930. According to it, a consistent description of matter on the microscopic scale is provided assuming that both radiation and matter could be described as either a particle or a wave. Such counter intuitive interpretation of the nature, formalized with the Heisenberg uncertainty principle, depicts a world where the deterministic trajectories of objects give way to the deterministic evolution of a probability density function, that describes the state of the system. The point is that the classical theory, which is a good approximation for the macroscopic world, fails on the atomic scales, where the quantum theory gives a good understanding. However, the two theories have not been continuously merged at present.

In this context, the field of optomechanics explores the nature at halfway between the macroscopic and microscopic scale. Here the radiation field interacts with a macroscopic mechanical oscillator to control its motion at the level where non classical effects are unveiled. In pioneering experiments [9, 10] it was shown that the radiation pressure force could be exploited to either damp or excite the mechanical motion of an harmonically suspended mirror. Thence, experiments showing mechanical control over masses ranging from the gram to the zeptogram have been shown. The engineering of these macroscopic mechanical oscillators has played a fundamental role and technical advances have allowed to fabricate a large variety of optomechanical devices. An ubiquitous issue that an experimentalist faces with this kind of devices is related to how well they can be decoupled from the external environment. In fact, quantum optomechanics is a branch of quantum statistical mechanics: here the probabilistic interpretation of the mechanical motion is not only related to the quantum properties of the oscillator, but also to the - necessarily - incomplete knowledge of the environment state which can be described only by means of statistical tools. As long as the oscillator is bound

to some kind of mechanical support, cryogeny is required to limit the amount the energy that enters the system from the environment, inducing decoherence in the mechanical motion. Here comes into play optical levitation.

Trapping and levitation of micrometric objects in strongly focused light beams (optical tweezers) was introduced in the pioneering works by Arthur Ashkin in the early 1970s [2], and the major impact of such techniques in a multidisciplinary environment earned him the Nobel Prize in Physics 2018. In most applications, optical trapping occurs in a strongly damping background. The idea of operating in a high vacuum, thus reducing the interaction with the environment, and bringing levitating and oscillating nano-particles into the quantum regime was boosted about 10 years ago [12, 4, 54, 35] and has since developed into a fruitful research topic [43]. The optical potential experienced by the nano-particle is proportional to the light intensity. As a consequence, its oscillatory motion is characterized by a lower frequency along the tweezer propagation axis, where the characteristic length is the Rayleigh range, with respect to the transverse plane, where the characteristic length is the beam waist. Optically levitating nanoparticles in high vacuum offer a quite natural platform for the study of quantum mechanical features in all three spatial dimensions and the achievement of quantum coherent control of their motion, with applications ranging from quantum foundations and information processing to directional quantum sensing. The goal of cooling the oscillations down to a mean phononic occupation number below unity has been recently achieved: by means of electrostatic feedback cooling on charged particles the motion was frozen along the tweezer propagation axis [37, 63], while cavity cooling produced similar results for the oscillation along an axis in the transverse plane [15]. Recently [48] the simultaneous ground-state cooling of two mechanical modes of a levitated nanoparticle has been achieved in the weak coupling regime. Cavity cooling for levitated particles, initially implemented with standard optomechanical methods [32], has become much more efficient with the introduction of the coherent scattering technique [16, 75, 22] imported from atomic physics experiments [71].

This thesis reports on the development of an experimental platform in high vacuum composed of a levitated silica nanoparticle strongly coupled to the field of a high finesse optical cavity in a room-temperature environment. The optomechanical cooling, combined with the high decoupling from the thermal bath, has allowed the exploration of the two-dimensional quantum motion of the particle on the plane orthogonal to the optical tweezer propagation axis. The strong optomechanical coupling raises collective excitations, the polaritonic modes, which may

be used in the future as a tool for quantum information protocols.

The doctoral work is presented as follows:

Chapter 1 reviews the fundamental concepts of levitodynamics. Starting from the basics of optical trapping and the description of the Brownian motion of a levitated nanoparticle, the chapter continues with an introduction to cavity optomechanics, in particular focusing on the differences between weak and strong coupling regime and between the 1D and 2D mechanical systems. Here is introduced and analysed the concept of polaritonic modes for our optomechanical platform.

Chapter 2 reports on the transfer of a levitated nanoparticle between two optical tweezers, an experimental protocol that we have developed to prepare cavity optomechanics experiments. The core of the experimental setup - experimental vacuum chamber and the optical tweezer - is described.

In the **3rd Chapter** is described the configuration used to perform the measurements. Here the properties of the optical cavity, of fundamental importance for the experiment, are reported together with the full analysis of the detection setup, necessary to resolve the mechanical motion at the quantum level.

Chapter 4 reports on the experimental observation of the 1D and 2D quantum motion of a levitated nanosphere. The full model that has been developed during the thesis, essential to catch the features of the optomechanical system, is described together with the experimental data. The main observations reported are:

- **hybrid optomechanical states in the classical regime**: we observe collective optomechanical excitations that raise in the strong coupling regime;
- **vectorial polaritons**: basically, the hybrid states in the quantum coherent regime, where the energy flows between the three oscillators (two mechanical - one optical) within the decoherence time;
- **1D ground state cooling in the strong coupling regime and quantum coherent regime**: we report on the observation of the mechanical motion with mean phononic occupation number below unity. Particular attention here is paid to the definition of phononic excitation

and a novel and general approach is introduced to quantify the motional energy;

- **spatial asymmetry of the dipole scattering heating rate**: we resolve the spatial anisotropy in the heating rate induced by the quantum shot noise of the trapping laser field that is scattered by the particle;
- **strong cooling of the motion in the plane**: we report here on the minimum motional energy achieved along the *warmest* motional direction on the 2-D plane;
- **quantum asymmetry in the strong coupling regime**: the basic concepts of sideband-asymmetry is here introduced for the weak optomechanical coupling regime and then extended in the case of strong coupling, whose peculiar features are both theoretically and experimentally investigated.

The results shown in this thesis are reported in the following references:

- M.Calamai, A.Ranfagni, and F.Marin, *Transfer of a levitating nanoparticle between optical tweezers*, **AIP Advances 11, 025246 (2021)**;
- A. Ranfagni, P. Vezio, M. Calamai, A. Chowdhury, F.Marino, and F.Marin *Vectorial polaritons in the quantum motion of a levitated nanosphere*, **Nature Physics 17, 1120-1124 (2021)**.
- A. Ranfagni, K. Børkje, F.Marino, and F.Marin, *Two-dimensional quantum motion of a levitated nanosphere*, **Phys. Rev. Research 4, 033051 (2022)**.

2 Basics of cavity optomechanics with a levitated nanoparticle

I present an introduction to the the basic concepts of levitodynamics - optomechanics with levitated nanoparticles - starting from the optical trapping and continuing with the basics of cavity optomechanics. With these tools available, will follow an introductory analysis on hybrid light-mechanical states that raise when the optomechanical interaction is strong. In the end is introduced the concept of vectorial polariton for our platform, which is the central topic of the experimental work presented in this thesis.

2.1 Optical trapping

As observed in the pioneering work of Arthur Ashkin [2], a tightly focused light beam enables the confinement of the motion of a dielectric particle. If the dimension of the particle is much smaller than the optical wavelength - the Rayleigh regime - the physics is quite simple. Namely, the interaction of the dielectric with the trapping field is fully described by the complex polarizability:

$$\alpha(\omega) = 3\epsilon_0 V \frac{\epsilon(\omega) - 1}{\epsilon(\omega) + 2},$$

where ϵ_0 is the vacuum dielectric constant, V is the particle volume and $\epsilon(\omega)$ is the frequency dependent permittivity. It can be shown [46] that the overall optical force exerted on the particle is:

$$\langle \mathbf{F} \rangle = \frac{\mathrm{Re}[\alpha]}{4} \nabla E^2 + \frac{\mathrm{Im}[\alpha]}{2} E^2(\mathbf{r}) \nabla \Phi(\mathbf{r}),$$

where the electrical field is $\mathbf{E}(\mathbf{r}) = E(\mathbf{r}) e^{i\Phi(\mathbf{r})} \mathbf{n}$, with E the real amplitude. The first term describes a conservative force, responsible for the trapping. The second term, proportional to the imaginary part of the polarizability, describes the optical absorption. As the conservative force is proportional to the light intensity, the particle is pulled toward the optical focus, resulting in a spatial confinement.

For a Gaussian trapping beam and the particle close to intensity maximum (if compared to the waist and the Rayleigh length of the beam) the optical potential

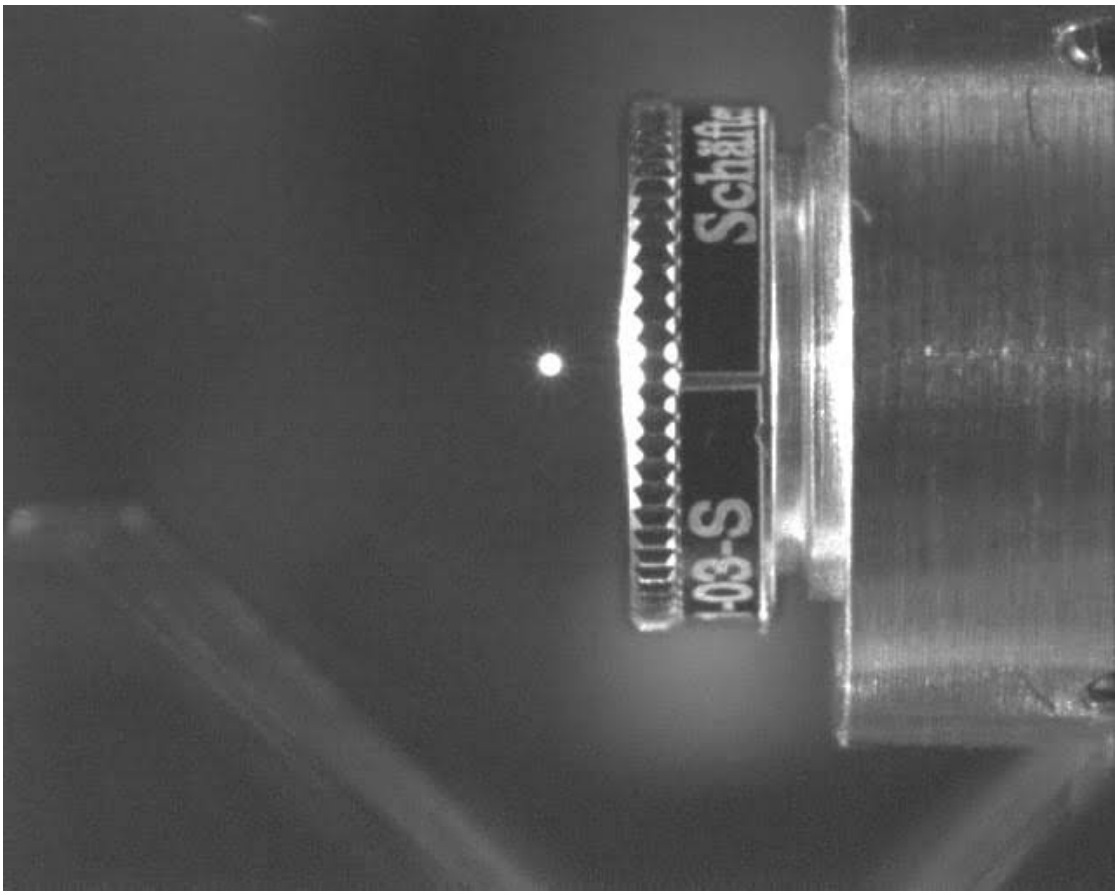

Figure 1: A particle trapped in the vacuum chamber of our lab by means of optical levitation.

can be Taylor expanded. At the first order, the trapping force reads:

$$F_j = -m\Omega_j^2 q_j, \qquad q_j \in x, y, z$$

i.e. it behaves as an harmonic restoring force. The resonance frequencies of the three dimensional oscillator are defined in terms of both the trapping beam and the particle properties. For a linearly polarized beam focused on a waist smaller than the wavelength, the shape of the waist at the focus is elliptical [46], elongated along the polarization axis. Defining z as the propagation axis of the beam and $W_{x(y)} = W_\mathrm{t} A_{x(y)}$ the waist along the $x\,(y)$ direction, with the Rayleigh length $Z_\mathrm{R} = \pi W_\mathrm{t}^2/\lambda$, the frequencies read:

$$\begin{pmatrix}\Omega_x\\ \Omega_y\\ \Omega_z\end{pmatrix} = \sqrt{\frac{\epsilon_0 \epsilon_\mathrm{c} \epsilon_\mathrm{tw}^2}{2\rho W_\mathrm{t}^2}} \begin{pmatrix}\sqrt{2}/A_x\\ \sqrt{2}/A_y\\ \lambda/\pi W_\mathrm{t}\end{pmatrix}$$

where $\epsilon_\mathrm{c} = \mathrm{Re}\,[\alpha]\,/\epsilon_0 V$, ρ is the particle density, $\epsilon_\mathrm{tw} = \sqrt{\frac{4P}{\pi\epsilon_0 c W_x W_y}}$ with P the optical power and c the light velocity.

Experimentally, to deliver a particle in the optical tweezer, we introduce dust of nanoparticles into pure nitrogen in a chamber with a tightly focused laser beam. The particles in the chamber undergo a Brownian motion because of their collisions with the molecules of the surrounding gas. As a particle approaches the beam waist, it loses energy because of the gas damping. If the thermal energy of the Brownian motion is smaller than the optical trap depth, the particle can be spatially confined. Figure (1) is a picture of a nanometric particle levitating in the optical potential in the vacuum chamber of our experimental setup.

2.2 Motion of a levitated nanoparticle

In general the particle evolution in non coherent, because of its interaction with the environment. Therefore the open dynamics of the oscillator, which can be modelled via the Langevin equations formalism, has to be analysed. In the configuration described above, the classical motion of the particle along any of the three spatial directions defined by the tweezer reads:

$$\ddot{q} + \gamma\dot{q} + m\Omega^2 q = F^\mathrm{th}/m, \tag{2.1}$$

where γ and F^{th} are respectively the damping and the stochastic force due to gas collisions. For an oscillator in thermal equilibrium with a bath at temperature T, the power spectral density (PSD) of the thermal force and the damping are related by the fluctuation dissipation theorem:

$$S_{FF}(\omega) = 2\gamma m k_{\mathrm{B}} T,$$

where k_{B} is the Boltzmann constant.

The quantum description of the macroscopic system is given quantising the oscillator degrees of freedom, i.e. setting $q \to \hat{q}$, where the usual commutation rule between position and momentum

$$[\hat{q}, \hat{p}] = i\hbar$$

holds.

The oscillator evolution is often represented in terms of the ladder operators, defined as

$$\hat{q} = q_{\mathrm{zpf}} \left(\hat{b} + \hat{b}^{\dagger} \right),$$

where $q_{\mathrm{zpf}} = \sqrt{\hbar / 2m\Omega}$ represents the quantum of oscillation. The equation (2.1) can be restated in its quantum version and, in the high Q limit ($\Omega/\gamma \gg 1$) reads:

$$\dot{\hat{b}} = (-i\Omega - \gamma/2)\, \hat{b} + \sqrt{\gamma} \hat{b}_{\mathrm{IN}}, \tag{2.2}$$

with the input white thermal noise that obeys:

$$\left\langle \hat{b}_{\mathrm{IN}}(t)\, \hat{b}^{\dagger}_{\mathrm{IN}}(t') \right\rangle = (\bar{n} + 1)\, \delta(t - t'),$$
$$\left\langle \hat{b}^{\dagger}_{\mathrm{IN}}(t)\, \hat{b}_{\mathrm{IN}}(t') \right\rangle = \bar{n} \delta(t - t'),$$

where $\bar{n}$ is the mean phononic occupation number at thermal equilibrium for the mode at frequency Ω defined by the Bose Einstein distribution:

$$\bar{n} = \frac{1}{e^{\frac{\hbar\Omega}{k_{\mathrm{B}}T}} - 1}.$$

The mechanical motion is often analysed in frequency space (when the system has stable stationary solutions). The quantum PSD (see Appendix A) of the

motion at the equilibrium reads:

$$S_{qq}(\omega) = q_{\mathrm{zpf}}^2 \gamma \left[|\chi_{\mathrm{m}}(\omega)|^2 \bar{n} + |\chi_{\mathrm{m}}(-\omega)|^2 (\bar{n}+1) \right],$$

where $\chi_{\mathrm{m}}(\omega) = 1/[i(\omega - \Omega) + \gamma/2]$ is the mechanical susceptibility.

It is newsworthy that the quantum PSD is asymmetric in the frequency, in contrast with the classical theory where the PSD of a real variable is always symmetric. The asymmetry here comes out from the fact that a quantum force is acting on the oscillator, driving transitions between the Fock states with probabilities depending upon the occupation number of the initial and final states. This feature will be further described in chapter 5. For now, it is sufficient to underline that in the classical, high temperature limit, $(\bar{n}+1)/\bar{n} \to 1$ and the asymmetry vanishes.

In the end, the variance of the noisy motion is obtained integrating the PSD:

$$\left\langle q^2 \right\rangle = q_{\mathrm{zpf}}^2 (2\bar{n} + 1). \tag{2.3}$$

In the quantum theory, the minimum RMS displacement for the oscillator is q_{zpf}, and in the high temperature limit the classical equipartition theorem is recovered:

$$m\Omega^2 \left\langle q^2 \right\rangle = k_{\mathrm{B}} T.$$

2.3 Cavity Optomechanics

As stated above, the dynamics of a levitated nanoparticle is equivalent (for small displacements) to the Brownian motion of a three dimensional quantum harmonic oscillator. The purpose of optomechanics consists in the full control of the mechanical motion by means of optical forces. In cavity optomechanics such forces are exerted via the momentum transfer between the cavity photons and the mechanical oscillator.

The basic theory of cavity optomechanics has been extensively studied and a complete overview is [3]. Here I'll just report the main concepts that serve as a preamble to the physics that has been explored during the thesis, which will be introduced in the next sections and extensively discussed along with the presentation of the results. Basically, the optomechanical dynamics is that of two coupled oscillators:

$$H/\hbar = \omega_{\mathrm{c}} \hat{a}_{\mathrm{c}}^\dagger \hat{a}_{\mathrm{c}} + \Omega \hat{b}^\dagger \hat{b} - g \hat{a}_{\mathrm{c}}^\dagger \hat{a}_{\mathrm{c}} \left(\hat{b} + \hat{b}^\dagger \right),$$

where $\hat{b}$ ($\hat{a}_{\mathrm{c}}$) is the ladder operator for the mechanical (optical) mode with frequency $\Omega(\omega_{\mathrm{c}})$ and g is the optomechanical coupling strength. In the linearised approximation, the cavity field is split into an average coherent ampltude $<\hat{a}_{\mathrm{c}}>$ and a fluctuating term $\hat{a}$, i.e. $\hat{a}_{\mathrm{c}} =<\hat{a}_{\mathrm{c}}>+\hat{a}$ (with $<\hat{a}>\in$ Re WLOG). Expressing the Hamiltonian in the frame rotating [1] at the laser frequency and retaining only the terms of the first order in the fluctuations:

$$H/\hbar = -\Delta\hat{a}^{\dagger}\hat{a} + \Omega\hat{b}^{\dagger}\hat{b} - g\left(\hat{a}+\hat{a}^{\dagger}\right)\left(\hat{b}+\hat{b}^{\dagger}\right),$$

where $\Delta = \omega_{\mathrm{l}} - \omega_{\mathrm{c}}$ is the difference between the laser (ω_{l}) and the cavity mode frequency. The evolution of the oscillator operators[2] in the Heisenberg picture, with the approximation of high quality oscillators, reads

$$\dot{\hat{a}} = (i\Delta - \kappa/2)\,\hat{a} + ig\left(\hat{b}+\hat{b}^{\dagger}\right) + \sqrt{\kappa}\hat{a}_{\mathrm{IN}}, \tag{2.4}$$

$$\dot{\hat{b}} = (-i\Omega - \gamma/2)\,\hat{b} + ig\left(\hat{a}+\hat{a}^{\dagger}\right) + \sqrt{\gamma}\hat{b}_{\mathrm{IN}}, \tag{2.5}$$

where $\gamma(\kappa)$ is the mechanical (optical) damping, and $\hat{b}_{\mathrm{IN}}$ ($\hat{a}_{\mathrm{IN}}$) is the noise term that drives the Brownian motion. This system of coupled equations enclose the whole physics of linear cavity optomechancs.

To find the stationary solutions, the equations can be readily solved in the Fourier domain where they represent a system of first order equations:

$$\tilde{a}(\omega) = \frac{1}{\kappa/2 - i(\omega+\Delta)}\left[ig\left(\tilde{b}(\omega)+\tilde{b}^{\dagger}(\omega)\right) + \sqrt{\kappa}\tilde{a}_{\mathrm{IN}}\right], \tag{2.6}$$

$$\tilde{b}(\omega) = \frac{1}{\gamma/2 - i(\omega-\Omega)}\left[ig\left(\tilde{a}(\omega)+\tilde{a}^{\dagger}(\omega)\right) + \sqrt{\gamma}\tilde{b}_{\mathrm{IN}}\right]. \tag{2.7}$$

These equations can be interpreted together with the interaction energy

$$H_{\mathrm{int}} = \hbar g\left(\hat{a}+\hat{a}^{\dagger}\right)\left(\hat{b}+\hat{b}^{\dagger}\right), \tag{2.8}$$

considering that for a high quality oscillator $\tilde{b}(\omega)$ is peaked at Ω (see Eq.(2.7)), while $\tilde{b}^{\dagger}(\omega)$ is peaked at $-\Omega$. In the good cavity regime ($\kappa \ll \Omega$) if $\Delta = -\Omega$

[1] Moving to the frame rotating at the frequency ω_{R} consists in the transformations: $\hat{a} \rightarrow \hat{a}^{\mathrm{R}}e^{-i\omega_{\mathrm{R}}t}$ and $H -> H^{\mathrm{R}} - \hbar\omega_{\mathrm{R}}\hat{a}^{\dagger\mathrm{R}}\hat{a}^{\mathrm{R}}$. For clarity the superscript R on the operators is dropped in the text

[2] The evolution of an operator $\hat{O}$, whose dynamic is set by the Hamiltonian $\hat{H}$, is $\dot{\hat{O}} = \frac{i}{\hbar}\left[\hat{H},\hat{O}\right]$

the cavity filtering couples $\hat{a}$ to $\hat{b}$ (see Eq.(2.6)), giving $\tilde{a}(\Omega) \simeq \frac{2ig}{\kappa}\tilde{b}(\Omega)$. In this case the resonant terms in the interaction energy Eq.(2.8) are those proportional to $\left(\hat{a}^\dagger\hat{b} + \hat{a}\hat{b}^\dagger\right)$. On the other hand, if $\Delta = \Omega$, $\hat{a}^\dagger \sim \hat{b}$ and the resonant interaction terms are proportional to $\left(\hat{a}^\dagger\hat{b}^\dagger + \hat{a}\hat{b}\right)$.

In the first case, the optical and mechanical oscillators exchange energy through the so called *beam splitter interaction*, which describes events where quanta of energy flow between the two oscillators. It describes the physics of optical cooling: the warm mechanical oscillator reaches the a stationary state at the equilibrium with a cold optical mode which, namely, acts as a reservoir. This kind of interaction is also suitable to set up quantum state transfer between light and mechanics.

The second term, called *two mode squeezing interaction*, is associated to events where photons and phonons are generated/annihilated in pairs. The optical and mechanical excitations could show, in principle, high correlations (squeezing). This kind of interaction is at the heart of the parametric amplification.

In case of optical resonance, the two terms are equally enhanced and the interaction is optimal for optomechanical displacement detection.

Experimentally, one can choose between these configurations setting the optical frequency.

2.3.1 Setting up the optomechanical interaction for a levitated nanoparticle

The optomechanical interaction is determined by several experimental parameters. It is always proportional to the coupling strength, g, whose value is determined by the basic physical mechanisms that couple optical and mechanical fluctuations.

Namely, the optomechanical interaction energy for a levitated nanoparticle raises from the coupling between the induced dipole, $\mathbf{d}$, and the optical field that polarizes the dielectric:

$$H_{\text{int}} = -\mathbf{d} \cdot \mathbf{E}(\mathbf{r}),$$

where here $\mathbf{E}$ is the total electrical field at the nanoparticle position. In the Rayleigh approximation, $\mathbf{d} = \alpha\mathbf{E}$ and the interaction term reads:

$$H_{\text{int}} = -\alpha E^2(\mathbf{r}).$$

In the experimental configuration the particle is trapped with an optical tweezer and placed on the cavity optical axis, where the total field is the sum of the tweezer

($\mathbf{E}_{\mathrm{tw}}$) and cavity ($\mathbf{E}_{\mathrm{c}}$) fields.

$$H_{\mathrm{int}} = -\alpha \left(E_{\mathrm{c}}^2 + 2\mathbf{E}_{\mathrm{c}}\mathbf{E}_{\mathrm{tw}} + E_{\mathrm{tw}}^2 \right).$$

A detailed analysis of these terms is reported in [22].

In a nutshell, these field operators must be evaluated at the particle position and only the terms containing the cavity field describe the cavity optomechanical interaction. Their Taylor expansion for small mechanical displacements around the equilibrium position gives different optomechanical terms:

- the **Dispersive coupling** raises from the term $-\alpha E_{\mathrm{c}}^2$, which can be expressed as

  $$H^{\mathrm{d}} = -\hbar\delta\omega\left(\mathbf{r}\right)\hat{a}^{\dagger}\hat{a},$$

  where $\delta\omega = \delta\omega_0 \left| f\left(\mathbf{r}\right)\right|^2$, with $\delta\omega_0 = \frac{\alpha\omega_{\mathrm{cav}}}{2V_{\mathrm{cav}}\epsilon_0}$, $f\left(\mathbf{r}\right)$ the spatial profile of the cavity mode with volume V_{cav}. The particle here acts as a dielectric perturbation of the cavity mode, shifting its resonance frequency by $\delta\omega\left(\mathbf{r}\right)$. Wishing to assess a physical picture of the coupling mechanism, the particle motion displaces the optical mode resonance, thus inducing fluctuations in the intracavity field. These in return, act back on the particle via radiation pressure.

  Taylor expanding the energy for the particle placed on the cavity axis, the linearised interaction Hamiltonian is:

  $$H^{\mathrm{d}} = \hbar g_{\mathrm{d}} \frac{\partial f^2}{\partial x^2} \left(\hat{a} + \hat{a}^{\dagger}\right)\left(\hat{b} + \hat{b}^{\dagger}\right),$$

  where $g_{\mathrm{d}} = \langle \hat{a}_{\mathrm{c}} \rangle \delta\omega_0 k x_{\mathrm{zpf}}$ is the dispersive coupling strength and $\hat{b}$ the ladder operator for the motion along the cavity axis (x). The coupling is proportional to the gradient of the field intensity profile and only the motion along the cavity axis is optomechanically coupled. The interaction is enhanced by the number of cavity photons.

- The **Coherent coupling** raises from the term $-\alpha\mathbf{E}_{\mathrm{cav}}\mathbf{E}_{\mathrm{tw}}$, that can be written as:

  $$H^{\mathrm{coh}} = -\hbar g_x \frac{\partial f}{\partial x}\frac{1}{k}\left(\hat{a} + \hat{a}^{\dagger}\right)\left(\hat{b} + \hat{b}^{\dagger}\right) + i g_z f\left(\mathbf{r}\right)\left(\hat{a} - \hat{a}^{\dagger}\right)\left(\hat{b}_z + \hat{b}_z^{\dagger}\right)$$

  where $g_x = E_{\mathrm{d}} k x_{\mathrm{zpf}}$, with $E_{\mathrm{d}} = \frac{\alpha\epsilon_{\mathrm{c}}\epsilon_{\mathrm{tw}}}{2\hbar}$ and $\epsilon_{\mathrm{c}} = \sqrt{\frac{\hbar\omega_{\mathrm{c}}}{2\epsilon_0 V_{\mathrm{c}}}}$. Here the particle acts

as an input mirror and the way that the photons scattered by the particle are filtered by the cavity determines the optomechanical interaction. This configuration has been recently exploited and introduced in optomechanics experiments [16, 75]. In the coherent scattering configuration both the motion along the cavity axis (x) and orthogonal to it (z) are naturally coupled to the field fluctuations. Since $f(x) \sim \sin(kx)$, the coupling is maximum at the node for the x motion and at the antinode for the z motion.

In our experimental configuration the particle is placed as close as possible to the node, exploiting the coherent scattering coupling. It should be noted that the average cavity photon number is nominally null. As such, technical limits related to classical fluctuations of the laser that would optomechanically couple to the particle motion are highly suppressed.

2.3.2 Noise terms driving the motion

As reported in Eq.(2.3) the particle motion never stops because of quantum constraints formalized in the Heisenberg uncertainty principle. The minimum rms displacement for our nanoparticle is on the order of $q_{\mathrm{zpf}} \sim 10^{-12}$ m.

Actually, there are several experimental/fundamental constraints that prevent the system from being so close to the quantum ground state. In fact, the particle is mechanically and optically coupled to external reservoirs, respectively via collisions and radiation pressure. The evolution of these external baths is random and, as such, randomness enters the particle dynamics washing away the motional coherence. In a quantum treatment, the action of a random force on the oscillator can be characterized through the heating rate, i.e. the rate at which - on average - the noise source contributes to the increase of the phononic occupation number of the oscillator. In other words, the mean phononic occupancy at the equilibrium is set by the ratio between the overall heating rate and the damping:

$$\bar{n}_{\mathrm{eq}} = \frac{\Gamma_{\mathrm{heat}}}{\Gamma_{\mathrm{damp}}}.$$

Here are reported the fundamental noise sources that drive the mechanical motion for the experimental configuration of our apparatus.

- **Thermal motion**: since the particle collides with the gas molecules of the thermal environment, its dynamics can be modelled via the Langevin equations for open systems (Eq.(2.1)).

As such, the thermal heating rate is

$$\Gamma^{\text{th}} = \bar{n}_{\text{th}}\gamma,$$

with $\bar{n}_{th}$ the Bose-Einstein occupancy at the oscillator frequency and γ the thermal damping. In the regime of interest (high vacuum, where the mean free path of the gas molecules is much larger than the diameter of the nanosphere), the expected collisional damping rate is proportional to the pressure P in the experimental chamber, and is given by [19, 5]

$$\gamma = \frac{8\sqrt{\pi}}{3}\frac{R^2}{m}\sqrt{\frac{m_{\text{gas}}}{2k_{\text{B}}T}}\left(2+\frac{\pi}{4}\right)P \tag{2.9}$$

where R is the radius of the nanosphere, m is its mass, and m_{gas} is the mass of the gas molecules.

So, the particle motion can be decoupled by the thermal environment in an experimental platform realized in high vacuum.

- **Dipole scattering**: the trapping beam drives the Brownian motion of the particle via its shot noise fluctuations. The calculation to evaluate the corresponding heating rate [58] can be derived in the semiclassical approximation starting from the momentum conservation for a scattering event between an incident photon and the particle. Taking into account the angular probability distribution for the dipole scattering pattern, it is possible to evaluate the amount of energy delivered to each mechanical degree of freedom. In particular, for a linearly polarized trapping beam, the heating rate for the three oscillation directions is:

$$\begin{pmatrix}\Gamma^x_{\text{dip}}\\ \Gamma^y_{\text{dip}}\\ \Gamma^z_{\text{dip}}\end{pmatrix} = \frac{\omega P_{\text{scatt}}}{10mc^2}\begin{pmatrix}2/\Omega_x\\ 1/\Omega_y\\ 7/\Omega_z\end{pmatrix}, \tag{2.10}$$

where P_{scatt} is the scattered power, the light is polarized along the y axis and propagates along the z axis.

- **Vacuum shot noise**: the Langevin equation that governs the evolution of the optical cavity oscillator is exactly like Eq.(2.2), but with the substitutions $\hat{b} \to \hat{a}$, $\Omega \to -\Delta$ and $\gamma \to \kappa$. As such, the optical oscillator undergoes a Brownian motion, driven by the optical input term $\sqrt{\kappa}\hat{a}_{\text{IN}}$. However, since

the Bose - Einstein phononic occupation number at the optical frequencies is negligible, the optical cavity mode can be assimilated to a high quality factor harmonic oscillator that undergoes a Brownian motion at the zero point fluctuations.

Because of the optomechanical interaction, the noisy vacuum field that resonates into the cavity exerts a random force on the mechanical oscillator via radiation pressure.

It can be shown, solving the system of equations (2.6) and (2.7), that effective input term acting on the mechanical oscillator is:

$$g\sqrt{\kappa}\chi_{\mathrm{c}}\left(\omega\right)\tilde{a}_{\mathrm{IN}}\left(\omega\right),$$

where $\chi_{\mathrm{c}} = 1/\left[\kappa/2 - i\left(\omega + \Delta\right)\right]$ is the optical susceptibility. So, the heating depends on the optomechanical configuration (the detuning of the laser beam, the coupling strength and the linewidth of the cavity). In the resolved sideband regime ($\Omega \gg \kappa$), for the optimal detuning $\Delta = -\Omega$ the corresponding heating rate is:

$$\Gamma^{\mathrm{vac}} \simeq \frac{\kappa g^2}{4\Omega^2}.$$

It is worth noting that this noise term is expected only in a quantum theory of the electromagnetic field.

2.3.3 Cooling the mechanical motion

In the experimental configuration, the laser light is always set on the red side of the cavity resonance. As stated above, this configuration leads to the *beam splitter* interaction, where the mechanical motion loses energy via the cold optical channel. Because of its importance for the understanding of experimental results, here is reported an overview of this optomechanical interaction.

The analysis starts from the solution of the system of Langevin equations (2.4) and (2.5), which leads to a modified mechanical susceptibility with $\Omega \to \Omega + \delta\Omega$

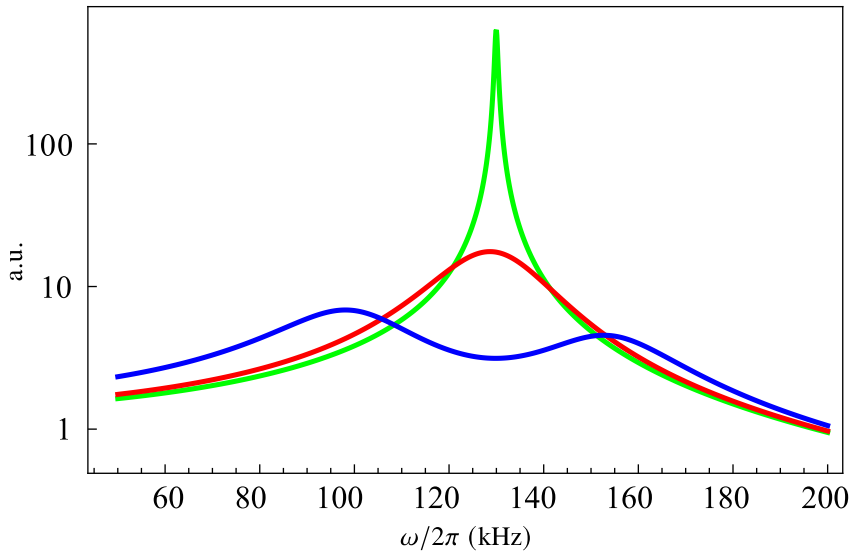

Figure 2: Squared modulus of the mechanical susceptibility in the positive frequency range for negligible mechanical damping, from the weak to the strong coupling regime. For $g/\kappa \sim 0.05$ (green curve) it has a Lorentzian shape. As the coupling strength is increased, at $g = \kappa/4$ (red curve), the Lorentzian shape is broader, with a FWHM of κ. For $g = \kappa/2$ (blue curve) the system is in the strong coupling regime. The two peaks, broad κ each, are $\sim 2g$ far apart. The three curves are evaluated for common experimental parameters $\Omega/2\pi = 130$ kHz, $\Delta = -\Omega$, $\kappa/2\pi = 57$ kHz.

and $\gamma \to \gamma + \Gamma_{\rm opt}$:

$$\begin{aligned}\delta\Omega(\omega) &= g^2\left[\frac{\Delta+\omega}{(\Delta+\omega)^2+(\kappa/2)^2}+\frac{\Delta-\omega}{(\Delta-\omega)^2+(\kappa/2)^2}\right],\\ \Gamma_{\rm opt}(\omega) &= g^2\left[\frac{\kappa}{(\Delta+\omega)^2+(\kappa/2)^2}-\frac{\kappa}{(\Delta-\omega)^2+(\kappa/2)^2}\right].\end{aligned} \tag{2.11}$$

Care must be taken in the interpretation of the modified susceptibility. Since the factors in 2.11 are frequency dependent, their intuitive interpretation as frequency shift and optical damping is valid only within certain approximations. For example, if the coupling strength goes to infinity, $\Gamma_{\rm opt}$ grows to infinity too. An a priori interpretation of $\Gamma_{\rm opt}$ as optical damping is clearly unphysical, since the upper limit to the mechanical losses is set by the optical losses (κ).

In Fig.(2) is reported the modulus squared of the modified mechanical susceptibility for different coupling strength values. Long story short, as long as $g \ll \kappa$ the

optomechanical interaction is weak and the modified susceptibility resembles the usual susceptibility of an oscillator with two Lorentzian peaks around $\pm(\Omega + \delta\Omega)$ and FWHM equal to $\gamma + \Gamma_{\rm opt}$. As $g = \kappa/4$, $\Gamma_{\rm opt} = \kappa$ and the system enters the so called *strong coupling regime*. From there, increasing the coupling strength value, the modified susceptibility is composed of two couples of peaks, at frequencies $\pm(\Omega \pm g)$ and broad $\kappa/2$ (assuming the mechanical damping negligible).

After this brief introduction, we specialize now on the cooling performances in the two regimes:

- **Optomechanical cooling in the weak coupling regime**: for $g \ll \kappa$, the equations (2.11) can be approximated to:

$$\begin{aligned}\delta\Omega &= g^2\left[\frac{\Delta+\Omega}{(\Delta+\Omega)^2+(\kappa/2)^2}+\frac{\Delta-\Omega}{(\Delta-\Omega)^2+(\kappa/2)^2}\right],\\ \Gamma_{\rm opt} &= g^2\left[\frac{\kappa}{(\Delta+\Omega)^2+(\kappa/2)^2}-\frac{\kappa}{(\Delta-\Omega)^2+(\kappa/2)^2}\right].\end{aligned} \tag{2.12}$$

  In the resolved-sideband regime the optimal cooling configuration is for $\Delta \simeq -\Omega$, where $\Gamma_{\rm opt} = 4g^2/\kappa$. The equation of motion for the mechanics expressed in the Fourier domain reads:

$$\tilde{b}\,(\omega) = \chi_{\rm m}^{\rm eff}\tilde{b}_{\rm IN},$$

  where $\tilde{b}_{\rm IN}$ is the combination of the thermal, optical and dipole scattering contribution and $\chi_m^{\rm eff}$ the mechanical effective susceptibility. Evaluating the corresponding PSD and integrating on the frequency axis, gives a mean phononic occupation number

$$\bar{n}^{\rm wc} = \frac{\Gamma_{\rm opt}\bar{n}_{\rm opt} + \gamma\bar{n}_{\rm th} + \Gamma_{\rm dip}}{\Gamma_{\rm opt}+\gamma},$$

  where $\bar{n}_{\rm opt} = (\kappa/4\Omega)^2$.

  Ideally, the particle thermal coupling in high vacuum is negligible and the minimum occupation number achievable is:

$$\bar{n}^{\rm wc} = \bar{n}_{\rm opt} + \Gamma_{\rm dip}/\Gamma_{\rm opt},$$

  which for the experimental parameters would be $\bar{n}^{\rm wc} = 0.014{+}0.05\left(\frac{2\pi\,30{\rm kHz}}{g}\right)^2$.

- **Optomechanical cooling in the strong coupling regime** : the core of the experimental work is about the observation of the mechanical motion with the optomechanical system in the strong coupling regime. When the coupling rate g exceeds the damping (namely, $4g \geq \gamma, \kappa$), the optical and mechanical modes can no longer be treated as separate entities and form hybrid optomechanical states [24, 65, 53, 70, 64, 76, 49, 38] and only the exact solutions of the optomechanical equations provide a proper description of the system.

  An introduction that catches the main concepts in reported in [3]. Basically, close to the optimal red detuning ($\Delta \simeq -\Omega$) the system can be easily described within the rotating wave approximation (RWA). As such, the equations of motion simplify and the optomechanical system can be described by a 2 X 2 - rather than 4 X 4 - matrix:

$$\begin{pmatrix} \dot{\hat{a}} \\ \dot{\hat{b}} \end{pmatrix} = \begin{pmatrix} i\Delta - \kappa/2 & -g \\ -g & -i\Omega - \gamma/2 \end{pmatrix} \begin{pmatrix} \hat{a} \\ \hat{b} \end{pmatrix}$$

  The square matrix (usually defined as drift matrix) encodes the dynamical properties of the system: its eigenvectors correspond to the normal modes and the real (imaginary) part of the eigenvalues represent the corresponding damping (frequency)

$$\lambda^{\pm} = \Omega - i\kappa/2 \pm \sqrt{g^2 - (\kappa/4)^2},$$

  where the mechanical damping contribution is supposed negligible for the sake of simplicity.

  Now, as long as $g < \kappa/4$ the square root is imaginary and the two eigenvectors are degenerate but with different damping terms. It will be shown that the two eigenvectors are either optical or mechanical. On the other hand, as $g > \kappa/4$, the square root displaces the two eigenfrequencies and the optical and mechanical components mix in the eigenvectors. The system enters the strong coupling regime and hybrid optomechanical excitations raise.

  It is worth noting that, unlike in the weak coupling regime, here a mechanical oscillator cannot be defined: the mechanical spectrum shows two broad peaks which correspond to the projection along the motional axis of the two normal modes of the optomechanical space.

Wishing to compare the mechanical cooling performance in the strong coupling regime with the results of the weak coupling, it should be clearly stated how the mechanical excitation in quantified: a definition of a mean phononic occupancy requires a definition of a frequency which, here, is not available. This point, that shouldn't be overlooked for a proper analysis and interpretation of the system, leads to small discrepancies with the results reported in literature [38], where the mechanical excitation is quantified in terms of the phononic occupation. A precise analysis of the mechanical excitation definition is given later and here we report the standard results for the minimum occupation in the strong coupling regime (for negligible thermal coupling):

$$\bar{n}_{\min} = \bar{n}^{\mathrm{wc}} + \Gamma_{\mathrm{dip}}/\kappa + 2\bar{n}^{\mathrm{wc}} \left(2g/\kappa\right)^2 .$$

In the weak coupling regime the minimum occupation number decreases as the coupling strength increases. Here, on the contrary, the cooling is less efficient. In fact, the optical damping saturates to the value set by the optical losses, and a further increase of the coupling leads to a higher cavity mediated back action.

These are the main concepts regarding the optomechanical cooling performances. However, little insight is gained about the dynamical description of the system, which is encoded in the eigenvalue/eigenvector structure of the complete Drift matrix of the system, that is analysed in Fig.(3).

In the upper panel is reported the trend of the eigenfrequencies of the system for typical parameters ($\Omega/2\pi =$ 130 kHz, $\kappa/2\pi =$ 57 kHz and negligible mechanical damping) as the laser frequency is swept on the red side of the cavity resonance. In the weak coupling regime, $g/\kappa \simeq 0.05$, the two branches (green curves) cross at $\Delta = -\Omega$ and are almost two straight lines with the bare optical and mechanical frequency values. Increasing the coupling strength to $g = \kappa/4$, the two branches (in red) show the optomechanical shift for $\Delta \simeq -\Omega$. In the strong coupling regime, for $g = \kappa/2$, the system shows an avoided crossing (blue branches) reminiscent of what is expected for the coupled system illustrated by the Jaynes-Cummings Hamiltonian [30].

The lower panel shows the mechanical (dashed line) and optical (solid line) energy contribution to the eigenvectors for the frequency branches plotted with dark hue in the upper panel.

In the weak coupling regime, the selected branch is mainly mechanical and a little increase of the optical component is visible close to $\Delta \simeq -\Omega$.

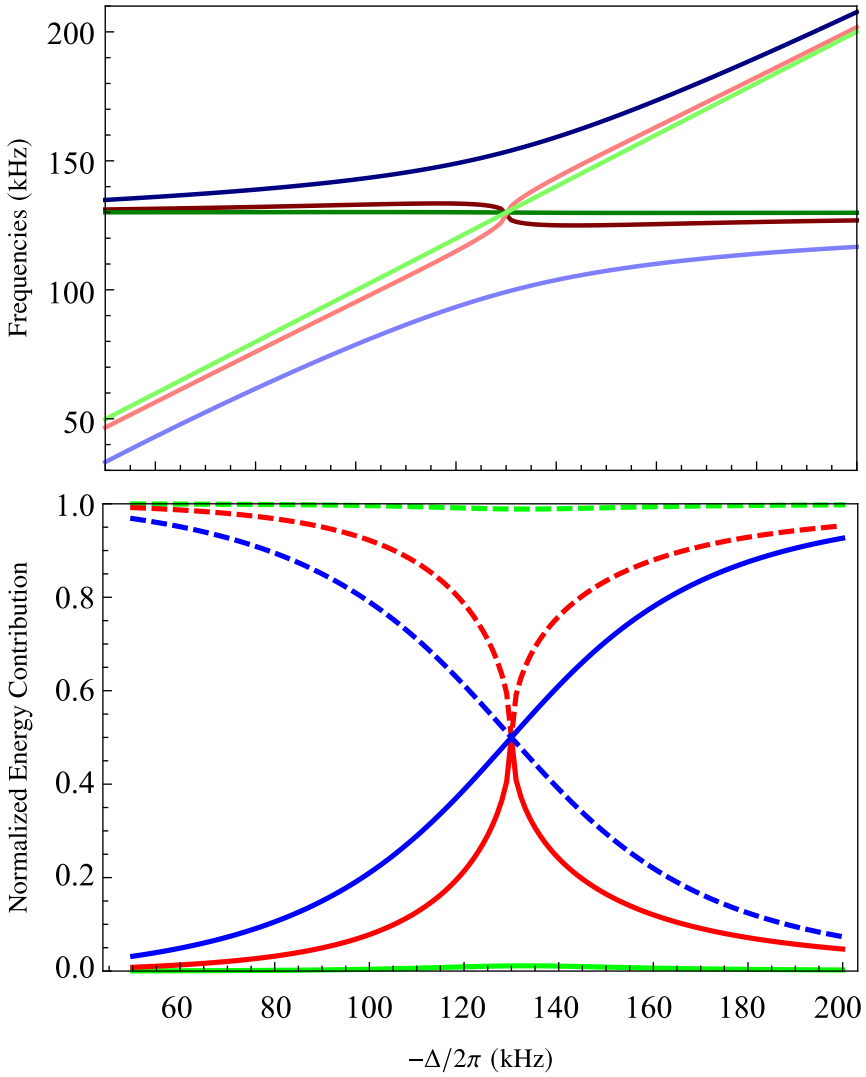

Figure 3: Upper panel: eigenfrequencies of the optomechanical system composed of a mechanical oscillator (with a frequency of 130 kHz) coupled to an optical oscillator (with optical losses $\kappa = 2\pi$ 57 kHz) as a function of the detuning. The green branches are evaluated for $g \simeq 0.05\kappa$, in the weak coupling regime. The red curves at the threshold value of $g = \kappa/4$ and the blue in the strong coupling regime, for $g = \kappa/2$. Lower panel: distribution of energy between the optical (solid line) and mechanical (dashed line) component in the eigenmodes.

At the threshold value between the strong and the weak coupling regime ($g = \kappa/4$), the eigenvector is mainly mechanical when the optical oscillator is far from the mechanical resonance. As the detuning gets close to $-\Omega$, the optical and mechanical components equally contribute to the eigenmode.

In the end, in the strong coupling regime, the avoided crossing leads to the swap in the components of the eigenvectors: when the optical field is far red detuned the mode is mainly mechanical. When the detuning is close to the mechanical frequency the energy, again, is equally split between the optical and the mechanical component and the excitations are hybrid optomechanical states [24, 65, 53, 70, 64, 76, 49, 38]. When the laser light gets closer to the optical resonance, the eigenmode turns optical.

The behaviour of the eigenvectors for the light coloured branches, which is not reported in the plots, is specular.

2.3.4 Cavity optomechanics with a 2D mechanical oscillator

In our experiment the particle is placed along the cavity axis on the node of the standing wave, exploiting the coherent scattering configuration. Only the dynamics that occurs on the plane orthogonal to the tweezer axis is optomechanically coupled.

The motion can be decomposed into two independent mechanical modes oscillating along perpendicular directions defined by the linear polarization of the tweezer field.

For the particle close to the cavity node and an angle θ between the tweezer polarization and the cavity optical axis, the optomechanical couplings for the x and y motion reads:

$$g_x = E_\mathrm{d} k \sin^2\theta x_\mathrm{zpf},$$
$$g_y = E_\mathrm{d} k \sin\theta\cos\theta y_\mathrm{zpf}.$$

The Hamiltonian of the isolated system is:

$$H/\hbar = -\Delta\hat{a}^\dagger\hat{a} + \Omega_x\hat{b}_x^\dagger\hat{b}_x + \Omega_y\hat{b}_y^\dagger\hat{b}_y + \left(\hat{a}^\dagger + \hat{a}\right)\left[g_x\left(\hat{b}_x^\dagger + \hat{b}_x\right) + g_y\left(\hat{b}_y^\dagger + \hat{b}_y\right)\right].$$

The complete solutions that derive from this Hamiltonian, adding the dissipative terms in the Langevin equations, fully describe the system. However, following this path would give little insights at this stage.

Wishing to have a qualitative picture of the physics, it results useful the study

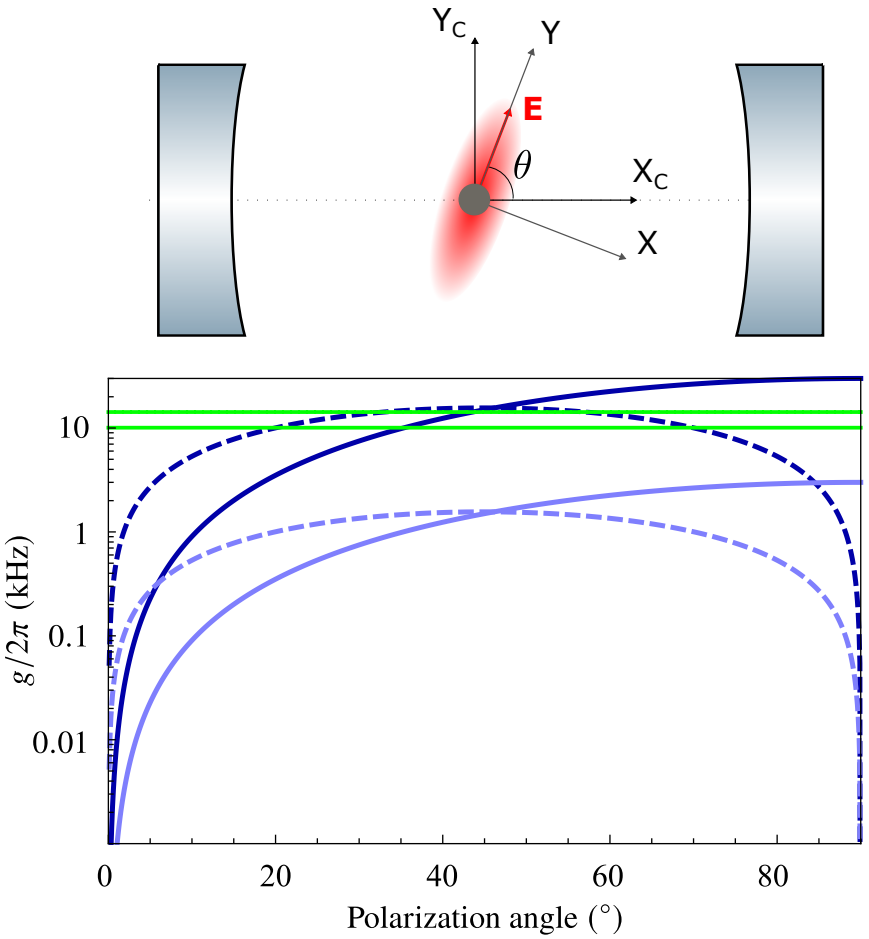

Figure 4: Scheme of the experimental system. A silica nanosphere levitates on the optical potential created by the light of an optical tweezer, propagating along the Z axis, with the electric field along the Y axis. The nanosphere is positioned on the axis of an optical cavity (which defines the direction X_C), in correspondence of a node of the field of a cavity mode. Graphic: coupling strength as a function of the polarization angle for the x (solid line) and y (dashed line) for strong (dark hue) and weak (light hue) coupling. The upper horizontal line marks the $\kappa/4$ threshold for the 1D strong coupling regime. The lower horizontal line is the threshold to enter the 2D strong coupling regime when $g_x \sim g_y$.

of the system in the frame defined by the cavity axis, i.e.:

$$\begin{pmatrix} x_\mathrm{c} \\ y_\mathrm{c} \end{pmatrix} = \begin{pmatrix} \sin\theta & \cos\theta \\ -\cos\theta & \sin\theta \end{pmatrix} \begin{pmatrix} x \\ y \end{pmatrix}.$$

The particle motion is decomposed in its x_c (y_c) component along (orthogonal to) the cavity axis, that is conventionally called the geometrical bright mode, GBM (dark mode, GDM). The Hamiltonian expressed in terms of the GBM and GDM modes is :

$$H/\hbar = -\Delta\hat{a}^\dagger\hat{a} + \Omega_\mathrm{b}\hat{b}_\mathrm{b}^\dagger\hat{b}_\mathrm{b} + \Omega_\mathrm{d}\hat{b}_\mathrm{d}^\dagger\hat{b}_\mathrm{d} + g_\mathrm{b}\left(\hat{a}^\dagger + \hat{a}\right)\left(\hat{b}_\mathrm{b}^\dagger + \hat{b}_\mathrm{b}\right) + g_\mathrm{bd}\left(\hat{b}_\mathrm{b}^\dagger + \hat{b}_\mathrm{b}\right)\left(\hat{b}_\mathrm{d}^\dagger + \hat{b}_\mathrm{d}\right),$$

with the frequencies defined as [69]:

$$\Omega_\mathrm{b}^2 = \Omega_x^2\sin^2\theta + \Omega_y^2\cos^2\theta, \tag{2.13}$$
$$\Omega_\mathrm{d}^2 = \Omega_x^2\cos^2\theta + \Omega_y^2\sin^2\theta, \tag{2.14}$$

and the coupling strength values:

$$g_\mathrm{b} = g_x\sqrt{\frac{\Omega_x}{\Omega_\mathrm{b}}}\sin\theta + g_y\sqrt{\frac{\Omega_y}{\Omega_\mathrm{b}}}\cos\theta. \tag{2.15}$$
$$g_\mathrm{bd} = \frac{\sin\theta\cos\theta\left(\Omega_y^2 - \Omega_x^2\right)}{2\sqrt{\Omega_\mathrm{b}\Omega_\mathrm{d}}}. \tag{2.16}$$

The GBM mode couples directly to the cavity field, while the GDM is only coupled to the GBM. It is noteworthy that if the two bare mechanical frequencies are degenerate, the GDM is totally decoupled from the system and the GDM/GBM structure describes the mechanical components of the system eigenvectors. On the other hand, if the mechanical frequencies are different, the GDM and GBM mix in the eigenvectors of the system. Conventionally, the eigenvectors with the mechanical component of the motion primarily along the cavity axis is called bright mode (BM), and the other is defined as the dark mode (DM).

It should be emphasized that while the GBM directly cools down via a red detuned laser field, the GDM sympathetically cools down through its interaction with the cold GBM (that in turn heats up).

With these two descriptions - the tweezer and the cavity system - it is useful to point out as a rule of thumb where they're preferentially used:

- **Two non-degenerate oscillators in the very weak optomechanical**

coupling $\vee$ in the strong coupling but with the tweezer radiation far from resonance: the motion in the transverse plane is better described in the framework defined by the tweezer. However, that's not true when the cavity mediated fluctuations couple the two oscillator. Owing to the optical spring effect, two non degenerate oscillators might be shifted towards degeneracy and become correlated even for weak optomechanical coupling [68, 69]. In this case, the system can be conveniently represented in terms of the GBM/GDM structure in the cavity reference. [20, 39, 59].

- **Detuning close to the mechanical frequencies $\wedge$ strong coupling** : now, the optomechanical coupling is more important than the frequency difference between the modes in determining the system's dynamical behaviour, and it is more appropriate to use the cavity axes as framework for describing the 2D motion.

To get a better understanding of the dynamics of the system, the eigenvalues/eigenvectors structure here is analysed as a function of the tilt angle θ. In Fig.(5), panels b),c) and d), is reported the amount of energy for the optical component (solid line) and the mechanical component along/orthogonal to (dashed/dot-dashed line) the cavity axis for the three eigenvectors of the system as a function of the angle between tweezer linear polarization and the cavity axis. Panel a) reports on the corresponding eigenfrequencies of the system. The simulation is evaluated for typical experimental parameters: the two mechanical frequencies of 120 kHz and 130 kHz and the optical mode of 125 kHz, with a decay rate of 57 kHz. The dark coloured curves represent the system for a maximal coupling strength $\sqrt{g_x^2 + g_y^2} \sim 2\pi$ 30kHz, while the light coloured curves are evaluated for $\sqrt{g_x^2 + g_y^2} \sim 2\pi$ 3 kHz. The dependence of the coupling strength on the polarization axes is plotted in Fig.(4).

In the low coupling case the system is always in the weak coupling regime and the interpretation of the dynamics is quite simple. In fact, the frequencies of the system show little dependence on the angle and the eigenvectors are either optical or mechanical. As stated before, the preferred framework to describe the plots here would be that defined on the tweezer polarization. As such, since the plots here are referred to the cavity framework, the mechanical eigenvectors simply swap - as the angle goes from 0° to 90° - according to the projection of the tweezer defined modes along the cavity-defined axes (panels c) and b)).

On the other hand, in the high coupling configuration, the system passes across three different regimes.

For a tilt angle between 0° and $\sim$ 35° the optomechanical system is in the weak coupling: the eigenfrequencies in the upper panel are nearly constant at the beginning and start shifting appreciably from $\theta \sim 25°$. In this region the description fits with the one of the low coupling configuration (and the curves overlap indeed).

Between $\sim$ 35° and $\sim$ 70° the system enters the 2 dimensional strong coupling: the eigenfrequency curves as a function of the detuning would show a double avoided crossing. It is worth noting that threshold for the two dimensional strong coupling is less stringent than the $\kappa/4$ value for the 1D mechanical system, as will be shown in the next section. Here we see the formation of the bright modes (dark blue and dark green curves, panel a)) and dark mode (dark red curve, panel a)) structure. The hybrid modes are roughly half optical and half mechanical, with the mechanical excitation along the cavity axis that is mainly coupled to the cavity field (i.e. mainly contributes to the bright modes eigenvectors, as shown in panels b) and d)). On the contrary, the dark eigenmode is mainly composed of the motion orthogonal to the cavity axis, with a small optical component. Here it's clear why the cavity-based coordinate system is preferred to describe the system dynamics, since the mechanical component of the bright modes (dark mode) is roughly the GBM (GDM).

In the end, for an angle close to 90°, only the x motion is in the strong coupling regime. The eigenvector previously associated to the dark mode is composed of the mechanical excitation along the tweezer polarization axis that is weakly coupled to the cavity field. The mechanical component of the bright mode here is mainly the x motion.

2.3.5 From hybrid optomechanical states to polaritonic modes

Starting from the basics of cavity optomechanics, it has been introduced the physics of the strong coupling regime for a three partite system composed of two mechanical oscillators and one optical.

However, few words have been spent about the potential application of this experimental platform as a tool for quantum experiments.

The strong coupling between photons and bosonic excitations in matter produces hybrid quasi-particle states known as polaritons [67, 27, 26]. It has been observed in quantum electrodynamics experiments based on atoms [66, 14], ions [45], excitons [74, 52, 77], spin ensembles [28, 61] and superconducting qubits [72].

While these systems are intrinsically quantum and the strong coupling allows

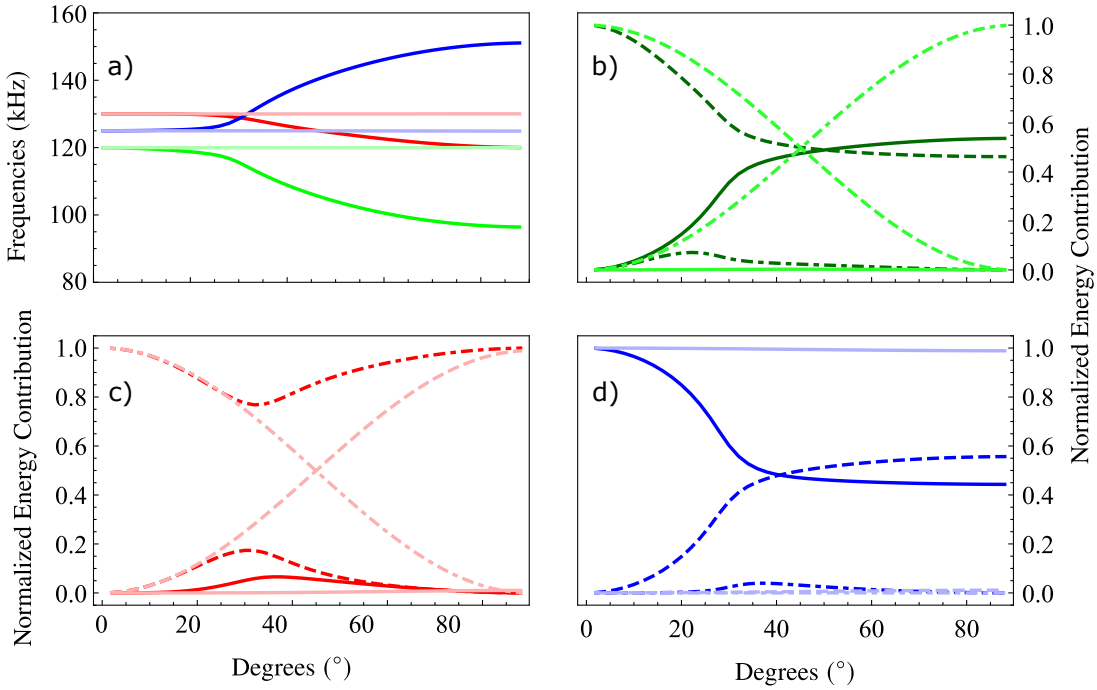

Figure 5: Panel a): eigenfrequencies of the system composed of two mechanical oscillators (with frequencies 130 kHz and 120 kHz) coupled to an optical oscillator (of frequency 125 kHz) for a maximal coupling strength of 30 kHz(dark coloured lines) and 3 kHz (light coloured lines) as a function of the angle between the polarization axis of the optical tweezer and the cavity axis. Panels b),c) and d): distribution of energy between the three oscillators within each normal mode, related respectively to the green, red and blue curve of panel a). The solid line is for the optical excitation, while the dashed (dot dashed) line is for the mechanical motion along (orthogonal to) the cavity axis.

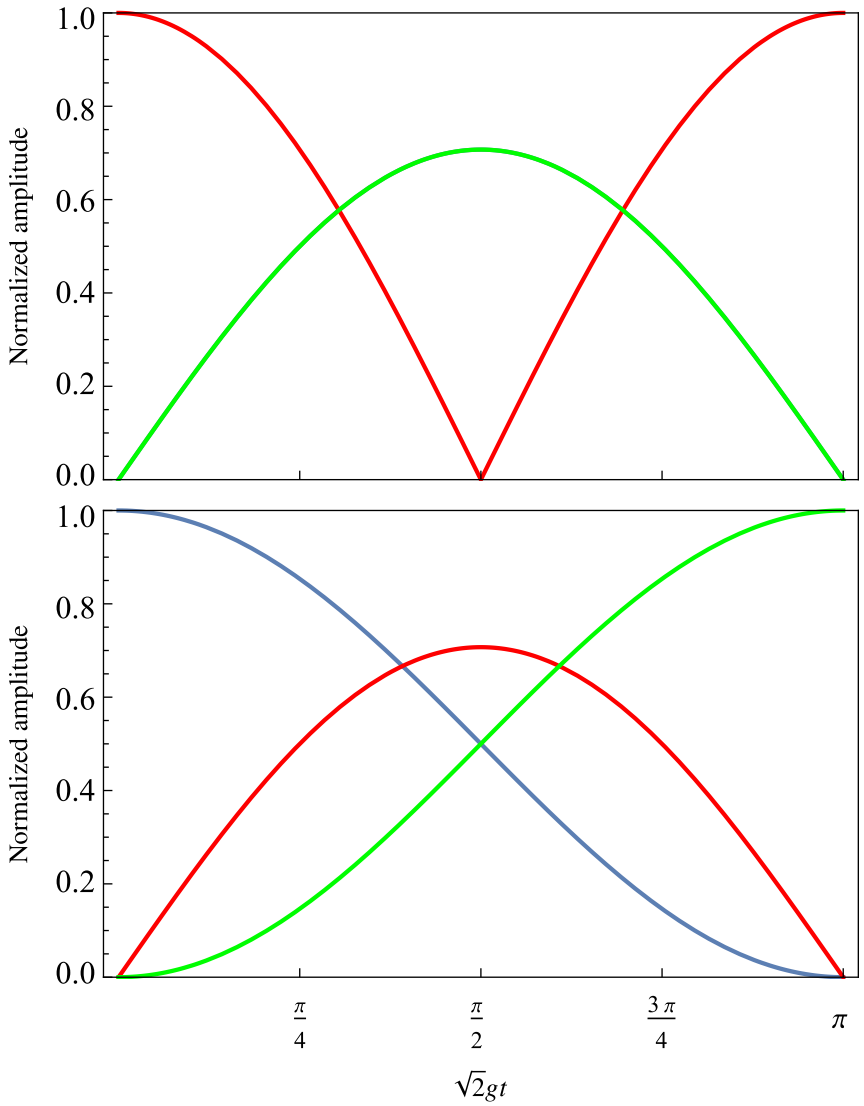

Figure 6: Free evolution of the optomechanical excitations for the three partite optomechanical system. At time $t = 0$ the amplitude of the three oscillators ($\hat{a}$ for the optical, $\hat{b}$ and $\hat{c}$ for the two mechanical) is set equal to 1. Upper panel: evolution of the optical amplitude ($\hat{a}$) in the rotating frame. As the system evolves, the optical excitation (red line) is replaced by the two mechanical excitations (green and blue lines, that overlap) at time $\bar{t} = \pi/2\sqrt{2}g$. After a time $t = 2\bar{t}$ the optical oscillator goes back to the initial state. Lower panel: evolution of the mechanical amplitude ($\hat{b}$) in the rotating frame. Here, at time $\bar{t}$, the optical excitation component reaches its maximum. At time $t = 2\bar{t}$ the two mechanical excitations swap their state. The evolution of the mechanical amplitude $\hat{c}$, which is not reported here, is specular to the evolution of $\hat{b}$.

for quantum state transfer between the system components, in our platform the evidence of hybrid optomechanical state doesn't necessarily imply quantumness, i.e. the avoided crossing raises even in the classical regime.

In a nutshell, the hybrid states can be called *polaritonic modes* only if the Rabi oscillation can set up.

That said, here a pedagogic introduction to the 2-D vectorial polariton is given by solving the dynamics for the isolated system of the coupled oscillators, similarly to the approach in [8]. In the simplest case of equal optical and mechanical frequencies and the optomechanical interaction equally split between the oscillators, the equation of motion is (in the RWA):

$$\dot{x} = -i \begin{pmatrix} \Omega & -g & 0 \\ -g & \Omega & -g \\ 0 & -g & \Omega \end{pmatrix} x,$$

where $x^T = \left(\hat{b}, \hat{a}, \hat{c}\right)$, with $\hat{b}$ and $\hat{c}$ for the mechanical modes, and $\hat{a}$ for the optical. The eigenvalues and eigenvectors of the matrix are

$$\lambda = \begin{pmatrix} \Omega \\ \Omega - \sqrt{2}g \\ \Omega + \sqrt{2}g \end{pmatrix}, \qquad x' = \left[\tfrac{1}{\sqrt{2}} \begin{pmatrix} -1 \\ 0 \\ 1 \end{pmatrix}, \tfrac{1}{2} \begin{pmatrix} 1 \\ \sqrt{2} \\ 1 \end{pmatrix}, \tfrac{1}{2} \begin{pmatrix} 1 \\ -\sqrt{2} \\ 1 \end{pmatrix} \right],$$

The first eigenstate is composed only by mechanical excitations and represents the dark mode, which is decoupled from the optical mode. The other two modes represent mixed states, the bright modes, in which optical and mechanical degrees of freedom hybridize. In this particular configuration we see that the energy is equally distributed between the optical and the mechanical excitations in each bright mode, and the overall mechanical excitation is equally split between the two mechanical oscillators.

Rotating back to the original basis we find:

$$x^{\mathrm{R}}(t) = \begin{bmatrix} \cos\left(gt/\sqrt{2}\right)^2 & \frac{i}{\sqrt{2}} \sin\left(\sqrt{2}gt\right) & -\sin\left(gt/\sqrt{2}\right)^2 \\ \frac{i}{\sqrt{2}} \sin\left(\sqrt{2}gt\right) & \cos\left(\sqrt{2}gt\right) & \frac{i}{\sqrt{2}} \sin\left(\sqrt{2}gt\right) \\ -\sin\left(gt/\sqrt{2}\right)^2 & \frac{i}{\sqrt{2}} \sin\left(\sqrt{2}gt\right) & \cos\left(gt/\sqrt{2}\right)^2 \end{bmatrix} x(0) \tag{2.17}$$

where x^{R} is the vector expressed in the frame rotating a the angular frequency Ω. The solutions are plotted in Fig.(6). We clearly see that the three oscillators exchange their excitations at a rate set by $\sqrt{2}g$. Namely, as $\sqrt{2}g\bar{t} = \pi/2$, the

optical excitation is replaced by the mechanical excitation, while for the mechanical oscillator the optical excitation reaches the maximum.

Now follows a brief review of the optomechanical figure of merits, useful to introduce the vectorial polaritons:

- the mechanical oscillators ($\hat{b}$,$\hat{c}$) exchange energy with the optical oscillator ($\hat{a}$) at a rate proportional to the coupling strength g;
- the energy decays from the mechanical system into the thermal bath at a rate γ;
- the excitations driven by the random external force (combination of the noise terms of Sec.2.3.2) enter the mechanical system at a rate proportional to Γ_{dec} (precisely half an excitation, $\hbar\Omega/2$ enters the system at a rate $2\Gamma_{\mathrm{dec}}$ and gives a random kick to mechanical oscillator);
- for the optical mode, the energy decay rate (κ) equals the decoherence rate, since the phononic occupation number at the optical frequency is null. In the time domain, $1/\kappa$ is the average time that a photon spends into the cavity before leaving it.

Each mechanical oscillator is coupled to a thermal bath at temperature T. Now, the dynamics predicted by the equation (2.17) is valid as long as the dissipation and decoherence mechanisms are not relevant.

If the oscillators swap their states within the optical decay time (only optical, in a ultra high vacuum where the mechanical coupling vanishes), i.e. $\bar{t}\kappa < 2\pi$ - which means $g > \kappa/4\sqrt{2}$ - the system enters the so called strong coupling regime.

A more stringent condition is the Quantum coherent regime, in which the decoherence mechanisms are slow with respect to the swapping time $4\sqrt{2}g > 2\Gamma_{\mathrm{dec}}, \kappa$.

It is worth noting that the rate at which the energy flows between the oscillators of the optomechanical system strongly depends upon the configuration. For a system composed of two degenerate coupled oscillators the energy flows at a rate of g (rather than $\sqrt{2}g$) between the oscillators. In this way, the condition for reaching the strong coupling regime is less stringent for a three partite system.

The rate of energy flow depends, moreover, on the frequencies of the oscillators involved. In practice, if two interacting oscillators have different bare frequencies, the slowest terms in the interaction energy rotate at the frequency difference

$\delta\Omega$. These terms average to zero on a time greater than $\delta\Omega^{-1}$. In practice, the interaction term vanishes for $\delta\Omega \gg \kappa, \gamma$.

To conclude, we point out that in most quantum electrodynamics and optomechanical systems polaritons are considered as scalar bosons. We remark indeed that here the two mechanical modes represent the orthogonal components of the particle motion. Their linear superposition has therefore a clear physical meaning, representing a position vector that can be associated to a physical vibration direction on a plane [68] thus conferring a peculiar vectorial nature to the polariton field.

3 Preparing the optomechanical experiment

To implement cavity optomechanics experiments, it is necessary to place the levitating particle into the region defined by a field mode of a high finesse optical cavity with sub-micrometric precision. The position must be stably and accurately maintained, avoiding excess mechanical and acoustic vibrations. A prerequisite is loading the dipole trap (optical tweezer) without spoiling the cavity mirrors, something that easily occurs due to particle deposition on the surface of mirrors. Finally, high vacuum conditions must be achieved in reasonable time, maintaining stable conditions. Even this latter procedure is conditioned by the relatively high pressure necessary for the initial trapping stage and often by the presence of solvents used for injecting the particles in the chamber through a nebulizer. A clean and reproducible method to prepare a levitating nanoparticle for cavity optomechanical experiments is not straightforward.

3.1 Overview

A possibility is to load the particle on the optical tweezer in a first chamber and then transfer it to a cleaner environment containing the optical cavity and the positioner. A movable optical trap is described in [40]. The trap is loaded in the first chamber using a nebulizer, then the whole tweezer, mounted on micrometric positioners in an extensible arm, is moved to the second chamber, and the particle is delivered to the stationary wave of an optical cavity. To stabilize the particle during the transfer, a cooling scheme acting on the tweezer optical power is used. A different method to transfer a levitating particle between different vacuum chambers is described in [23]. A standing wave is created inside a hollow fiber connecting the two chambers by means of counter-propagating laser beams. The particle is trapped on an anti-node of the standing wave and then moved by slightly shifting the frequencies of the two beams. The collection of the particle in the second chamber has not yet been reported.

Here [11], similar to [40], the particle is trapped in the first chamber by a tweezer placed on a movable arm and then translated into the experimental chamber containing the optical cavity. It is then transferred to the second optical trap that is mounted inside the second chamber on nano-positioners [3]. This sec-

[3]Check out the video of the protocol: https://youtu.be/3yfppTbf2II

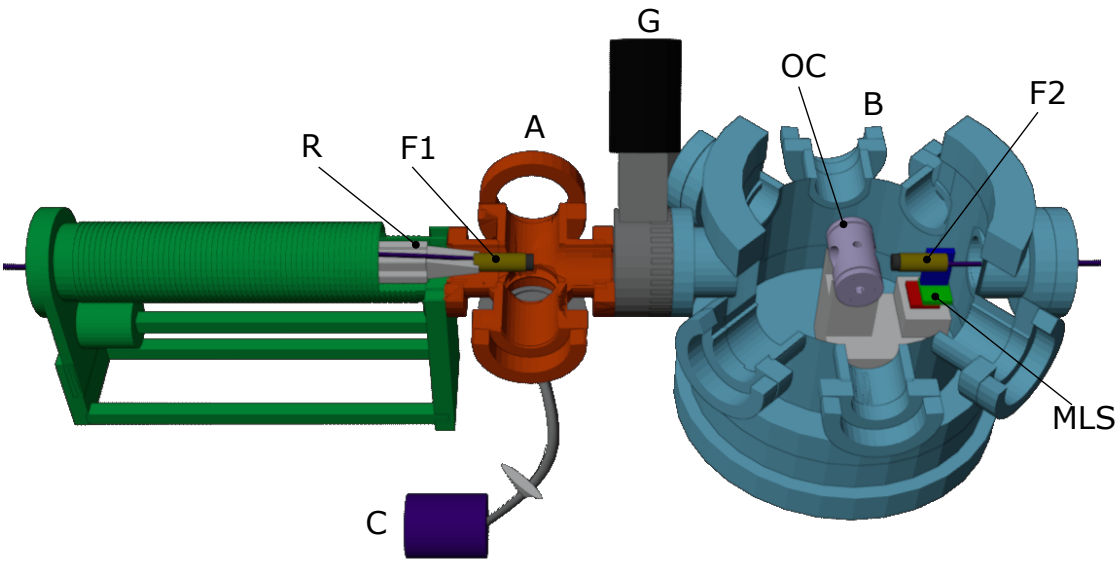

Figure 7: Experimental setup. Nanoparticles are injected in chamber C and then transported in a gas flux toward chamber A where they are captured by the tightly focused light of a laser diode delivered by a single-mode fiber. The fiber head with the focusing system (F1) is mounted on the tip of a rod (R) that can be manually translated between chambers A and B through the gate G. The second optical tweezer is formed by the light of a Nd:YAG laser and delivered by a similar optical system (F2) mounted on a three-axis miniature linear translation stage (MLS). The focus can be positioned inside the optical cavity (OC) with sub-micrometric precision.

ond tweezer is used to accurately position the particle inside the optical cavity. Mounting the nano-positioners on the chamber baseplate that also supports the optical cavity, instead of placing them on the moving arm, significantly improves the overall mechanical stability. Moreover, the moving arm is retracted after the particle transfer, and the vacuum chambers are isolated. As a consequence, the environment in the experiment chamber is suitable for a rapid evacuation down to very low pressure. Now follows a description of the transfer protocol.

3.2 Transfer of a levitated nanoparticle between optical tweezers

The setup is shown in Fig.(7). Nanoparticles are caught in chamber A and then transferred to the second trap in chamber B. The optical tweezer in the first

chamber is realized with a fibered 976 nm laser diode (LD). The light delivered by a single−mode fiber is collimated and focused using an optical system (F1) composed of two aspheric lenses, having a nominal focal length and a numerical aperture of 15.4 mm (N.A. 0.16) and 3.1 mm (N.A. 0.68), respectively. The two lenses are screwed on the fiber head connector. The beam at the focus is elliptical with waists of 0.96μm and 0.92μm, as deduced from the particle oscillation frequencies at the typical output power of 250 mW[46]. The fiber head with the optics is mounted at the end of a 500 mm long, X−shape aluminum rod screwed on the moving flange of a bellowed sealed linear shift mechanism (HV Design) that allows us to manually translate it between chambers A and B. We note that this support is sensitive to mechanical vibrations, making this trap unsuitable for stable cavity optomechanics experiments.

3.2.1 Trapping a particle

A drop of aqueous solution of silica nanospheres (9 % of particles, in mass) with mean diameter 125nm (measured by photon correlation imaging [18]) is injected inside chamber C that is filled with clean nitrogen, while chamber A is evacuated. The valve separating the two chambers is opened, and the dust of nanoparticles is introduced in chamber A, carried by the gas turbulence produced by the pressure unbalance. Trapping by the optical tweezer occurs when a pressure of ∼100 mbar is achieved in chamber A, typically within few minutes. With a particle trapped, before opening the gate G, residual wandering nanoparticles are pumped out from chamber A, whose pressure is gently decreased down to the mbar level. The chamber is then slowly refilled with pure nitrogen up to ∼30 mbar, and the gate is opened to equilibrate the pressure between chambers A and B (which was initially in high vacuum).

3.2.2 Moving the particle in the experimental chamber

The optical tweezer is translated to chamber B and positioned in front of the second optical trap. We remark that, at this pressure, the nanoparticle motion is over damped, and we can keep the levitating particle during the translation without using any active feedback. The second tweezer is formed by the 1064 nm radiation of a Nd:YAG laser and delivered into chamber B by a polarization maintaining fiber. The focusing optical system screwed on the fiber head (F2) is the same of the first tweezer and is positioned on a three-dimensional miniature linear stage (PI Q− 522). The beam waists at the focus are 1.02 μm and 0.93 μm, and the

typical optical power is 200 mW. Fibered beam − splitters allow us to collect part of the light arriving from the fiber heads. With the help of dichroic mirrors, we can thus measure the transmitted and back−scattered light of both sources.

3.2.3 Position optimization

To transfer the particle between the two tweezers, we have to superpose the positions of their intensity maxima with submicrometric precision. This procedure is performed by moving the second fiber head. Its transverse position with respect to the optical axis is optimized by maximizing the light transmission between the two fibers, while the distance between the two fiber heads must take into account the chromatic aberration, as sketched in Fig.(8b). We remark that the light of the second tweezer remains off during the whole procedure to avoid the accidental formation of an unstable potential by the superposition of the two intensity profiles.

To define the optimization procedure, we have performed a preliminary characterization of the optical coupling between the two fibers at the two used wavelengths. The transmitted power of the Nd:YAG light through the first fiber and that of the LD light through the second fiber are reported in Fig.(8a). The transverse position of the fiber head is kept optimized during the measurement, while the two fiber heads are moved closer at $\sim 1.1\mu m$ steps. The solid line, for each of the two wavelengths, is given by the overlap integral of the two counter-propagating modes, fitted to the experimental data. We find a distance of 9.8 μm between the positions of the foci for the two wavelengths. As shown in the scheme of Fig.(8b), assuming two identical focusing systems, the optimal distance to transfer the particle between the tweezers is halfway between the transmission maxima at the two wavelengths [this position is labeled as P2 in Fig.(8b)]. The operative procedure is then the following: we optimize the transmission of the LD light through the second fiber by moving the fiber head in the three directions, and afterward, we increase the distance of the fiber heads by $\sim 10\mu m$.

3.2.4 Particle transfer

To load the second trap, we boost the Nd:YAG power and slowly turn off the LD. With the described protocol, we can reliably transfer the particle between the two traps. In Fig.(9), we show a photo of the two optical systems and the levitating nanoparticle before and after the transfer. The power spectra of the light collected by the fibers in the back and forward directions, also shown in Fig.(9), exhibit the

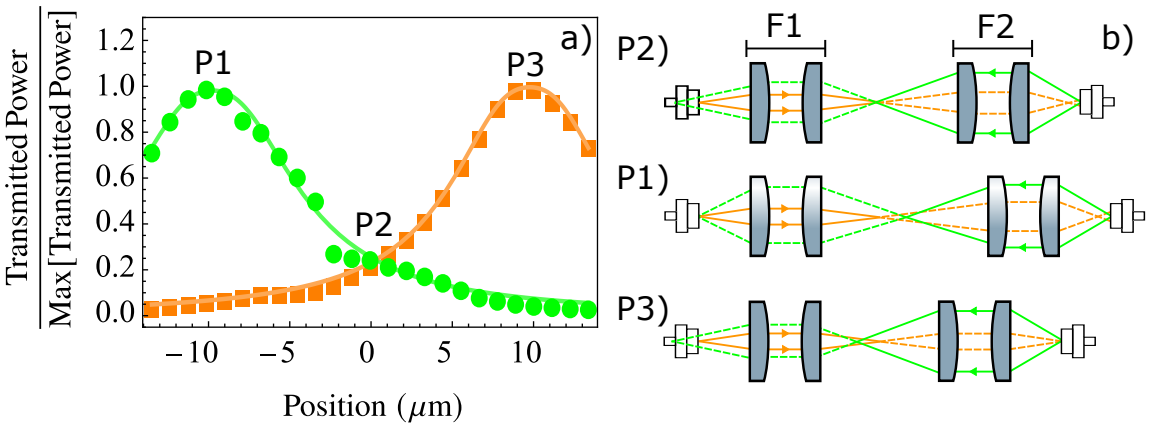

Figure 8: (a) Transmitted power of the laser light from the two sources through the two optical fibers and the corresponding F1 and F2 optical systems. Green dots: Nd:YAG light. Orange squares: LD light. Data are recorded approaching the two fiber heads at 1.1μm per step and normalized to the maximum transmitted power for each wavelength. Abscissa represents the variation of the distance of the fiber heads with the origin set halfway between the two maxima. Solid lines: overlap integral between the propagating field modes, fitted to the experimental data. (b) Schematic diagram of the two focusing systems during the measurement. Green (orange) rays represent the Nd:YAG (LD) beam propagation with arrows indicating the direction. P2 indicates the optimal position to transfer the particle as the two focuses are spatially overlapped. At relative position P1(P3), the two focusing systems are optimally placed to couple the Nd:YAG (LD) optical power. In that case, the distance between the two traps is 9.8 μm.

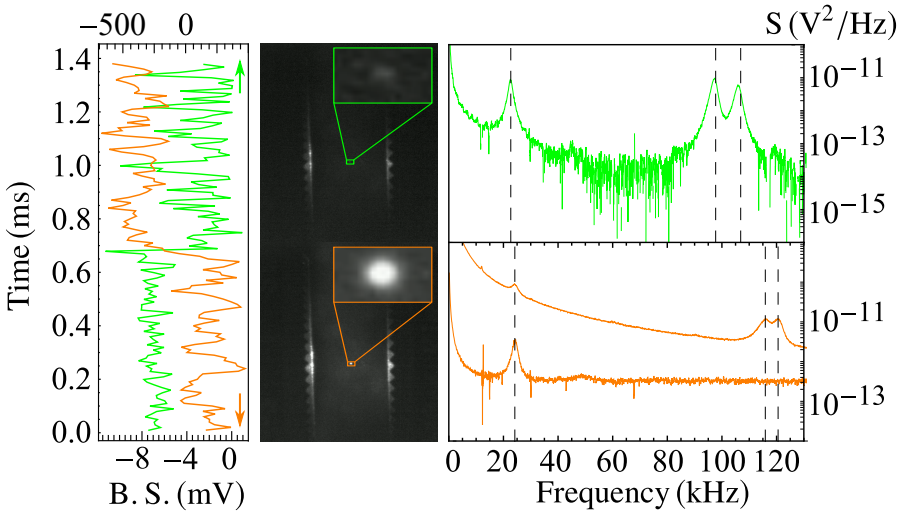

Figure 9: Left panel: The light back scattered (B.S.) from the particle is collected from the trapping fibers during the transfer between the LD and the Nd:YAG tweezers. Orange: LD light signal (scale on the bottom axis). Green: Nd:YAG light signal (scale on the top axis). Central panel: images of the Nanoparticle trapped by the LD (bottom picture) and the Nd:YAG (top picture) optical tweezers. Bright spots, also shown in the enlarged insets, are due to the particle dipole emission, and scattered light allows us to identify the edges of the focusing lenses. The brightness difference between the two traps is due to the different camera sensitivity at the two wavelengths. Right panel: spectra of the back and forward scattered light, collected by the fibers and acquired at a background pressure of 2 mbar, exhibiting spectral peaks corresponding to the three eigenfrequencies of the particle motion. Bottom graph: spectra of the forward scattering (upper trace) and back scattering (lower trace) of the LD light with the particle on the first tweezer. Top graph: spectrum of the forward scattering of the Nd:YAG light with the particle trapped by the Nd:YAG tweezer. Vertical dashed lines display the particle oscillation frequencies.

peaks associated with the nanoparticle motion in the three orthogonal directions defined by the trap geometry. In both cases, the background pressure is reduced down to 2 mbar to show such clear signatures of the under-damped motion.

3.3 Protocol reliability

We often observe that the particle scattered light changes suddenly during the transfer. On the other hand, a transfer between potential wells having the same minimal point should be characterized by a continuous change in the apparent particle brightness, following the varying light intensity. The observed abrupt changes indicate that the nanoparticle jumps between two potential minima, which are not perfectly superimposed due to an uncertainty in the positioning of the order of few hundred nanometers and to the optics mechanical vibrations. While turning off the LD, the potential barrier from the first to the second trap as well as the depth of the first trap becomes vanishingly small. To obtain a reliable transfer, the jump rate (favored by the lowering barrier) must be higher enough than the loss rate (increased by the lowering well depth). Moreover, the gas damping must be strong enough to allow the particle losing its kinetic energy during the transfer.

At the purpose of providing useful information for the reproduction of our method, we describe in the following a semi-quantitative investigation of the pressure and misalignment ranges that allow a reliable transfer. We first characterize the relative mechanical vibrations of the two trapping optics on the plane perpendicular to the optical axis. The two focusing systems are first placed at the position that maximizes the transmitted Nd:YAG power through the two fibers. The transmitted signal is then recorded while moving the second fiber head in the vertical direction. Hence, the fiber head is set at the position that halves the transmitted power, and the time trace of the transmitted signal is acquired and calibrated in terms of displacement fluctuations using the previously recorded transmission curve (as illustrated in the right inset of Fig.(10)). The same procedure is repeated for the horizontal displacement. In Fig.(10), we show the calculated displacement noise spectra. The main spectral feature is a double peak at $\sim$50 Hz for the vertical direction, whose area corresponds to a displacement of $\sim$ 50 nm (root mean square), much smaller than the beam waists. A simulation with a finite element model shows that the two peaks are due to flexural modes of the rod that sustains the first fiber head. In order to define the pressure range that allows a reliable transfer, we have repeated at least three times the transfer back and forth between the two traps at the pressure values of 100 mbar, 75 mbar, 50 mbar, 25 mbar, and

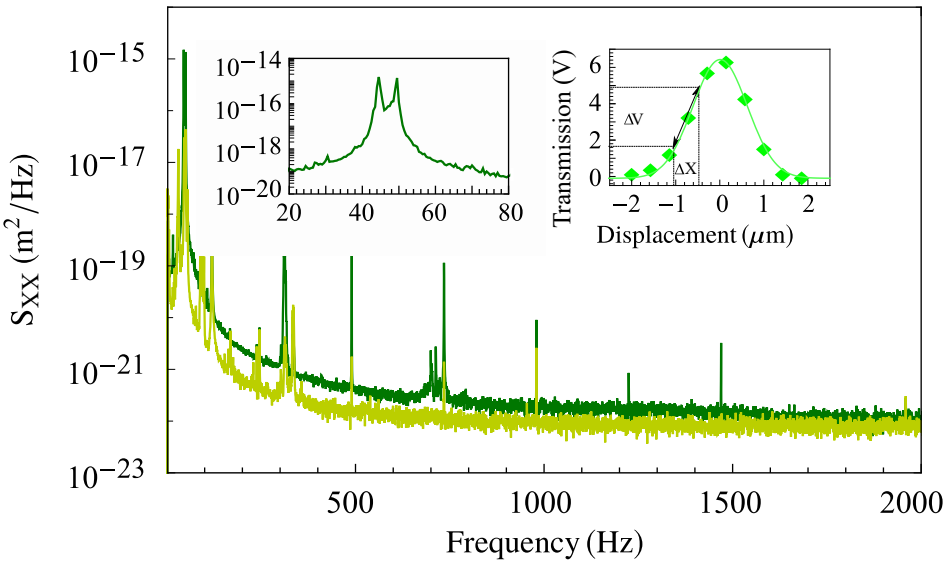

Figure 10: Spectra of the relative position between the two fiber heads, on the plane perpendicular to the tweezer axis, along the vertical (green) and horizontal (yellow) directions. Left inset: dominant vibrational modes at 44 Hz and 49 Hz in the vertical direction. Right inset: transmitted power of the Nd:YAG light through the two optical fibers, as the second fiber head is translated in the vertical direction. This curve is used to convert into displacement spectra the acquired transmission spectra, as illustrated in the picture.

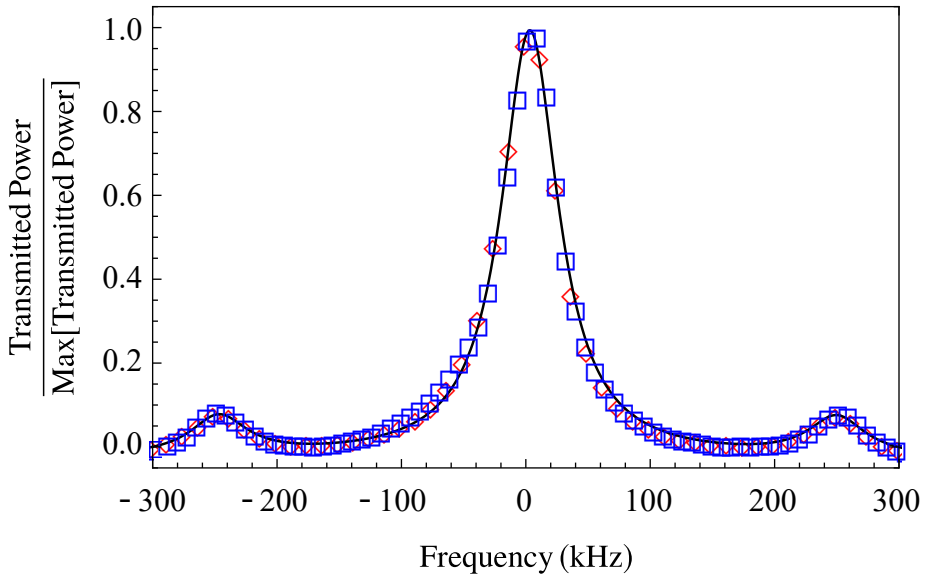

Figure 11: Transmitted power of a probe Nd:YAG laser through the high finesse optical cavity. Sidebands at ±250 kHz are produced by laser phase modulation for calibrating the frequency scan. The blue squares and red diamonds correspond to acquisitions recorded before the nanoparticle capture and transfer and after ten complete operations, respectively. The solid line shows a fit to the latter dataset.

15 mbar. We actually lost the particle during the fourth attempt at 10 mbar. We notice that at 10 mbar the damping rate is about $\Gamma \simeq 2\pi$ 10kHz ; thus, the particle motion is weakly damped. At 50 mbar, we have then evaluated the tolerance in the misalignment between the two fiber heads. Starting from the optimal position, we could transfer the particle three times back and forth in different relative positions until the two focuses were misplaced by $\sim 3\mu$m on the plane perpendicular to the optical axes or $\sim 10\mu$m along the optical axes. For the latter case, we show in Fig.(9), on the left panel, the time evolution of the backscattered light during a transfer from the LD to the Nd:YAG tweezers. The visible steps indicate a jump between the two potential wells occurring in a time shorter than 0.1 ms.

3.4 Final remarks

After having defined the above described transfer protocol, we have placed a ~ 50 mm long optical cavity (Finesse 54 000) inside chamber B. The cavity spacer has a 20 mm diameter radial hole that allows us to place on the cavity optical axis the nanoparticle trapped by the Nd:YAG tweezer. We have captured and transferred

several particles from the LD to the Nd:YAG trap at a background pressure of 30 mbar and eventually positioned them inside the cavity standing wave. In Fig.(11) we report two recordings of the cavity transmission function, acquired before the first and after the tenth transfer operation, where the measured width is 57 $\pm$ 1 kHz and 56 $\pm$ 1.5 kHz, respectively (the description of the cavity is postponed to the next chapter). As of now, even after $\sim$ 70 complete cycles, we could appreciate no degradation of the cavity finesse.

After the transfer, the arm is moved back, and the science chamber is isolated from the loading chamber and is pumped down to a pressure below 10^{-6} mbar in half an hour.

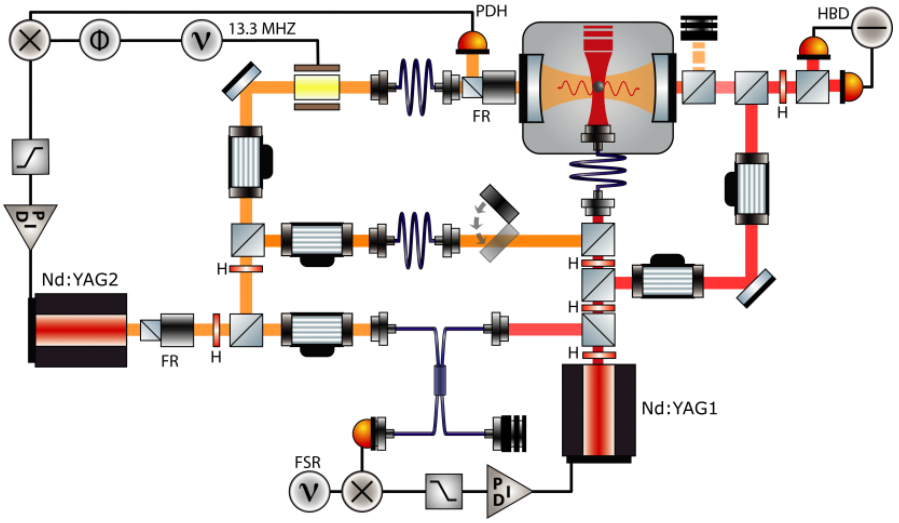

Figure 12: Scheme of the experimental setup. PDH: Pound-Drever-Hall detection, HBD: heterodyne balanced detection, FR: Faraday rotator, H: half-wave plate, FSR: sinusoidal wave generator at frequency corresponding to $\sim$ 1 cavity free-spectral-range.

4 The experimental setup

This section reports on the experimental setup that has been implemented for the cavity optomechanical experiment. Particular attention is paid to the full description of the detection apparatus, that has allowed to sense the motion at the quantum level.

4.1 The optical table

A simplified scheme of the experimental setup is shown in Fig.(12). From a first Nd:YAG laser we derive three beams, all of them frequency shifted by acousto-optic modulators and sent to the experimental bench by polarization-maintaining optical fibers. The first beam (reference) is phase modulated at 13.3 MHz, mode-matched to the cavity and used to frequency lock the laser to a cavity resonance by means of the Pound-Drever-Hall technique. The second beam is used for phase locking the second Nd:YAG laser (Nd:YAG2). At this purpose, it is mixed in a fibered beam-splitter with the radiation derived from Nd:YAG2, and detected by a fast photodiode. The beat note is down-converted in a mixer by a local oscillator at $\sim$ 3 GHz (one cavity free-spectral-range), and the IF output of the mixer is used in a servo loop acting on Nd:YAG2 for phase locking. The third beam is

superposed to the main tweezer light (supplied by Nd:YAG2), red detuned from a cavity resonance and used for stabilization purposes during the pumping down. The presence of two fields in the tweezer, red detuned from consecutive cavity resonances, provides indeed cooling along all the three directions for any position of the nanosphere, thanks to the two shifted standing waves. This third beam is blocked during the measurements.

Two weak beams are derived from Nd:YAG2. The first one is launched into an optical fiber and used for phase locking, as just described, the second one is frequency shifted by 1.1 MHz using a cascade of two acousto-optic modulators working on opposite orders, and it provides the local oscillator in a balanced heterodyne detection. The light transmitted by the cavity is mode-matched and overlapped to the local oscillator with orthogonal polarization, in a first polarizing beam-splitter. The resulting beam is then directed to the balanced detection setup, composed of a half-wave plate, a second polarizing beamsplitter, and a couple of photodetectors, whose signals are electronically subtracted.

Most of the Nd:YAG2 power is launched into a polarization maintaining fiber and used for the optical tweezer. The fiber is delivered into the experimental vacuum chamber, where its output is collimated and re-focused by the doublet of aspheric lenses mounted on the fiber FC connector.

4.2 Optical cavity

The optical cavity (depicted in Fig.(13)) is monolithic, built on a 48.8 mm long invar spacing cylinder with a radial hole allowing the inset of the tweezer. The two equal spheric mirrors (nominal curvature radius 25 mm) have measured transmission coefficient of 4.8×10^{-5}.

To analyse the transmission lineshape of the empty cavity, we overlap the reference laser beam and a fraction of the beam used for the tweezer, with orthogonal polarizations, before sending them to the cavity input. The reference beam is then locked to a cavity resonance, and the second laser, offset phase-locked to the reference, is scanned over the resonance of the subsequent longitudinal mode using the acousto-optic modulators. The transmission of the second beam is recorded and fitted to a Lorentzian function, as shown in Fig.(14), deriving the cavity width $\kappa/2\pi = 57.0 \pm 0.2$ kHz (Finesse 54000).

To estimate the birefringence, the procedure is repeated swapping the two polarizations. The distance between the two peak centers corresponds to twice the cavity birefringence (that results to be 28.4 ± 0.4 kHz), their mean value allows to

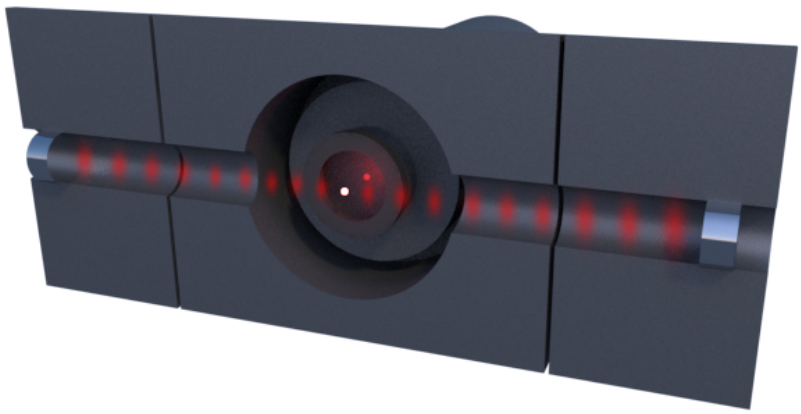

Figure 13: Rendering of the vertical cross section of the cavity, with the particle levitating in the optical potential on the cavity axis.

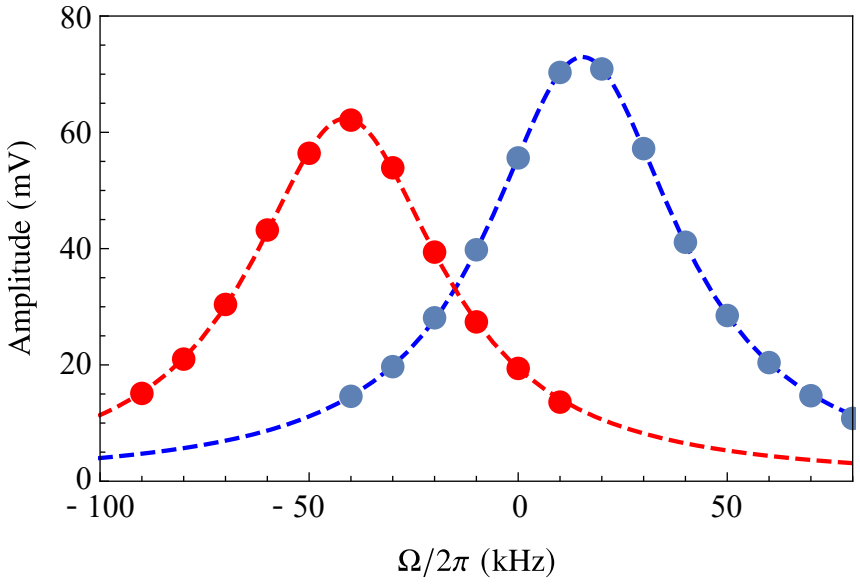

Figure 14: Detected intensity of the scanning Nd:YAG2 light transmitted by the cavity, when the reference laser is locked at resonance, as a function of the scanning frequency Ω (with an offset subtracted). Red (blue) symbols refer to p (s) polarized Nd:YAG2 light when the reference laser is s (p) polarized. Dashed lines show the fitting Lorentzian functions.

extract the cavity free-spectral-range. The tilt angle between the cavity vertical axis and the vertical axis of the optical table is 2°. Since the tweezer polarization lays nominally on the plane orthogonal to the optical table, we estimate a misalignment between the tweezer and the cavity axis on the order of a couple of degrees.

4.3 Heterodyne detection

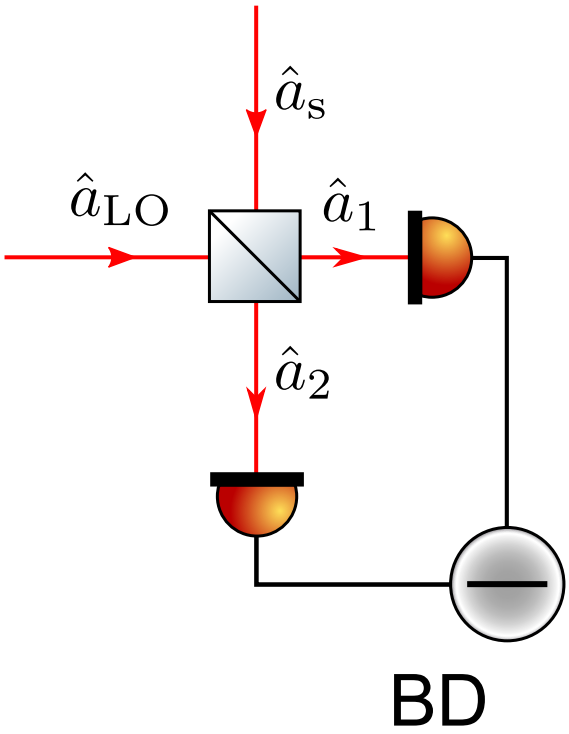

Figure 15: Heterodyne detection. The signal field transmitted by the cavity $\hat{a}_{\mathrm{s}}$ is mixed at the beam splitter with the local oscillator $\hat{a}_{LO}$. At the optimal configuration the output intensity is equally split between the two ports of the beam splitter. The heterodyne signal obtained subtracting electronically the photocurrents generated at the two detectors.

If the signal leaks out from the cavity at a rate κ, the output field is:

$$\hat{a}_{\mathrm{s}}(t) = \sqrt{\kappa}\hat{a} - \hat{a}_{\mathrm{v}},$$

where $\hat{a}$ ($\hat{a}_{\mathrm{v}}$) is the ladder operator of the cavity (vacuum) field. In the heterodyne detection setup, we make $\hat{a}_{\mathrm{s}}$ interfere with a strong local oscillator ($\hat{a}_{\mathrm{LO}}$) at the

beam splitter. The field at the output ports of the beam splitter is:

$$\begin{pmatrix} \hat{a}_1 \\ \hat{a}_2 \end{pmatrix} = \begin{pmatrix} i\sqrt{\mathrm{R}} & \sqrt{\mathrm{T}} \\ \sqrt{\mathrm{T}} & i\sqrt{\mathrm{R}} \end{pmatrix} \begin{pmatrix} \hat{a}_\mathrm{s} \\ \hat{a}_\mathrm{LO} \end{pmatrix},$$

where the relation $\mathrm{R}+\mathrm{T}=1$ for the reflectance and the transmittance of the beam splitter holds.

The photocurrent generated by the impinging photons at the j detector can be described as:

$$\hat{I}_j(t) = d_j\left[\hat{f}_j(t)\right],$$

where the detectors response is represented by the function d_j and $\hat{f}_j = \hat{a}_j^\dagger \hat{a}_j$ is the optical flux:

$$\begin{aligned} \hat{f}_1 &= \mathrm{R}\hat{f}_\mathrm{s} + \mathrm{T}\hat{f}_\mathrm{LO} + i\sqrt{\mathrm{RT}}\left[e^{i\Omega_\mathrm{LO}t}\hat{a}_\mathrm{s}\hat{a}_\mathrm{LO}^\dagger - e^{-i\Omega_\mathrm{LO}t}\hat{a}_\mathrm{s}^\dagger\hat{a}_\mathrm{LO}\right], \\ \hat{f}_2 &= \mathrm{T}\hat{f}_s + \mathrm{R}\hat{f}_\mathrm{LO} - i\sqrt{\mathrm{RT}}\left[e^{i\Omega_\mathrm{LO}t}\hat{a}_\mathrm{s}\hat{a}_\mathrm{LO}^\dagger - e^{-i\Omega_\mathrm{LO}t}\hat{a}_\mathrm{s}^\dagger\hat{a}_\mathrm{LO}\right], \end{aligned}$$

with the field operators expressed in the rotating frame and $\Omega_\mathrm{LO} = \omega_\mathrm{LO} - \omega_\mathrm{s}$ the frequency difference between the local oscillator and cavity field.

The current generated at the two detectors can be electronically summed or subtracted. The AC signal in the Fourier domain for a linear response of the electronics reads:

$$\delta\tilde{I}^{\mp}(\omega) = \tilde{F}(\omega)\left[\delta\tilde{f}_1(\omega) \mp \xi(\omega)\,\delta\tilde{f}_2(\omega)\right],$$

where $\tilde{F}(\omega)$ is the overall response function of the electronics, $\xi(\omega)$ takes into account slight differences in the response of the two detectors and $\delta\hat{f}_i$ the ith flux fluctuations. Expanding the field operators around their mean value, $\hat{a}_i = \alpha_i + \delta\hat{a}_i$ with $\alpha_i = \langle\hat{a}_i\rangle$, the difference/sum signal reads:

$$\begin{aligned} \delta\tilde{I}^{\mp}(\omega) = \alpha_\mathrm{LO}\tilde{F}(\omega)\Big\{&(\mathrm{T}\mp\xi\mathrm{R})\left[\delta\tilde{a}_\mathrm{LO}(\omega) + \delta\tilde{a}_\mathrm{LO}^\dagger(-\omega)\right] + \\ &+ i\sqrt{\mathrm{RT}}\,(\xi\pm 1)\left[\delta\tilde{a}_\mathrm{s}(\omega+\Omega_\mathrm{LO}) - \delta\tilde{a}_\mathrm{s}^\dagger(\omega-\Omega_\mathrm{LO})\right]\Big\}, \end{aligned} \quad (4.1)$$

with the approximation $\alpha_\mathrm{LO} \gg \alpha_\mathrm{s}$, assuming $\alpha_\mathrm{LO} \in \mathbb{R}$ and neglecting the second order fluctuating terms.

For R $\simeq$ T the sum signal PSD reads:

$$S^{+}|_{\mathrm{R}\simeq\mathrm{T}} \equiv S_{\mathrm{LO}} = \lim_{\tau\to\infty} \frac{1}{\tau}\langle \delta\left(\tilde{I}^{+}\right)^{\dagger}(\omega)\,\delta\left(\tilde{I}^{+}\right)(\omega)\rangle,$$

while the difference signal gives the heterodyne spectrum:

$$S^{-}|_{\mathrm{R}\simeq\mathrm{T}} \equiv S_{\mathrm{het}} = \lim_{\tau\to\infty} \frac{1}{\tau}\langle \delta\left(\tilde{I}^{-}\right)^{\dagger}(\omega)\,\delta\left(\tilde{I}^{-}\right)(\omega)\rangle.$$

Since the signal field fluctuations depend on the mechanical motion $\delta\tilde{a}_{\mathrm{s}} \sim \tilde{x}$, the heterodyne detection gives the PSD of the mechanical motion $S_{\mathrm{het}} \sim S_{xx}(\omega + \Omega_{\mathrm{LO}}) + S_{xx}(-\omega + \Omega_{\mathrm{LO}})$, where the fast rotating terms have been neglected.

4.3.1 Detection efficiency

As for the inefficiencies of the system, can be treated considering that the signal field impinges on a two port beams splitter, so that:

$$\hat{a}_{\mathrm{s}}^{\mathrm{exp}} = \sqrt{\eta}\hat{a}_{\mathrm{s}} + \sqrt{1-\eta}\hat{a}_{\mathrm{v}},$$

where $\hat{a}_{\mathrm{v}}$ is the vacuum field that enters from the port of the BS that represents the loss channel, characterized by a transimission coefficient η. The experimentally measured signal is:

$$S_{\mathrm{het}}^{\mathrm{exp}} = \eta S_{\mathrm{het}} + (1-\eta).$$

The efficiency of the heterodyne detection is determined by:

- Cavity efficiency: $\eta_{\mathrm{cav}} = \kappa_{\mathrm{out}}/\kappa$. Its value of 0.41 is evaluated measuring the ratio between the input (P_{IN}) and output (P_{OUT}) optical power at resonance. Assuming symmetric mirrors:

  $$\frac{P_{\mathrm{OUT}}}{P_{\mathrm{IN}}} = T^2\eta_{\mathrm{mc}}\left(\frac{\mathcal{F}}{\pi}\right)^2,$$

  where η_{mc} is the mode matching of the cavity, T is the transmission coefficient of the mirrors and $\mathcal{F}$ is the cavity Finesse.

- Collection efficiency: $\eta_{\mathrm{col}} = P_{\mathrm{det}}/P_{\mathrm{OUT}}$. It is readily estimated measuring amount of the power that leaks out the cavity P_{OUT} that is collected at the detectors P_{det}.

- Spatial matching between the local oscillator and the signal field : η_{m}. Its value is determined by the beat note between the local oscillator and the cavity output field at the heterodyne detectors:

$$Sig = 2I\left[1 + \eta_{\mathrm{m}} \cos\left(\Omega t\right)\right],$$

  where the intensities of both beams is equal to I, their frequency difference is set to Ω and $\eta_{\mathrm{m}} = \iint_{-\infty}^{+\infty} dx\, dy f_{\mathrm{LO}} f_{\mathrm{sig}}$ is the overlap integral on the detector surface between the spatial profile amplitudes of the two beams. Defining $\bar{I} = 2I$ and I_{pp} the peak to peak amplitude of the beat note, the efficiency is $\eta_{\mathrm{m}} = \frac{I_{\mathrm{pp}}}{2\bar{I}}$.

- Photodiodes quantum efficiency: $\eta_{\mathrm{PD}} \simeq 1$.

So, the overall detection efficiency is the product of these terms:

$$\eta = \eta_{\mathrm{cav}} \eta_{\mathrm{col}} \eta_{\mathrm{m}} \eta_{\mathrm{PD}}.$$

4.3.2 Intensity noise calibration

We have measured the amplitude fluctuations value using the shot level for calibration: sending only the local oscillator to the heterodyne detection, the ratio in the PSD between the sum and the difference signal is:

$$\frac{S^+}{S^-} = \frac{S_{X_{\mathrm{LO}}}}{S_{X_{\mathrm{v}}}},$$

where the quadrature operator is defined as $X = \frac{\delta\hat{a} + \delta\hat{a}^\dagger}{2}$. Since the spectrum of the relative amplitude fluctuations is $S_\epsilon = 4S_{X_{\mathrm{LO}}}/\alpha_{\mathrm{LO}}$, we get

$$S_\epsilon = 4S_{X_{\mathrm{v}}} \frac{S^+}{S^-} \frac{\hbar\omega_{\mathrm{LO}}}{P_{\mathrm{LO}}}$$

The measured RIN (Relative Intensity Noise) of the tweezer laser is $S_\epsilon = 2.3 \times 10^{-14}$ Hz^{-1} in the spectral region of interest. The intensity noise spectrum at twice the oscillation frequency causes parametric heating of the nanosphere motion. The heating rate, calculated as $\Gamma_{\mathrm{RIN}} = 0.25\,\Omega^2 S_\epsilon$ [56], is below 1 Hz, and it is therefore negligible.

4.3.3 Optimal rejection

Ideally $\xi = 1$ and the heterodyne signal can be totally decoupled form the local oscillator fluctuations. In the real world, however, response unbalances for the two detectors are always present and the amount of LO noise in the signal at the optimal configuration has to be quantified.

We have determined the configuration of R and T that minimizes in the spectrum of the difference signal an externally driven amplitude fluctuation in the frequency region of interest by rotating the half wave plate of the balanced detection.

The common mode rejection ratio at 1 MHz and the spectral power integrated between 0.7 and 1.5 MHz are shown in Fig.(16) as a function of the linear polarization angle at the input of the polarizing beam-splitter of the balanced detection, varied by tuning the angle of the half-wave plate and monitoring the DC output of the balanced detection. This angle is then kept at $0.3^\circ \pm 0.1^\circ$ during all the measurements. In this range, the common mode rejection is 40 dB, i.e.

$$\left|\frac{\mathrm{T} + \xi\mathrm{R}}{\mathrm{T} - \xi\mathrm{R}}\right|^2 \simeq \frac{4}{|1-\xi|^2} = 40\mathrm{dB}.$$

4.3.4 Quantum noise calibration

In Fig.(17) we show the spectrum recorded by the balanced detection with just the local oscillator, i.e., with vacuum noise as input signal and the local oscillator power of 4.5 mW . The spectrum nominally corresponds to the reference shot noise, filtered by the overall transfer function of the detectors and the following electronics. Its polynomial fitting function, shown in the figure, is indeed used to normalize the heterodyne spectra to vacuum noise.

Considering the RIN and the power of the local oscillator, we calculate that the residual amplitude noise at the output of the balanced detection is $\sim 3\%$ of the shot noise level. This is in agreement with the directly measured spectral power, shown in Fig.(18) for increasing detected power.

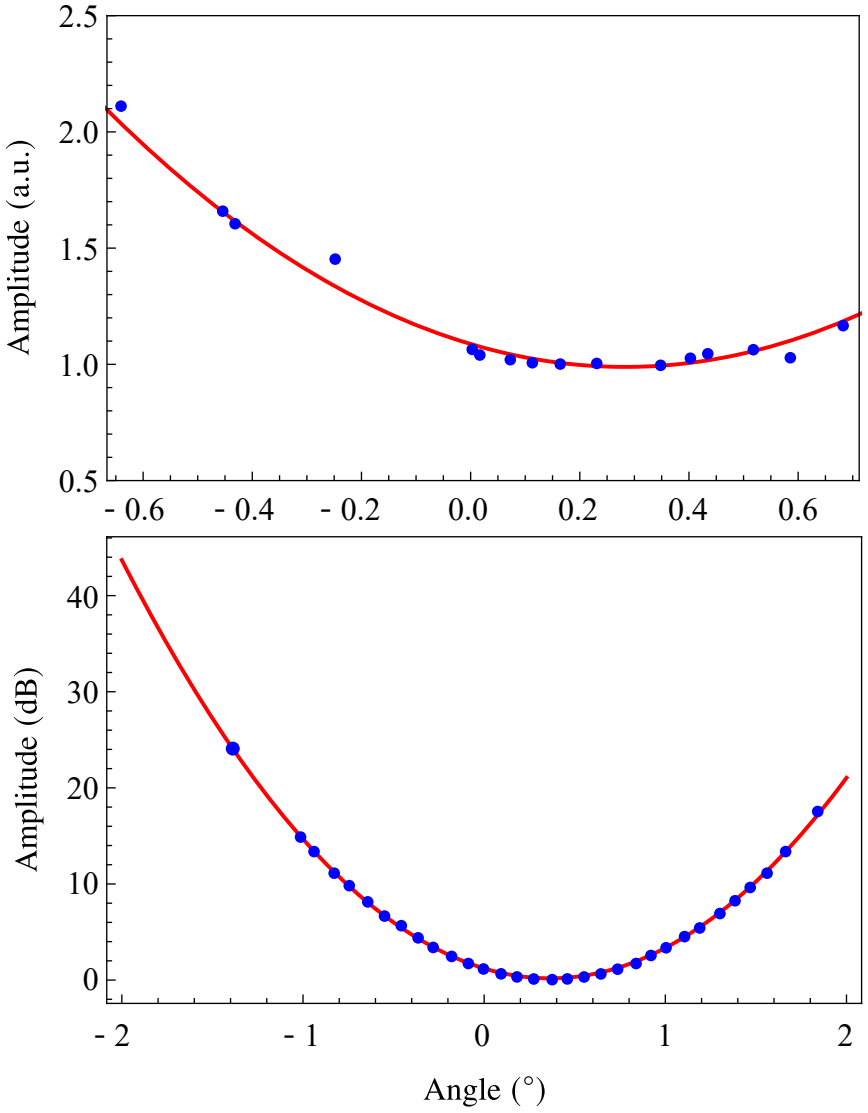

Figure 16: Spectral power of the local oscillator, measured at the output of the balanced detection and integrated between 0.7 and 1.5 MHz (upper panel), and amplitude of an intensity modulation peak at 1 MHz (lower panel), as a function of the angle of the input linear polarization in the balanced detection. Both signals are normalized to their minimum value. Red solid lines show the sinusoidal fitting functions.

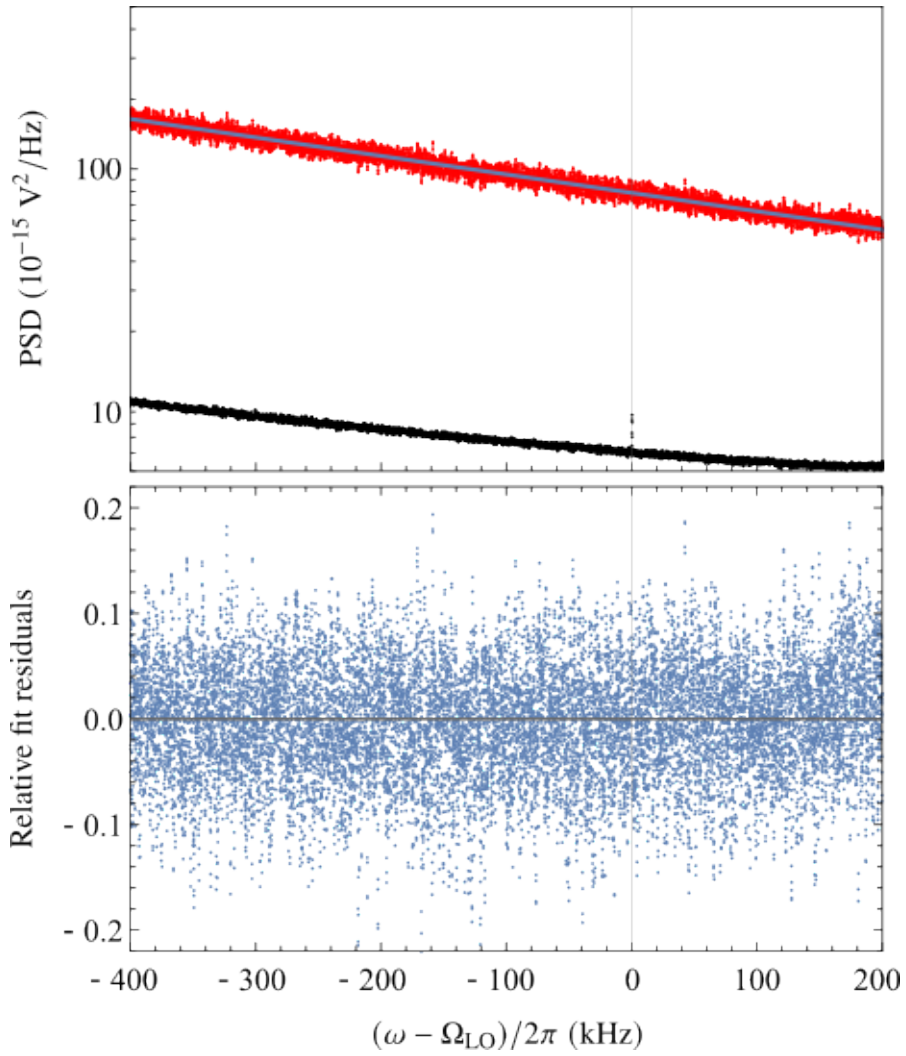

Figure 17: Red trace: spectrum of the local oscillator at the output of the balanced detection. The solid line shows the fitting polynomial curve, the fitting relative residuals are shown in the lower panel. Black trace: electronic noise.

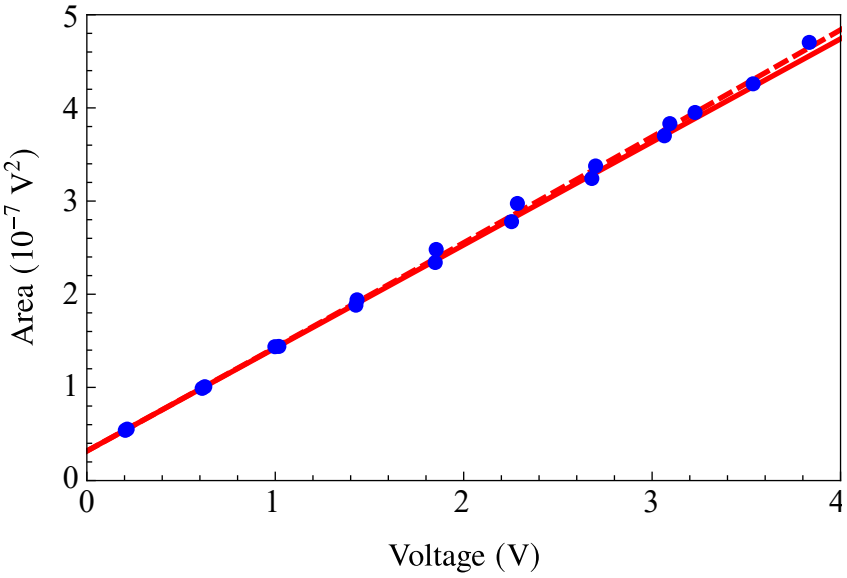

Figure 18: Spectral power of the local oscillator, measured at the output of the balanced detection and integrated between 0.7 and 1.5 MHz, as a function of the dc signal in the photodiodes. The red solid line shows the linear interpolation to the data, the dashed line the parabolic fit that indicates an excess noise equivalent to 3% of the shot noise, at the maximum detected power that corresponds to 4.5 mW.

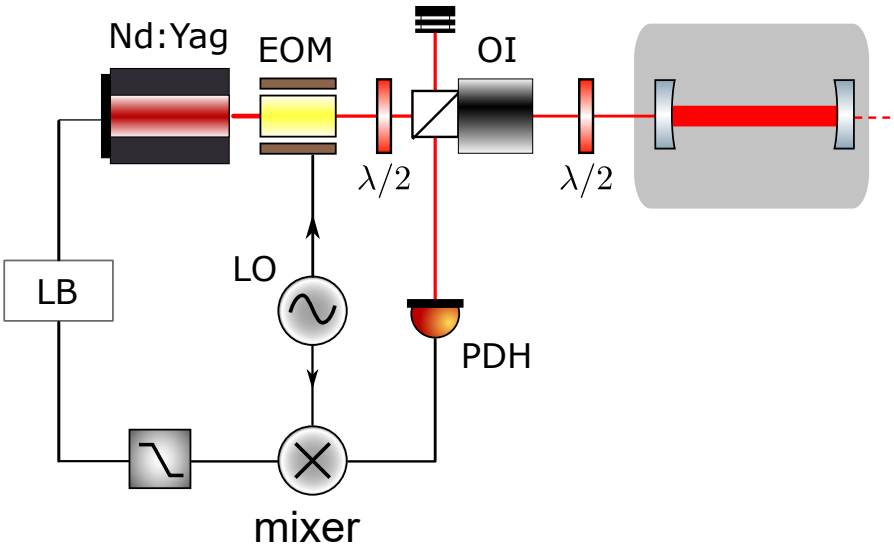

Figure 19: Cavity locking via the PDH technique. The laser light is modulated at the frequency Ω by means of the EOM. The back reflected beam, deflected by the optical isolator (OI), is detected at the photodiode (PDH). The electronic signal, downconverted via the mixer, is sent to the lock-box, which controls the laser driver.

4.4 Locking schemes

4.4.1 Cavity locking

The laser frequency is stabilized through the Pound-Drever-Hall (PHD) technique [17]. For a symmetric cavity, i.e. two equal mirrors, if the laser light impinging at the input cavity mirror is written as $E_{\rm in} = E_0 e^{i\omega t}$, the field that comes back leaking through the input cavity mirror reads:

$$E_{\rm ref} = E_{\rm in} F(\omega) = E_{\rm in} \frac{r}{1 - r^2 e^{i\omega/\mathrm{FSR}}} \left(e^{i\omega/\mathrm{FSR}} - 1 \right), \tag{4.2}$$

where r is the mirrors reflectivity. By means of an electro optic modulator (EOM) the phase of the impinging field is modulated at the frequency Ω. Expressing the modulated field with the Bessel functions (J_i) and retaining only the slow rotating terms, the impinging field can be re-expressed as:

$$E_{\rm in} = E_0 e^{i(\omega t + \beta \sin \Omega t)} \simeq E_0 e^{i\omega t} \left(J_0(\beta) + J_1(\beta) e^{i\Omega t} - J_1(\beta) e^{-i\Omega t} \right).$$

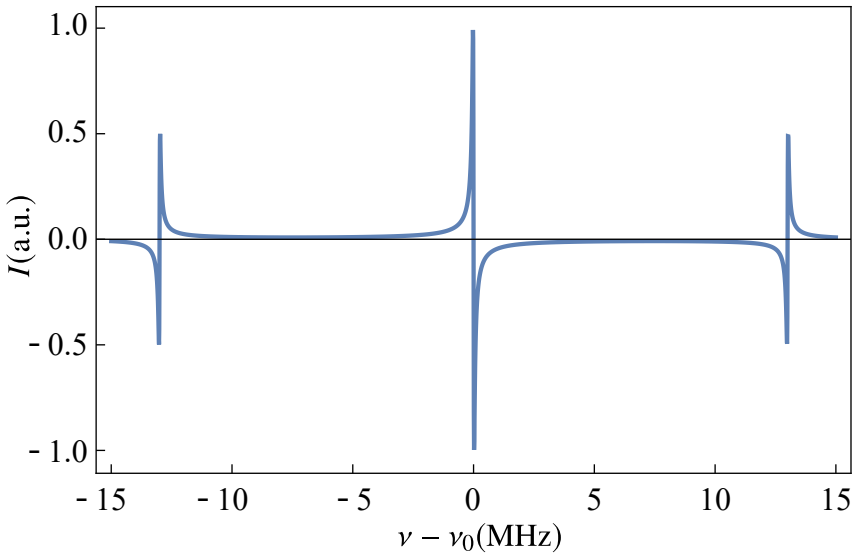

Figure 20: Simulated PDH signal.

As such, the reflected beam (Eq.(4.2)) reads

$$E_{\text{ref}} \simeq E_0 e^{i\omega t}\left(F(\omega)J_0(\beta) + F(\omega+\Omega)J_1(\beta)e^{i\Omega t} - F(\omega-\Omega)J_1(\beta)e^{-i\Omega t}\right).$$

The back reflected field is detected, giving a signal

$$\begin{aligned} Sig \propto\ & I_{\text{p}}\left|F(\omega)\right|^2 + I_{\text{s}}\left(\left|F(\omega+\Omega)\right|^2 + \left|F(\omega-\Omega)\right|^2\right) + \\ & + 2\sqrt{I_{\text{p}}I_{\text{s}}}\text{Re}\left[F(\omega)F^*(\omega+\Omega) - F^*(\omega)F(\omega-\Omega)\right]\cos\Omega t + \\ & + 2\sqrt{I_{\text{p}}I_{\text{s}}}\text{Im}\left[F(\omega)F^*(\omega+\Omega) - F^*(\omega)F(\omega-\Omega)\right]\sin\Omega t, \end{aligned}$$

with $I_{\text{p(s)}}$ the intensity of the main (secondary) band. The fast oscillating terms have been neglected.

Demodulating this signal at the drive frequency Ω with the proper phase, we can retain only the term

$$\text{Im}\left[F(\omega)F^*(\omega+\Omega) - F^*(\omega)F(\omega-\Omega)\right],$$

that is plotted in Fig.(20). In the vicinity of the cavity resonance the frequency difference between the cavity resonance and the laser light is linearly converted into an electronic signal which is processed via the electronic circuit reported in appendix C. and fed back to the driver of the laser, thus stabilizing the emitted

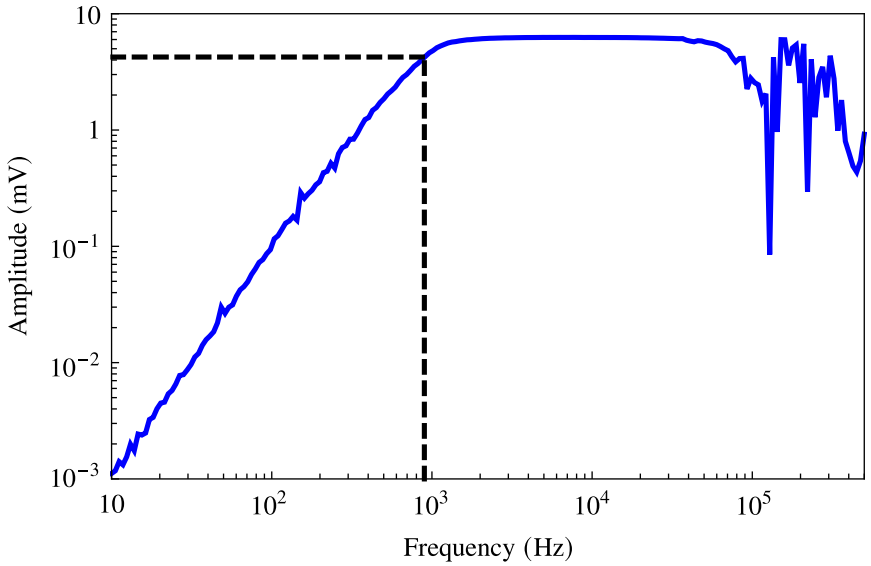

Figure 21: Bandwidth of the cavity locking: a modulation signal is sent to the Fast controller of the laser. The recorded PDH error signal is down converted at the modulation frequency. The cut-off frequency is estimated at $\sim$ 900Hz, where the amplitude decreases of a factor $\sqrt{2}$ with respect to the value on the plateau (dashed lines).

frequency. In Fig.(21) is reported the measurement of the lock bandwidth.

4.4.2 Phase and frequency locking

The schematic is represented in Fig.(22). The light of the two Mephisto lasers (ML1 ML2) interfere at the fast detector FPD, generating the electrical signal:

$$V_{\mathrm{b}} = V_0 \sin\left[\delta\phi\left(t\right)\right],$$

where $\delta\phi\left(t\right)$ is the phase difference between the two lasers, which includes a linear drift due to the different frequencies.

To set up the locking scheme, this signal is mixed with a reference oscillator of frequency FSR $-$ 10MHz. The output is split by means of the power splitter (PS) and sent either to the phase lock or frequency lock control loop:

- **phase lock**: to get the error signal for the phase lock, the signal is down converted to DC by means of a second mixer, driven by a 10MHz oscillator:

$$e_\phi = e_0 \sin\left[\delta\phi\left(t\right) - 2\pi \text{ FRS } t\right].$$

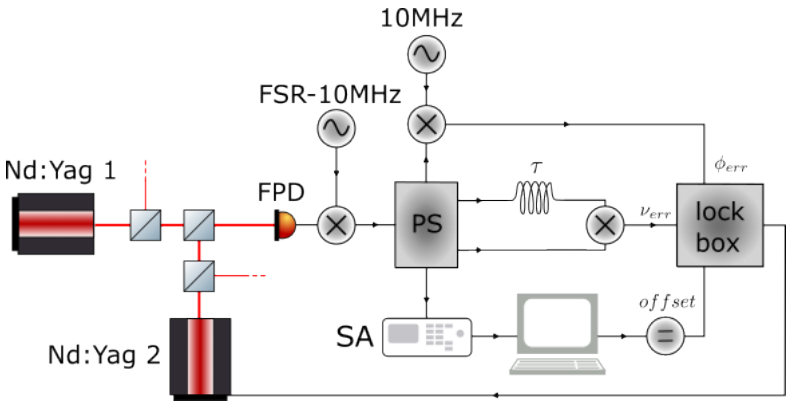

Figure 22: Phase and Frequency locking scheme: the optical beating between the two lasers is detected and down converted by mean of on oscillator of frequency FSR-10 MHz. The down converted signal is sent to the power splitter (PS). For the phase locking, the beating is down converted again by means of a second oscillator of frequency 10 MHz and sent to the Lock Box. at the fast detector. For the frequency locking, the PS output is sent to the Lock Box via an interferometer. The interferometer thermal drifts is monitored by means of a frequency meter of a spectrum analyser (SA) and corrected with a dc signal sent to the auxiliary input of the Lock Box.

- **frequency lock**: to get the error signal proportional to the frequency difference between the two lasers, an interferometric measurement of the PS output has been realized: the signal is split between two transmission lines with a relative time lag of $\sim$ 50ns. The low frequency signal at the IF output of the mixer reads:

$$\sin\left[2\pi\nu/\tilde{\nu}\right],$$

where ν is the beat note frequency at the output of the PS, $\tilde{\nu} = v/L$ is the characteristic frequency of the interferometer, L is the length difference between the two arms and v the propagation velocity of the RF signal through the interferometer. Because of thermal drifts, $\tilde{\nu}$ fluctuates around the ideal set point $\hat{\nu} = 10\text{MHz}$. Taylor expanding the reference frequency around $\hat{\nu}$, the error signal is:

$$e_\nu = \sin\left[2\pi\frac{\nu}{\hat{\nu}}\right] - 2\pi\frac{\nu}{\hat{\nu}}\frac{\delta\hat{\nu}\left(\mathrm{T}\right)}{\hat{\nu}}.$$

To counteract the slow thermal drifts, $\delta\hat{\nu}\left(\mathrm{T}\right)$, the beating is continuously monitored with a frequency meter and an offset is added to the error signal to correct it.

The PI electronic scheme (lock box) is reported in appendix B.

5 Quantum motion of a levitated nanosphere on the plane

This chapter reports on the experimental observations with the optomechanical system that has been developed during the thesis. As stated in the introductory section, in cavity optomechanics polariton modes originate from the quantum-coherent coupling of a macroscopic mechanical vibration to the cavity radiation field [70, 41]. Here, we investigate polaritonic modes in the motion of an optically-levitated nanosphere [2, 12, 4, 54, 35, 21, 44] in the regime of coherent quantum coupling. The particle is trapped in high vacuum by an optical tweezer and strongly coupled to a single cavity mode by coherent scattering of the tweezer photons [16, 75, 22, 15, 53]. The two-dimensional motion and the optical cavity mode define an optomechanical system with three degrees of freedom. In the strong coupling regime, we observe hybrid light-mechanical states with a vectorial nature. Rather than just focussing on the non classical signatures of the mechanical oscillator, care should be taken to the optomechanical platform as a whole. In fact, it may be exploitable for quantum information experiments performed at room temperature.

5.1 Overview

The results presented here concern the research work reported in [51, 50] and more recent observations. Because of the complementarity of the topics the observations could be, in principle, the output of an individual experimental run. As such, they are presented as the story of a single, ideal, experiment. Let's suppose that the particle has just been delivered to the tweezer in the experimental chamber, the experimental run would go like this:

- positioning of the particle on the cavity axis;
- data acquisition in mid vacuum to observe the hybrid optomechanical states in the classical regime;
- evacuation of the chamber to reach high vacuum;
- exploration of the optomechanical system physics in the quantum coherent regime.

For the seek of clarity the theory is presented when necessary, along with the experimental results.

As final remark, the different measurements were realized on different nanoparticles, thus leading to slight variations in the coupling strength values. These discrepancies are attributed to the imprecision in the positioning procedure of the particle on the cavity axis.

5.2 Placing the particle on the cavity axis

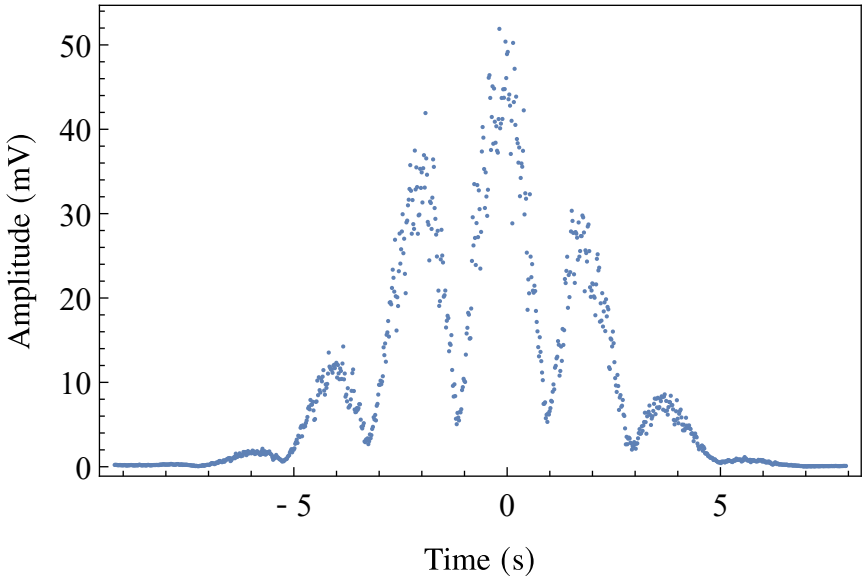

Figure 23: Amplitude of the beat note at 1.1 MHz between the tweezer light, scattered by the nanosphere and transmitted through the cavity output mirror, and the local oscillator. The nanosphere is moved through the cavity standing wave using the tweezer positioner.

The optical system of the trap is movable along three axes using nanometric vacuum positioners. Its displacement along the cavity is calibrated by observing the beat note between the light scattered by the nanosphere on the cavity mode and transmitted through the output mirror, and the local oscillator. The amplitude of such beat note is proportional to the field amplitude of the standing wave at the nanosphere position. An example of the beat note amplitude recorded while moving the positioner, nominally along the tweezer axis, is shown in Fig.(23). We see the Gaussian envelop with a width given by the cavity waist, and a modulation reflecting the sinusoidal standing wave, due to a slight misalignment between the

axis of the positioner and the cavity transverse plane. The particle is placed on the axis when the beat note is at the center of the gaussian envelope along the two orthogonal directions on the plane perpendicular to the cavity axis. Once there, the particle is placed on the node and the auxiliary laser beam, a fraction of light coming from the laser used for the cavity locking, is unblocked. The particle motion is now optomechanically damped along the three directions and the chamber is gently evacuated starting from the initial pressure of 1mbar.

5.3 theoretical model

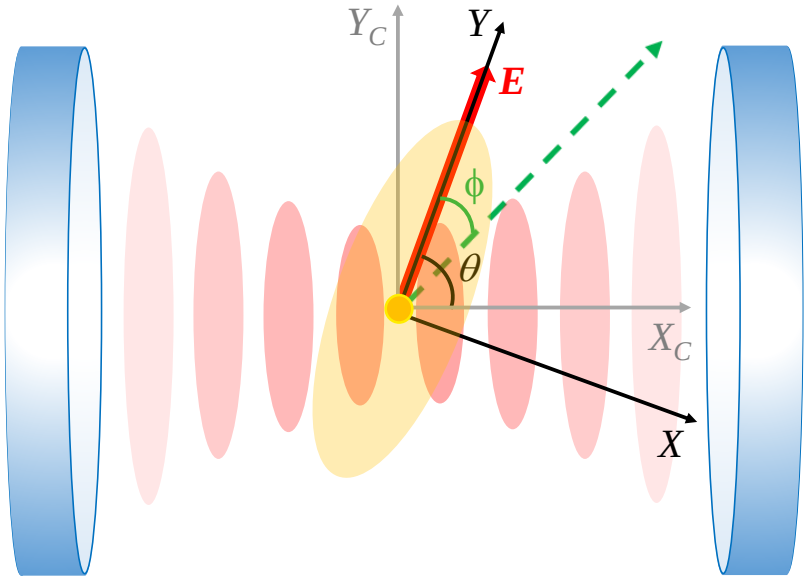

Figure 24: Scheme of the experimental system. A silica nanosphere levitates on the optical potential created by the light of an optical tweezer, propagating along the Z axis, with the electric field along the Y axis. The nanosphere is positioned on the axis of an optical cavity (which defines the direction X_C), in correspondence of a node of the field of a cavity mode. The angle ϕ defines a generic direction in the transverse plane $X - Y$.

Even if the (approximated) analytical expressions are obviously useful to understand the system behaviour and guide the experiments, a correct quantitative

study requires the comparison of the experimental spectra with those generated by a full model, the consequent extraction of the system parameters, and finally the inference of the characteristics of the motion (in particular, the effective thermal occupancy) from the model.

For the purpose of reproducing the experimental results, the oscillation of the nanosphere in the optical potential created by the tweezer and its interaction with the mode of the cavity field, that is close to resonance with the tweezer light, can be described by a standard quantum Langevin model.

The Hamiltonian of the three interacting oscillators (one optical and two mechanical) is

$$H = -\hbar\Delta\hat{a}_{\rm c}^{\dagger}\hat{a}_{\rm c}+\hbar\Omega_1 b_X^{\dagger}b_X+\hbar\Omega_2 b_Y^{\dagger}b_Y+\hbar g_X(\hat{a}_{\rm c}^{\dagger}+\hat{a}_{\rm c})(b_X^{\dagger}+b_X)+\hbar g_Y(\hat{a}_{\rm c}^{\dagger}+\hat{a}_{\rm c})(b_Y^{\dagger}+b_Y)\,.$$

where $\hat{a}_{\rm c}$ (b_i, $i = X, Y$) are the bosonic operators of the optical (mechanical) oscillators, Ω_i the mechanical angular frequencies and g_i the optomechanical coupling rates.

The quantum Langevin model is derived from the Hamiltonian by adding the input terms. The linearised evolution equations for the motion in the plane orthogonal to the tweezer axis, expressed in the frame rotating at the laser frequency Ω_L, can be written as

$$\dot{\hat{a}}_{\rm c} = \left(i\Delta - \frac{\kappa}{2}\right)\hat{a}_{\rm c} + ig_X(\hat{b}_X + \hat{b}_X^{\dagger}) + ig_Y(\hat{b}_Y + \hat{b}_Y^{\dagger}) + \sqrt{\kappa}\,\hat{a}_{\rm IN}$$

$$\dot{\hat{b}}_j = \left(-i\Omega_j - \frac{\gamma_j}{2}\right)\hat{b}_j + ig_j(\hat{a}_{\rm c} + \hat{a}_{\rm c}^{\dagger}) + \sqrt{\Gamma_j}\,\hat{b}_{{\rm n},j} \tag{5.1}$$

where Γ_j is the overall mechanical heating rate. The $\hat{b}_j$ are linked to the operators describing the displacements (x, y) and the momenta (p_x, p_y) along the X and Y directions by the relations

$$x = x_{\rm zpf}(\hat{b}_X + \hat{b}_X^{\dagger}) \tag{5.2}$$

$$p_x = ip_{\rm zpf}^{x}(\hat{b}_X^{\dagger} - \hat{b}_X) \tag{5.3}$$

where $x_{\rm zpf} = \sqrt{\frac{\hbar}{2m\Omega_X}}$ and $p_{\rm zpf}^{x} = \sqrt{\frac{\hbar m\Omega_X}{2}}$ are the zero-point position and momentum fluctuations of the free oscillators, and by equivalent expressions for y and p_y.

We note that while the operators $\hat{b}_j$ can be thought of as phonon annihilation

operators in the limit of weak optomechanical coupling, such an interpretation is not straightforward in the strong coupling regime.

The input noise operators are characterized by the correlation functions

$$\begin{aligned} \langle \hat{a}_{\mathrm{IN}}(t)\hat{a}^{\dagger}_{\mathrm{IN}}(t')\rangle &= \delta(t-t') \\ \langle \hat{a}^{\dagger}_{\mathrm{IN}}(t)\hat{a}_{\mathrm{IN}}(t')\rangle &= 0 \\ \langle \hat{b}^{\dagger}_{\mathrm{n},j}(t)\hat{b}_{\mathrm{n},j}(t')\rangle = \langle \hat{b}_{\mathrm{n},j}(t)\hat{b}^{\dagger}_{\mathrm{n},j}(t')\rangle &= \delta(t-t') \end{aligned}$$

The total decoherence rates can be written as

$$\Gamma_j = \frac{k_{\mathrm{B}}T}{\hbar\Omega_j}\,\gamma_j + \Gamma_{\mathrm{n}j} \tag{5.4}$$

where the first contribution is due to scattering with the background gas molecules which damps the motion at a rate γ_j, and $\Gamma_{\mathrm{n}j}$ accounts for the shot noise in the dipole scattering (which adds negligible damping), as well as for additional technical noise sources. We note that in Eq.(5.4) we are dealing with noise in a classical way, justified by the fact that $k_{\mathrm{B}}T \gg \hbar\Omega_j$.

As discussed, the X_C-Y_C framework can be more appropriate to understand the physics of the system and to describe it by means of approximated analytical expressions. However, we remark that in the X-Y framework the input noise sources are uncorrelated and easily evaluated, and it is therefore more suitable for exact numerical calculations.

From the Langevin model and the input/output relation for the transmitted field we calculate the heterodyne spectra, that are shown in the next sections and display an excellent agreement with the experimental data.

In the parameters range that assures the system stability, the stationary evolution equations can be written in the Fourier space in the compact matrix form as

$$(-i\Omega\,\mathbf{I} + \mathbf{D})\,\mathbf{V} = \mathbf{V}_{\mathrm{IN}} \tag{5.5}$$

where $\mathbf{I}$ is the identity matrix of order 6, the drift matrix is

$$\mathbf{D} = \begin{pmatrix} -i\Delta+\kappa/2 & 0 & -ig_X & -ig_X & -ig_Y & -ig_Y \\ 0 & i\Delta+\kappa/2 & ig_X & ig_X & ig_Y & ig_Y \\ -ig_X & -ig_X & i\Omega_X+\gamma_x/2 & 0 & 0 & 0 \\ ig_X & ig_X & 0 & -i\Omega_X+\gamma_x/2 & 0 & 0 \\ -ig_Y & -ig_Y & 0 & 0 & i\Omega_Y+\gamma_y/2 & 0 \\ ig_Y & ig_Y & 0 & 0 & 0 & -i\Omega_Y+\gamma_y/2 \end{pmatrix},$$

the intracavity vector is $\mathbf{V} = (\tilde{a}_{\rm c}, \tilde{a}_{\rm c}^\dagger, \tilde{b}_X, \tilde{b}_X^\dagger, \tilde{b}_Y, \tilde{b}_Y^\dagger)$ where $\tilde{O}(\Omega)$ is the Fourier transformed of the operator $\hat{O}(t)$ and $\tilde{O}^\dagger(\Omega) = \left(\tilde{O}(-\Omega)\right)^\dagger$ is the Fourier transformed of $\hat{O}^\dagger(t)$. The input noise vector $\mathbf{V}_{\rm IN}$ is defined as

$$\mathbf{V}_{\rm IN} = (\sqrt{\kappa}\,\tilde{a}_{\rm IN}, \sqrt{\kappa}\,\tilde{a}_{\rm IN}^\dagger,\ \sqrt{\Gamma_X}\,\tilde{b}_{{\rm n},X}, \sqrt{\Gamma_X}\,\tilde{b}_{{\rm n},X}^\dagger, \sqrt{\Gamma_Y}\,\tilde{b}_{{\rm n},Y}, \sqrt{\Gamma_Y}\,\tilde{b}_{{\rm n},Y}^\dagger),$$

and $\mathbf{V}$ is found by inverting Eq.(5.5), i.e., $\mathbf{V} = (-i\Omega\,\mathbf{I} + \mathbf{D})^{-1}\,\mathbf{V}_{\rm IN}$. The total cavity output field is $\hat{a} = \sqrt{\kappa}\hat{a}_{\rm c} - \hat{a}_{\rm IN}$, from which:

$$\tilde{a} \;=\; \left(\frac{\kappa}{-i\Omega - i\Delta + \kappa/2} - 1\right)\tilde{a}_{\rm IN} \;+\; i\sqrt{\kappa}\frac{g_X(\tilde{b}_X + \tilde{b}_X^\dagger) + g_Y(\tilde{b}_Y + \tilde{b}_Y^\dagger)}{-i\Omega - i\Delta + \kappa/2}. \qquad (5.6)$$

The full model is necessary to correctly derive the output spectra, and the behavior of single components of the system (such as the nanoparticle motion) can just be extracted from the model, provided that it accurately describe the experimental observations [68].

We can define an output vector $\mathbf{V}_{\rm OUT} = (\tilde{a}, \tilde{a}^\dagger, \tilde{b}_X, \tilde{b}_X^\dagger, \tilde{b}_Y, \tilde{b}_Y^\dagger)$ that is linked to the input noise vector by the equation $\mathbf{V}_{\rm OUT} = \mathbf{O}\,\mathbf{V}_{\rm IN}$ where the final output matrix is

$$\mathbf{O} = \begin{pmatrix} \sqrt{\kappa} & 0 & 0 & 0 & 0 & 0 \\ 0 & \sqrt{\kappa} & 0 & 0 & 0 & 0 \\ 0 & 0 & 1 & 0 & 0 & 0 \\ 0 & 0 & 0 & 1 & 0 & 0 \\ 0 & 0 & 0 & 0 & 1 & 0 \\ 0 & 0 & 0 & 0 & 0 & 1 \end{pmatrix} (-i\Omega\,\mathbf{I} + \mathbf{D})^{-1} - \begin{pmatrix} 1/\sqrt{\kappa} & 0 & 0 & 0 & 0 & 0 \\ 0 & 1/\sqrt{\kappa} & 0 & 0 & 0 & 0 \\ 0 & 0 & 0 & 0 & 0 & 0 \\ 0 & 0 & 0 & 0 & 0 & 0 \\ 0 & 0 & 0 & 0 & 0 & 0 \\ 0 & 0 & 0 & 0 & 0 & 0 \end{pmatrix}.$$

The output spectra are calculated by taking just the coefficients of the few non-null terms in the input noise correlation functions. By calling $O^{\pm}[i,j]$ the (i,j) element of $\mathbf{O}(\pm\Omega)$, a generic output spectrum can be written in the form

$$\begin{aligned} S_{i,j} \;&=\; \kappa\, O^-[i,1]O^+[j,2] \\ &+\; \Gamma_X\left(O^-[i,3]O^+[j,4] + O^-[i,4]O^+[j,3]\right) \\ &+\; \Gamma_Y\left(O^-[i,5]O^+[j,6] + O^-[i,6]O^+[j,5]\right). \end{aligned}$$

For the output field we obtain

$$\begin{aligned} S_{aa} &= \frac{1}{2\pi}\langle\tilde{a}^\dagger(-\Omega)\tilde{a}(\Omega)\rangle \equiv S_{2,1} \\ S_{a^\dagger a^\dagger} &\equiv S_{1,2} \end{aligned}$$

and the heterodyne spectrum, normalized to shot noise, is

$$S_{\text{out}} = \Big(S_{aa}(\Omega-\Omega_{\text{LO}}) + S_{a^\dagger a^\dagger}(\Omega+\Omega_{\text{LO}})\Big)\eta + (1-\eta) \tag{5.7}$$

where Ω_{LO} is the angular frequency of the local oscillator, and η is the detection efficiency.

5.3.1 Strong coupling regime for the 2D motion

The essential information on the system dynamical behavior is encoded in the eigenvalues and eigenvectors of the drift matrix. The formers are three couples of complex conjugate parameters, where the absolute values of the imaginary parts give the three eigenfrequencies, and the corresponding real parts gives the widths of the resonances.

As anticipated in equations (2.12), for weak coupling ($g_X, g_Y \ll \kappa/4$) and well separated mechanical frequencies ($|\Omega_X - \Omega_Y| \gg 4g^2_{\text{X,Y}}/\kappa$) the optical eigenvalues are $\sim \kappa/2 \pm i\Delta$ and the mechanical resonances are given approximately by [3]

$$\Omega_{\text{eff}} \simeq \Omega^0 + g^2\left(\frac{\Delta-\Omega^0}{(\Delta-\Omega^0)^2+\kappa^2/4} + \frac{\Delta+\Omega^0}{(\Delta+\Omega^0)^2+\kappa^2/4}\right) \tag{5.8}$$

$$\Gamma_{\text{eff}} \simeq \gamma + g^2\left(\frac{\kappa}{(\Delta+\Omega^0)^2+\kappa^2/4} - \frac{\kappa}{(\Delta-\Omega^0)^2+\kappa^2/4}\right) \tag{5.9}$$

where we have omitted the subscripts X,Y (Fig.(25a)).

When the optical spring effect is strong enough, and the two natural mechanical frequencies close enough, that the effective frequencies of the two oscillators get closer than their effective widths, the two mechanical modes hybridize, and two linear combinations exhibit the highest and lowest coupling to the optical field. They are, respectively, the geometrical bright and dark mode: $b_{\text{bright}} \propto g_Y\hat{b}_X + g_X\hat{b}_Y$ and $b_{\text{dark}} \propto g_X\hat{b}_Y - g_Y\hat{b}_X$ [20, 39, 59, 68, 69]. Such modes are not exact eigenvectors of the systems, therefore the dark mode resonance is broadened by the coupling with the bright mode (and actually with the optical field), however

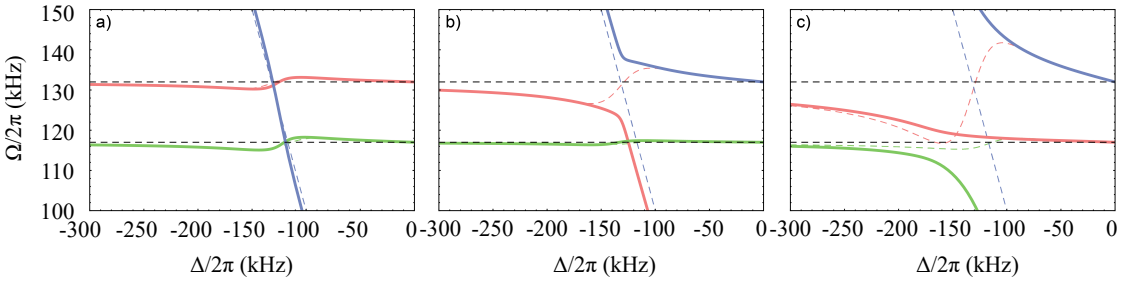

Figure 25: Solid lines: eigenfrequencies derived from the imaginary part of the eigenvalues of the drift matrix, as a function of the detuning. Colored dashed lines: effective frequencies calculated in the weak coupling approximation (Eq.(5.8)). Black dashed lines: mechanical frequencies of the uncoupled oscillators. Common parameters are $\kappa/2\pi = 57$ kHz, $\Gamma_m/2\pi = 0.1$ Hz, $\Omega_X/2\pi = 132$ kHz, $\Omega_Y/2\pi = 117$ kHz. The optomechanical coupling rates are $g_X = g_Y = 2\pi\times 9$ kHz (a), $g_X = 2\pi\times 16$ kHz; $g_Y = 2\pi \times 5$ kHz (b), $g_X = 2\pi \times 29$ kHz; $g_Y = 2\pi \times 9$ kHz (c).

a narrow resonance remains the signature of the hybridization. A drawback of the hybridization is that the optical cooling of the bright mode is hindered by its coupling to the hot, dark mode, therefore reaching the quantum regime is more difficult [20, 68, 69]. On the other hand, hybridization allows the transfer of energy and information between the two mechanical modes, as well as two dimensional cooling.

If the two mechanical frequencies are well separated, when one mode has a coupling strength $g > \kappa/4$ it enters the strong optomechanical coupling regime [3, 8], characterized by an avoided crossing between the eigenfrequencies of the optical mode (that significantly departs from Δ) and of the mechanical mode (Fig.(25b)). The width of the latter does not increase as much as predicted by Eq.(5.9), and it is upper limited to $\kappa/2$. Like the mechanical hybridization, also this effect hinders the attainment of the mechanical quantum regime, even if a phononic occupation number below unity has been achieved even in the strong coupling regime in ultra-cryogenic experiments with a microwave coupled to an aluminum drum oscillator [76, 49].

Finally, in the strong coupling regime involving both mechanical modes, full development of the system into vectorial polaritons occurs (Fig.(25c)). The threshold to reach two-dimensional strong coupling, marked by a double avoided crossing in the spectral curves, is lowered with respect to the single-mode case. It depends on the difference between the resonance frequencies of the uncoupled mechanical modes, approaching $g_X^2 + g_Y^2 > \kappa^2/16$ for $\Omega_X \simeq \Omega_Y$.

5.4 Data analysis

The output signal of the heterodyne balanced detection is low-pass filtered at 1.9 MHz and sampled at 5 MS/s. Spectra are typically obtained with a resolution of 40 Hz, by segmenting the time series into 25 ms long intervals and calculating the Fourier transform. Before averaging, we apply a post-selection of the intervals, keeping those exhibiting the lowest amplitude of the beat note at 1.1 MHz between the scattered light and the local oscillator, i.e., the signals acquired with the nanosphere closer to the node of the cavity mode. This selection allows to reduce the effect of frequency noise in the spectra. In appendix D is reported the Mathematica script with the full theoretical model as well as the fitting procedure by means of Eq.(5.7).

5.5 Evidence of hybrid optomechanical states

In Fig.(26) we show the spectra (high frequency sideband) of the transmitted field when the pressure in the experimental chamber is about 6×10^{-3} Pa, for varying detuning Δ of the tweezer light with respect to the cavity resonance. The photonic component becomes evident for $-\Delta/2\pi = 160$ kHz, where the spectrum shows three peaks for the optical and the two mechanical resonances. The X and Y mode peaks merge, forming the dark and bright modes and, at slightly smaller detuning, the bright mode strongly mixes with the photon field, forming hybrid modes that, in a quantum formalism, are identified as polaritons (we will use in the following this description even if the quantum coherent coupling is just reached at lower pressure). At $-\Delta/2\pi \simeq 140$ kHz we clearly distinguish the photon-like polariton (on the high frequency side of the dark mode peak), and the phonon-like polariton (on the opposite side). For $-\Delta/2\pi \simeq 120$ kHz both polaritons are almost equally composed of phononic and photonic components and, as we will see, the minimum occupation number is achieved. The corresponding resonances have width $\sim \kappa/2$ and are separated by $\sim 2g$. Between them we see the narrow resonance originated by the dark mode. For smaller detuning, the relative position of the photon-like and phonon-like polariton peaks are swapped.

The corresponding spectral curves are reported in Fig.(27). The polaritonic branches are separated by an energy gap, originated by an upper and a lower avoided-crossing, and asymptotically approach the correspondent free mechanical frequencies. This situation is strongly reminiscent of phonon-polaritons in ionic crystals, where the asymptotic frequencies are those of the longitudinal and transverse optical phonons [27]. Inside the gap the curve of the dark mode takes place,

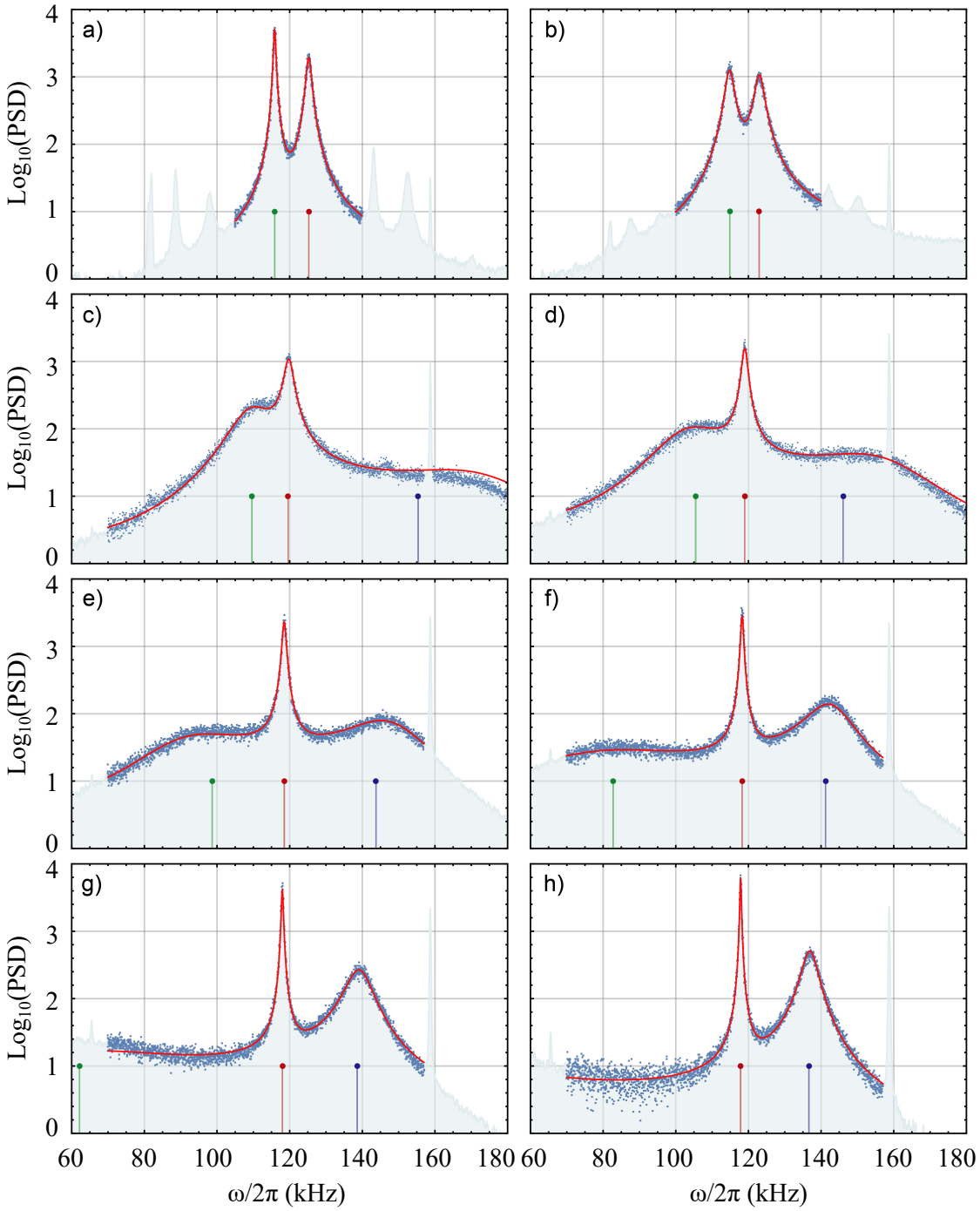

Figure 26: High frequency sideband of the heterodyne spectra, for a background pressure of $\sim 6 \times 10^{-3}$ Pa. The detuning of the tweezer light from the cavity resonance is $-\Delta/2\pi = 260$ kHz (a), 210 kHz (b), 160 kHz (c), 140 kHz (d), 120 kHz (e), 100 kHz (f), 80 kHz (g), 60 kHz (h). Red solid lines show the theoretical spectra, calculated with the following, independently measured, parameters: $\kappa/2\pi = 57$ kHz, $\eta = 0.32$. The mechanical frequencies and optomechanical coupling rates are slightly adjusted for each spectrum, to account for slow variations of the mean nanosphere position and tweezer light power and polarization. Their mean values (standard deviations) are $\Omega_X/2\pi = 131.6\,(0.9)$ kHz, $\Omega_Y/2\pi = 117.3\,(0.2)$ kHz, $g_X/2\pi = 26.7\,(0.3)$ kHz, $g_Y/2\pi = 9.4\,(0.5)$ kHz.

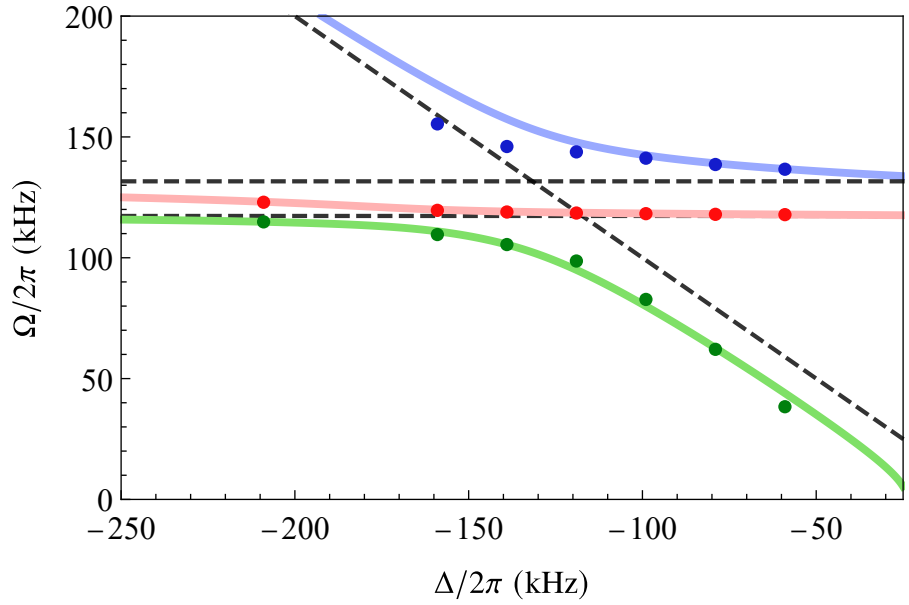

Figure 27: Dispersion curves obtained, as a function of Δ, from the imaginary part of the eigenvalues of the drift matrix (solid lines). The experimental heterodyne spectra do not provide a direct access to such eigenvalues, however the spectral shape can be approximated as a sum of three Lorentzian functions multiplied by the cavity susceptibility, whose centers, obtained from a fit, are shown with dots in the figure (26). Dashed lines show the eigenfrequencies of the uncoupled system (i.e., with $g_X = g_Y = 0$).

similarly to what is observed in the spectra of two-qubit states interacting with microwave photons [60, 1].

The optomechanical coupling rates for the oscillations parallel (Y direction) and perpendicular (X direction) to the tweezer polarization are $g_X/2\pi = 28.5\,\mathrm{kHz}$ and $g_Y/2\pi = 9\,\mathrm{kHz}$.

The phonon occupation numbers for the X and Y mechanical modes are calculated from the integral of the respective displacement spectra, produced by the model. The minimal values are achieved for a detuning of 120 kHz and are respectively around 200 and 1500. We notice that single-mode occupation numbers do not fully describe the thermal state of the system, that requires instead the complete correlation matrix.

5.6 Measurement of the dipole heating rate anisotropy

After the observation of the hybrid optomechanical states in the classical regime, the vacuum chamber is evacuated to high vacuum to decouple the mechanical motion from the thermal environment. It is essential here the characterization of the noise sources acting on the particle to check that no technical excess noise is heating the mechanical motion, thus limiting the cooling results. The force noise that determines the motion of the nanosphere can be ascribed to two fundamental sources, besides the optomechanical coupling: the collisions with the molecules of background gas, and the recoil due to the shot-noise in the dipole emission of the nanosphere. At very low pressures, the contribution of dipole scattering becomes important.

Jain *et al.* [29] have observed the re-heating of the Y mode, after parametric feedback cooling down to a phononic occupation number of ~ 60 in high vacuum. Their measured rate agrees with the theory within $10 - 30\%$.

We can deduce the total decoherence rates for the X and Y motion from the spectrum of the field transmitted by the cavity. These rates mainly determine the area of the spectral peaks generated by the motion of the nanosphere, while their width is dominated by the optical cooling. We have acquired the time series of the heterodyne detection signal during the evacuation of the experimental chamber, maintaining a relatively large detuning of the tweezer radiation from cavity resonance (namely, $\Delta/2\pi = -220\,\mathrm{kHz}$). An example of a derived spectrum (anti-Stokes motional sideband) is shown in Fig.(28a). The spectra are calculated by Fourier transforming consecutive time intervals, and are fitted to the theoretical model of Eq.(5.7). For each spectrum the resonance frequencies Ω_X and Ω_Y, the

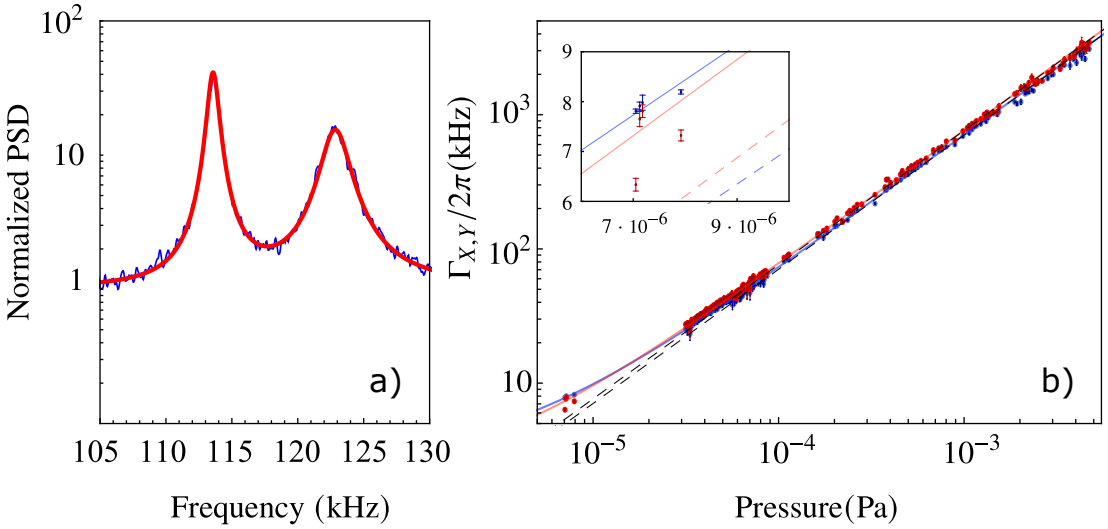

Figure 28: (a) Typical heterodyne spectrum (anti-Stokes sideband, power spectral density PSD normalized to shot noise) showing the resonances of the X and Y modes, acquired at the pressure of $P \simeq 3 \times 10^{-5}$ Pa for a detuning of $-\Delta/2\pi = 220$ kHz. The red solid line is the fit with the theoretical model. (b) Total decoherence rates for the X and Y motion (blue and red dots respectively), measured for a tweezer light detuning of $-\Delta/2\pi = 220$ kHz as a function of background pressure. The error bars represent the standard error, calculated on several consecutive time intervals. The solid lines show linear fits and the dashed lines have the slopes extracted from the fits, but null constant terms. The inset is an enlarged view of the region at lowest pressure.

optomechanical coupling rates g_X and g_Y, and the decoherence rates Γ_X and Γ_Y are derived from the fits, while the detuning Δ, the cavity width κ and the detection efficiency η are measured independently and kept as fixed parameters in the fitting procedure.

The decoherence rates vs pressure can be fitted by a straight line, according to $\Gamma_j/2\pi = a_j + b_j P$ (Fig.(28b)). The parameters derived from this fitting procedure are slopes $b_x = (7.05 \pm 0.02) \times 10^8$ Hz/Pa and $b_y = (7.64 \pm 0.03) \times 10^8$ Hz/Pa, and constant terms $a_x = 2.79 \pm 0.06$ kHz and $a_y = 1.97 \pm 0.15$ kHz. In these expressions, the quoted errors represent the statistical uncertainty of the fits (one standard deviation). However, the main error is due to the evaluation of the detection efficiency, measured to be $\eta = 0.295 \pm 0.03$, which produces an additional uncertainty of 10% in the a_j and b_j parameters.

We have calculated the gas damping rate from the slopes of Γ_j, according to $\gamma_j = P\, b_j \frac{\hbar\Omega_j}{k_B T}$ (see Eq.(5.4)), obtaining $\gamma/2\pi P = 14.4$ Hz/Pa for the X mode, and

14.0 Hz/Pa for the Y mode, in good relative agreement. With the parameters of our nanosphere in nitrogen atmosphere, the theoretical value given by the expression (2.9) is $\gamma/2\pi P = 9.7\,\mathrm{Hz/Pa}$. Even considering the 30% nominal accuracy of the pressure gauge quoted by its manufacturer, the agreement is not very good. This discrepancy can be explained by the heating of the sphere caused by laser absorption, which eventually warms up the background gas, as pointed out in Ref. [42] and analysed in Ref. [25].

The decoherence rates due to the photon recoil in the dipole radiation, calculated for our nanosphere using expression (2.10), are $\Gamma^x_{\mathrm{dip}}/2\pi = 3.0\,\mathrm{kHz}$ and $\Gamma^y_{\mathrm{dip}}/2\pi = 1.7\,\mathrm{kHz}$, with a 20% uncertainty derived from the knowledge of the nanosphere mass and of the tweezer intensity. The agreement with the fitted constant terms $a_{x,y}$ is excellent, indicating that no significant extra noise is present, i.e., the $\Gamma_{\mathrm{n}j}$ introduced in Eq.(5.4) coincide with the Γ^j_{dip}. The calculated fluctuations due to the laser intensity and frequency noise are indeed negligible [51], and the measured decoherence rate shows that even parametric heating due to mechanical vibrations, whose relevance was pointed out in other works [75, 22], do not play an evident role in our case. We also remark that we can distinguish the dipole scattering rates in the two modes, whose ratio (weakly dependent on the detection efficiency) we found to be $a_x/a_y = 1.42 \pm 0.14$. To our knowledge, this is the first time that such spatial variation of the shot noise in the photon recoil due to dipole scattering is shown in the motion of a mesoscopic object. The residual discrepancy with the calculated ratio of 1.8 can be attributed to the imperfectly linear polarization of the light at the output of the optical fiber.

From the measured optomechanical gains of the two modes, we derive a maximum gain $g_{\max}/2\pi = 25.7 \pm 1.7\,\mathrm{kHz}$, and an angle θ that varies between 78° and 69° during the chamber evacuation.

5.7 Vectorial polaritons

In high vacuum, the pressure-independent decoherence terms become relevant, in particular the shot-noise in the dipole scattering [29]. In Fig.(29a,b) are reported the Stokes and anti-Stokes motional sidebands of the heterodyne signal for a particle at the pressure $P = 4.4 \times 10^{-6}\,\mathrm{Pa}$. Here, as demonstrated in the simulation of Fig.(29c), the particle is well above the 2D strong coupling threshold. At this point, the optomechanical coupling rates $g_X/2\pi = 20.5$ kHz and $g_Y/2\pi = 9.3$ kHz well exceed the total decoherence rate $\Gamma_{X,Y}/2\pi \simeq 5$ kHz, in spite of the room-temperature operation.

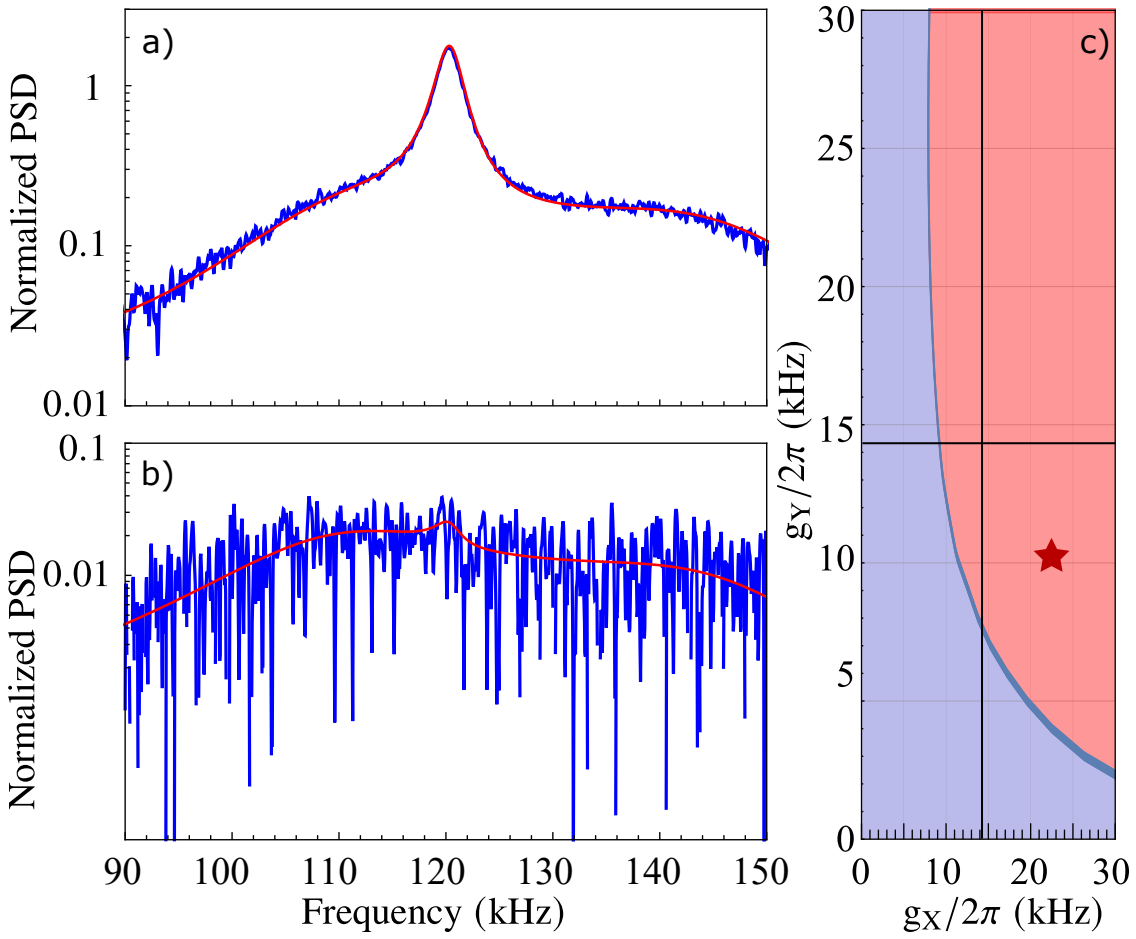

Figure 29: Anti-Stokes a) and Stokes b) motional sideband of the heterodyne power spectral density for the optomechanical system in the quantum coherent regime for a tweezer light detuning of $-\Delta/2\pi = 130\,\mathrm{kHz}$, at a background pressure of $P = 4.4 \times 10^{-6}\,\mathrm{Pa}$. The spectra are normalized to the shot noise, that was then subtracted. The red solid line is the fit with the theoretical model. The inferred values of the optomechanical coupling factors are $g_X/2\pi = 20.5$ kHz and $g_Y/2\pi = 9.5$ kHz and the mechanical frequencies are $\Omega_X/2\pi = 131$ kHz, $\Omega_Y/2\pi = 118$ kHz. Panel c): Optomechanical coupling rate threshold to achieve the two-dimensional strong coupling regime. The blue solid line, calculated for $\kappa/2\pi = 57$ kHz, $\gamma/2\pi = 0.1$ Hz, $\Omega_X/2\pi = 131$ kHz, $\Omega_Y/2\pi = 118$ kHz, is obtained by a numerical study of the eigenvalues of the drift matrix. Double avoided crossing is observed above this line (in the light red region). Black solid lines show the threshold for a system with a single mechanical mode (i.e., $g_{X,Y} > \kappa/4$). The red star corresponds to the particle analysed in this section.

The system has fully entered the quantum coherent strong-coupling regime. As such, the broad peaks on the two sides of the spectra are associated to the polaritonic modes. The phonon-like and photon-like components in each Polariton have similar strengths. The sharper peak in the middle is associated to the geometrical dark mode that couples to the geometrical bright mode because of the non-degeneracy of the two mechanical oscillators.

5.8 How far from the quantum ground state?

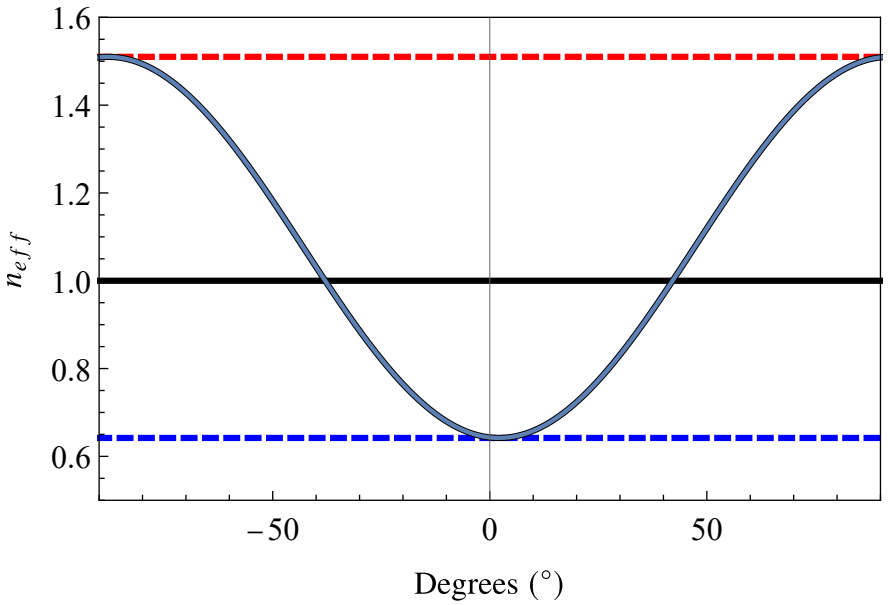

Figure 30: Effective occupancy as a function of the angle between the motional direction and the cavity axis evaluated by means of Eq.(5.10) for the spectrum reported in sec. 5.11, where $g_X/2\pi = 14$ kHz, $g_Y/2\pi = 11$ kHz and the mechanical frequencies are $\Omega_X/2\pi = 131$ kHz, $\Omega_Y/2\pi = 120$ kHz, with $\Gamma_X = 2\pi$ 5.7 kHz and $\Gamma_Y = 2\pi$ 5.4 kHz.

Here is discussed the definition of occupancy for the mechanical motion. Let's start with an oscillator linearly and weakly coupled to the cavity field. The external noisy bath, with the thermal (gas collisions) and optical (dipole scattering and cavity noise) components, drives transitions between the energy levels of the

oscillator at a rate[13]

$$\Gamma_{n\to n+1} = (n+1)\,\Gamma_{\uparrow},$$
$$\Gamma_{n\to n-1} = n\Gamma_{\downarrow},$$

where $\Gamma_{\uparrow} \sim S_{FF}(-\Omega)$ and $\Gamma_{\downarrow} \sim S_{FF}(\Omega)$ with S_{FF} the PSD of the overall noise force acting on the oscillator of frequency Ω.

The time evolution of the occupancy probability for a Fock state is:

$$\dot{p}_n(t) = [n\Gamma_{\uparrow}p_{n-1} + (n+1)\,\Gamma_{\downarrow}p_{n+1}] - [n\Gamma_{\downarrow} + (n+1)\,\Gamma_{\uparrow}]\,p_n.$$

The stationary state of the oscillator, that is obtained setting $\dot{p}_n(t) = 0\,\forall n$, is described by the Bose-Einstein probability coefficients:

$$p_n = e^{-n\hbar\Omega/k_{\mathrm{B}}T}\left(1 - e^{-\hbar\Omega/k_BT}\right),$$

where T is the bath effective temperature at the oscillator frequency Ω ($k_{\mathrm{B}}T \equiv \hbar\Omega/\log\left[S_{FF}(\Omega)/S_{FF}(-\Omega)\right]$). So, the oscillator is in a thermal state:

$$\psi = \frac{1}{1+\bar{n}}\sum_{k=0}^{\infty}\left(\frac{\bar{n}}{1+\bar{n}}\right)^k |k\rangle\langle k|,$$

where $\bar{n}$ is the mean occupancy and the sum is over all the Fock states.

The point here is that the energy of the thermal state is fully characterized via the mean occupancy.

According to the standard definition of optomechanics the oscillator reaches the ground state when $\bar{n} < 1$. This means that is more probable to find the oscillator in the vacuum Fock state than in any other ($k \geq 1$).

What about our system? Without coupling with the cavity field, the 2D motion of the nanosphere in the plane perpendicular to the tweezer axis is well described by two harmonic oscillators along orthogonal directions (X and Y) defined by the tweezer polarization. In any other direction of the plane, the motion is given by a weighted sum of the two oscillations, with a spectrum displaying two peaks, and it cannot be simply reproduced by a single harmonic oscillator. Introducing the strong coupling with the cavity field, the system is generally described by three harmonic oscillators associated to the hybridized modes (vectorial polaritons [51]), defined by the eigenvectors of the drift matrix. Therefore, in this case, in no direction can the motion be simply associated to a single harmonic oscillator. We can

characterize the state of the polaritons by their bosonic occupation number, but we cannot straightforwardly assign a phononic occupation number to the motion in any direction. We note in particular that, in the presence of several resonance peaks in the displacement spectrum, the energy equipartition is not preserved, i.e., $m^2\Omega_0^2 \langle x^2 \rangle \neq \langle p^2 \rangle$ for any physically meaningful choice of Ω_0 (here, x and p are the position and momentum along the considered direction).

The motion of the nanosphere can be meaningfully and uniquely characterized by specifying how far it is from a minimum uncertainty state, i.e., by quantifying the parameter $\frac{4}{\hbar^2}\langle x^2 \rangle \langle p^2 \rangle$. For a quantum mechanical oscillator in a thermal state, this parameter coincides with $(2\bar{n}+1)^2$, where $\bar{n}$ is the mean phononic occupation number. It is therefore natural to define an effective thermal occupancy for the motion along the generic ϕ direction, as

$$n_{\text{eff}}(\phi) = \frac{1}{2}\left(\frac{2}{\hbar}\sqrt{\langle x_\phi^2 \rangle \langle p_\phi^2 \rangle} - 1\right) \tag{5.10}$$

where $x_\phi = x \sin\phi + y \cos\phi$, $p_\phi = p_x \sin\phi + p_y \cos\phi$, and x, y, p_x, and p_y are the physical coordinates and momenta along the X and Y direction. These variables are derived from the $\hat{b}_j$ operators used in the model according to the expressions (5.3). The variances can be calculated as integrals of the spectra, according to $\langle \mathcal{O}^2 \rangle = \int S_{\mathcal{O}\mathcal{O}}(\Omega) \frac{\mathrm{d}\Omega}{2\pi}$. An example of the occupancy as a function of the angle referred to the cavity axis is reported in Fig.(30).

5.9 Exploring the 2D quantum motion

Since we've the possibility to rotate the tweezer angle, the next sections report on the investigation of the system properties in the optimal configuration for the 1D and 2D cooling.

The spectra shown in the previous section are acquired for a polarization angle close to 70°, such that the direction of strongest cooling (the geometrical bright mode direction) is close to the direction X defined by the optical trap. On the other hand, the Y direction is close to the geometrical dark mode direction and thus very weakly coupled to the field.

By rotating the polarization angle θ we increase g_Y and enter the regime of true 2D cooling. As shown in Fig.(31), g_Y matches and then overtakes g_X, as expected. In the region where the two gains are similar, we also observe the most efficient 2D cooling, i.e., we achieve for this particle the lowest value of the occupation along the warmest motional direction, which is $n_{\text{eff}}^{\max} = 3.4 \pm 0.4$.

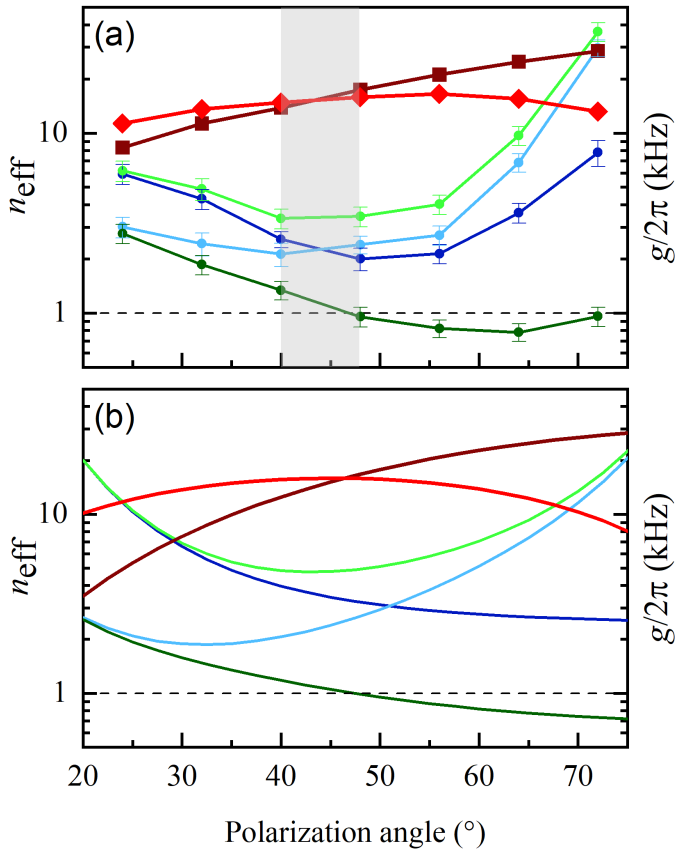

Figure 31: (a) Effective thermal occupancy along the coldest (dark green), warmest (light green), X (dark blue) and Y (light blue) direction of oscillation for a tweezer light detuning of $-\Delta/2\pi = 130\,\mathrm{kHz}$, at varying tweezer polarization angle. Square, dark red (diamond, light red) symbols: optomechanical coupling coefficient for the X (Y) motion. Solid lines are guides for the eye. In the abscissa, we report the polarization angle at the input of the tweezer fiber. The shadowed region highlights the achievement of the strongest 2D confinement. (b) Expected trend of the same parameters, plotted as a function of the tweezer polarization angle θ, assuming linear polarization. These theoretical curves are computed using the following values of the system parameters: $-\Delta/2\pi = 130$ kHz, $\Omega_X/2\pi = 125$ kHz, $\Omega_Y/2\pi = 114.4$ kHz, $g_{\mathrm{max}}/2\pi = 31\,\mathrm{kHz}$, $\Gamma_X/2\pi = 12.4\,\mathrm{kHz}$, and $\Gamma_Y/2\pi = 12.3\,\mathrm{kHz}$ (the decoherence rates are calculated for a background pressure of $P = 1.4\ 10^{-5}$ Pa). The agreement with the data of the upper panel is good, yet we remark that the comparison can just be qualitative since the propagation in the tweezer optical fiber modifies the light polarization, yielding an increasing ellipticity and a poorly controlled output angle.

At the same time, the smallest effective thermal occupancy is around 1. This result has presented a major improvement with respect to previous experiments, since parametric cooling just allowed to achieve 2D occupation numbers around 100 [29], and strong coherent scattering cooling was previously optimized for the single X direction, while the occupation number of the Y mode was just estimated to be below 100 [15]. Recently [48] the simultaneous ground-state cooling of two mechanical modes of a levitated nanoparticle has been achieved, but in the weak coupling regime.

Finally, for $\theta \sim \pi/2$, the motion along the cavity axis is strongly cooled, thus falling below unity.

5.9.1 Occupancy as a function of the detuning

First of all, to check that no unmodeled detuning-dependant noise is present, several spectra have been acquired for different laser frequencies with $\theta \sim \pi/2$. When tuning the tweezer radiation closer to resonance, the optomechanical interaction is increased, and the 2D motion is better modeled by a bright mechanical mode and a dark mode. The former corresponds to the motion in the direction of the cavity axis X_C (close to X for small θ), the latter is in the orthogonal direction (i.e., along Y_C). The decoherence rates measured at different detunings, at low pressure, remain stable as shown in Fig.(32a), in particular for what concerns their mean value $0.5(\Gamma_X + \Gamma_Y)$. Indeed, when the two mechanical modes are coupled through the cavity field and their spectra are superposed, we can hardly distinguish the contributions of the two decoherence channels from the shape of the heterodyne spectrum, while the spectral area is determined by their overall effect.

It is worth noting that for $\Delta \simeq -\Omega_{X,Y}$ the occupancy along the coldest motional direction is well below unity (see Fig.(32b)), thus achieving the 1D ground state cooling, that will be presented in the next section for a different nanoparticle, for which we had slight improvement thanks to a further decrease of the pressure.

5.9.2 One dimensional ground state cooling in the strong coupling regime

For a detuning $\Delta \simeq -\Omega_{X,Y}$ the optomechanical effect is maximum and the geometrical bright mode is strongly coupled with the optical field, yielding hybridized modes (polaritons) [53, 51]. The lowest occupancy spectrum is shown in Fig.(33)a,b, for the anti-Stokes (upper spectrum) and Stokes (lowe spectrum) sidebands. The two polaritonic peaks are centered at $\sim 100\,\mathrm{kHz}$ and $\sim 142\,\mathrm{kHz}$ (their

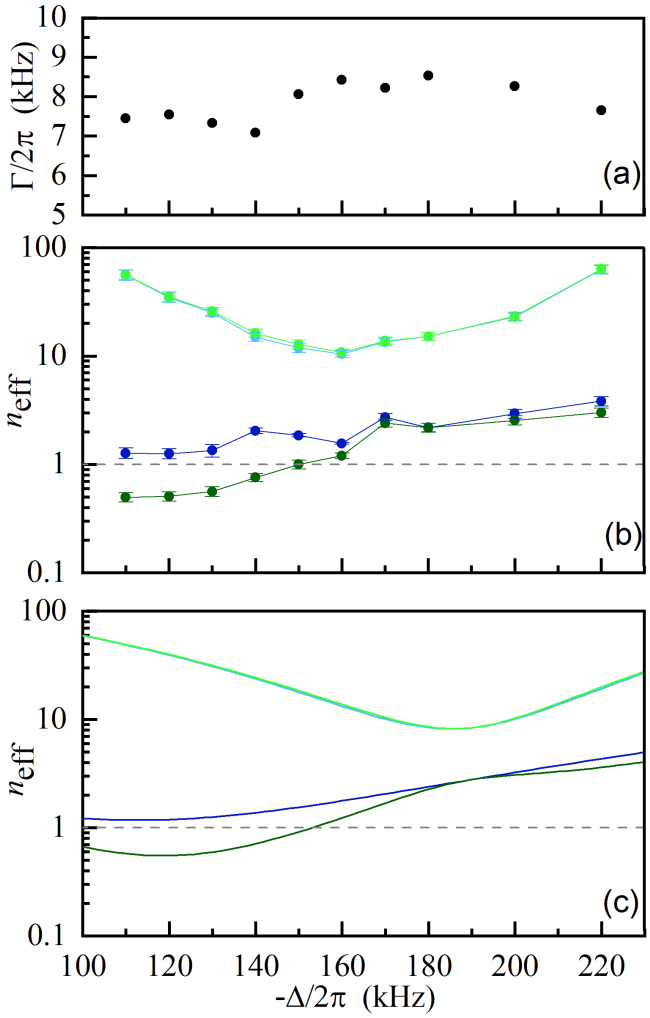

Figure 32: (a) Mean decoherence rate $\Gamma = 0.5\,(\Gamma_X + \Gamma_Y)$ deduced from the experimental spectra at varying detuning. (b) Effective thermal occupancy along the coldest (dark green), warmest (light green), X (dark blue) and Y (light blue) direction of oscillation, as a function of the detuning of the tweezer light from cavity resonance. Solid lines are guides for the eye. (c) Expected trend of the same occupation numbers. These theoretical curves are computed using the following values of the system parameters: $\Omega_X/2\pi = 125.9$ kHz, $\Omega_Y/2\pi = 115.95$ kHz, $g_X/2\pi = 23.5\,$kHz, $g_Y/2\pi = 3.5\,$kHz, $\Gamma_X/2\pi = 7.85\,$kHz, and $\Gamma_Y/2\pi = 7.45\,$kHz (these decoherence rates are calculated for a background pressure of $P = 7.2\ 10^{-6}$ Pa).

frequency splitting is $\sim 2g_X/2\pi$) and are wide (full width) respectively $\sim 34\,$kHz and $\sim 22\,$kHz (i.e., close to $0.5\kappa/2\pi$) as anticipated in Sec.2.3.3. Between the two polaritonic peaks, a third narrow peak is visible, centered at $\sim 119\,$kHz and

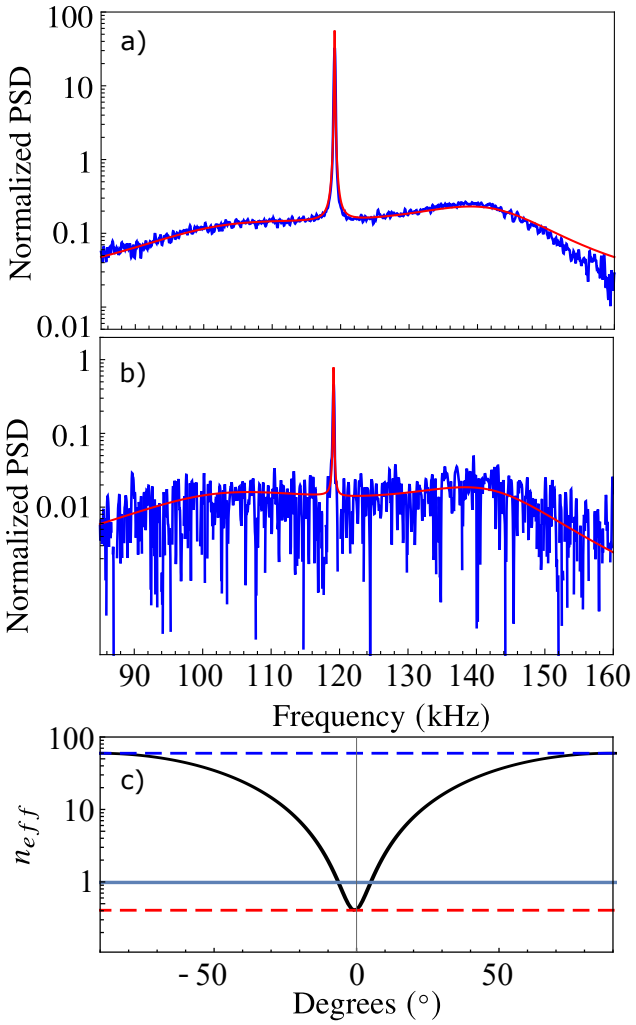

Figure 33: Anti-Stokes a) and Stokes b) motional sideband of the heterodyne power spectral density for the optomechanical system in the quantum coherent regime for a tweezer light detuning of $-\Delta/2\pi = 120\,\text{kHz}$, at a background pressure of $P = 4.8 \times 10^{-6}\,\text{Pa}$. The red solid line is the fit with the theoretical model. The inferred values of the optomechanical coupling factors are $g_X/2\pi = 23.8$ kHz and $g_Y/2\pi = 2.5$ kHz and the mechanical frequencies are $\Omega_X/2\pi = 128$ kHz, $\Omega_Y/2\pi = 119\,\text{kHz}$. Panel c): effective occupancy as a function of the angle between the motional direction and the cavity axis. The occupation in the range $\pm 10°$ around the cavity axis is lower than one, reaching the minimum value of 0.41, calculated by means of Eq.(5.10).

$\sim 40\,\text{Hz}$ wide. It originates from the bright mode's coupling to the dark mode due to unequal frequencies $\Omega_X \neq \Omega_Y$. Here that peak is sharper than the spectrum in

Fig.(29) because of the strong unbalance between the two optomechanical coupling strengths.

In Fig.(33c) is plotted the occupation numbers as a function of the angle referred to the cavity axis. The occupancy along the coldest direction is $\bar{n}_{\mathrm{eff}}^{\mathrm{min}} = 0.41 \pm 0.04$.

5.10 Thermometry? Not so trivial

The radiation scattered by the nanosphere on the cavity mode and transmitted by the cavity output mirror is the only sensitive probe that we have to analyse the motion of the nanosphere. Most optomechanical experiments deal with a single mechanical mode weakly coupled to the probe field, a situation that allows to infer some properties of the motion in a direct way. The signature of the mechanical mode is typically a Lorentzian peak in the field spectrum, whose calibrated area yields the displacement variance and the temperature of the mechanical oscillator, while the asymmetry between the Stokes and anti-Stokes peaks in the motional sidebands is a quantum feature allowing a direct measurement - optomechanical thermometry - of the phononic occupation number [55, 31, 6]. For our configuration of two correlated mechanical oscillators strongly coupled to the cavity field such a direct analysis in not viable.

These features are analysed in the next two sections, where the expected spectral features in the weak coupling regime and the observed asymmetry in the strong coupling regime are presented.

5.10.1 Asymmetry in the weak coupling regime

Let's consider an optomechanical system composed of a mechanical oscillator weakly coupled to the field of a high finesse optical cavity. As stated in Sec. 2.3.3 the oscillator mechanical response to an external force is described by its modified susceptibility. As the oscillator reaches the equilibrium with the external bath, the motional PSD reads:

$$S_{qq}(\omega) \sim \left[\left| \chi_m^{\mathrm{eff}}(\omega) \right|^2 S_{FF}(-\Omega_{eff}) + \left| \chi_m^{\mathrm{eff}}(-\omega) \right|^2 S_{FF}(\Omega_{eff}) \right]. \tag{5.11}$$

It can be shown [57] that $S_{FF}(\Omega_{\mathrm{eff}}) \propto \bar{n} + 1$ and $S_{FF}(-\Omega_{\mathrm{eff}}) \propto \bar{n}$. As such, the mechanical PSD reads

$$S_{qq}(\omega) = q_{\mathrm{zpf}}^2 \gamma_{\mathrm{eff}} \left[\left| \chi_{\mathrm{m}}^{\mathrm{eff}}(\omega) \right|^2 \bar{n} + \left| \chi_{\mathrm{m}}^{\mathrm{eff}}(-\omega) \right|^2 (\bar{n} + 1) \right],$$

where $\bar{n}$ is the mean Bose occupancy at the equilibrium temperature of the bath at the mechanical frequency. Now, since the heterodyne detection gives access directly to the motional spectrum, it is possible to infer the occupancy the oscillator via the sideband asymmetry measurement. This procedure is called Sideband Thermometry. It is noteworthy that such asymmetry is always present, but because of its weak dependence on $\bar{n}$, it's experimentally measurable at low mechanical energies.

As final remark, it is well known that the PSD of a real variable must be symmetric in frequency. As such, the measurement of a non zero asymmetry corresponds to the experimental evidence of a non classical effect of the mechanical motion.

5.10.2 Asymmetry in the strong coupling regime

The bright mode is strongly cooled, eventually entering the quantum regime whose signature, as already discussed, is the spectral asymmetry.

The optical fluctuations imprinted by the mechanical motion along the cavity axis are detected via the heterodyne setup and give access to the geometrical bright mode x_b, i.e. considering Eq.(5.6) :

$$\tilde{a} = (\kappa\chi_{\mathrm{c}} - 1)\,\tilde{a}_{\mathrm{IN}} + i\sqrt{\kappa}\chi_{\mathrm{c}} g_{\mathrm{b}} x_{\mathrm{b}},$$

where $x_{\mathrm{b}} = (g_X x + g_Y y)/g_{\mathrm{b}}$ and $g_{\mathrm{b}} = \sqrt{(g_X^2\Omega_x + g_Y^2\Omega_y)/\Omega_b}$ (see Sec. 2.3.4). So, the PSD of the heterodyne signal around the local oscillator frequency reads [8]:

$$S_{\mathrm{out}}(\Omega_{\mathrm{LO}} + \omega) = 1 + g_{\mathrm{b}}^2\kappa\,|\chi_{\mathrm{c}}(\omega)|^2\, S_{x_{\mathrm{b}}x_{\mathrm{b}}}(\omega)\,.$$

In the radiation transmitted by the cavity, the motional sidebands are filtered by the cavity transmission function (optical susceptibility). To recover a more meaningful indicator, we define a corrected asymmetry as

$$A(\omega) \;=\; \frac{S_{\mathrm{out}}(\Omega_{\mathrm{LO}} - \omega) \;-\; 1}{S_{\mathrm{out}}(\Omega_{\mathrm{LO}} + \omega) \;-\; 1}\;\frac{(\omega - \Delta)^2 + (\kappa/2)^2}{(\omega + \Delta)^2 + (\kappa/2)^2}\,,$$

which equals the asymmetry in the geometrical bright mode spectrum.

The solution of the system reported in 5.1 gives the stationary state of the

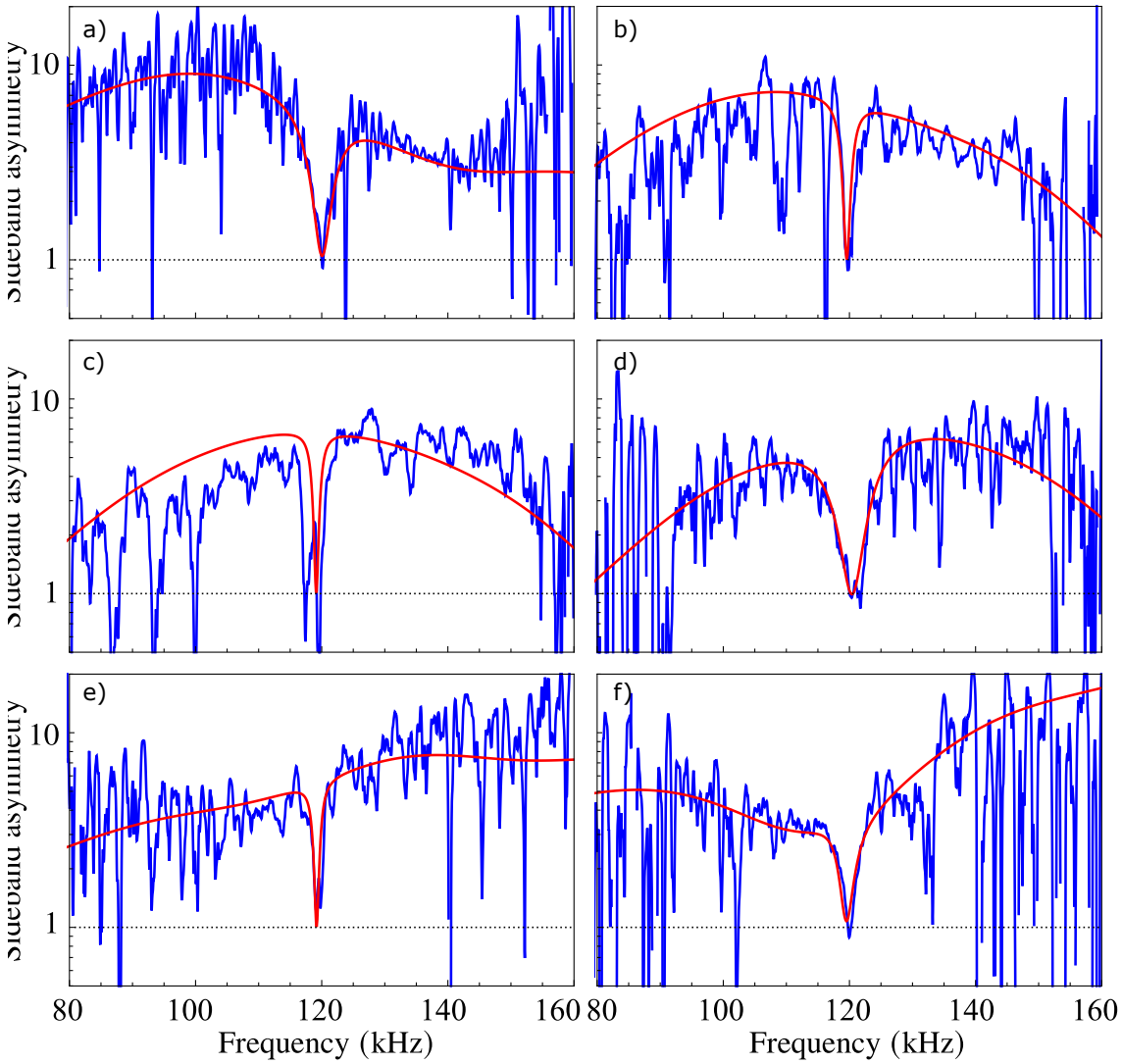

Figure 34: Ratio between Stokes and anti-Stokes sidebands for a tweezer light detuning ranging from $-\Delta/2\pi = 100\,\mathrm{kHz}$ (panel a), to $-\Delta/2\pi = 150\,\mathrm{kHz}$ (panel f) in steps of 10 kHz, at a background pressure of $P = 4 \times 10^{-6}\,\mathrm{Pa}$. The red solid line is the theoretical model obtained from the fit. The inferred mean values of the optomechanical coupling factors are $g_X/2\pi = 22$ kHz and $g_Y/2\pi = 4.5$ kHz, hence the system can be described by an oscillator in the strong optomechanical coupling regime, plus a second weakly coupled oscillator.

geometrical Bright mode. The analytical formulation of the PSD reads:

$$S_{x_\mathrm{b}x_\mathrm{b}} = \frac{\Omega_\mathrm{b}}{g_X^2\Omega_X + g_Y^2\Omega_Y} \frac{1}{\left|1 + \chi_\mathrm{c}^- \left(g_X^2\chi_x^- + g_Y^2\chi_y^-\right)\right|^2} \cdot \left[g_X^2\Gamma_X\left(|\chi_x(\omega)|^2 + |\chi_x(-\omega)|^2\right) + g_Y^2\Gamma_Y\left(|\chi_y(\omega)|^2 + |\chi_y(-\omega)|^2\right) + \left|g_X^2\chi_x^- + g_Y^2\chi_y^-\right|^2 \kappa\,|\chi_\mathrm{c}(-\omega)|^2\right], \quad (5.12)$$

where $\chi_{\rm c}^{-} = \chi_{\rm c}(\omega) - \chi_{\rm c}^{*}(-\omega)$, $\chi_{x(y)}^{-} = \chi_{x(y)}(\omega) - \chi_{x(y)}^{*}(-\omega)$ and $\chi_{x(y)}$ is the mechanical susceptibility as defined in 2.2. The sideband asymmetry features can be understood in terms of this analytic solution.

First of all, we can distinguish the contribution of the spectrally flat noise forces (thermal and dipole scattering) acting on the oscillator, proportional to $\Gamma_{X,Y}$, from that associated to the white optical vacuum noise, filtered by the cavity, which is proportional to $\kappa\left|\chi_{\rm c}(-\omega)\right|^2$.

For the interpretation of this model, it is instructive to start from its 1-D limit:

$$S_{xx} \sim \frac{1}{\left|1+g^2\chi_{\rm c}^{-}\chi_{\rm m}^{-}\right|^2}\cdot\left[g^2\Gamma\left(\left|\chi_{\rm m}(\omega)\right|^2+\left|\chi_{\rm m}(-\omega)\right|^2\right)+\left|\sqrt{\kappa}g^2\chi_{\rm m}^{-}\chi_{\rm c}(-\omega)\right|^2\right]$$

where, for the seek of clarity, $x_{\rm c}\to x$, Γ is the mechanical decoherence rate and $\chi_{\rm m}$ is the mechanical susceptibility. Here, the term

$$\frac{\left|\chi_{\rm m}(\omega)\right|^2+\left|\chi_{\rm m}(-\omega)\right|^2}{\left|1+g^2\chi_{c}^{-}\chi_{\rm m}^{-}\right|^2}=\left|\chi_{\rm m}^{eff}\right|^2$$

is the squared modulus of the optomechanical effective susceptibility (see Sec. 2.3.3) written in its compact form.

In the weak coupling regime ($g\ll\kappa/4$), $\chi_{\rm m}^{eff}$ is a sharp peak as compared to the broad cavity resonance and the oscillator probes the noisy bath close to its resonance frequency:

$$S_{xx}(\pm\omega)\propto\left|\chi_{\rm m}^{\rm eff}(\pm\omega)\right|^2\left(\Gamma+g^2\kappa\left|\chi_{\rm c}(\mp\Omega_{\rm eff})\right|^2\right).$$

This equation is analogous to Eq.(5.11), but with the noise force terms explicitly expressed. We clearly see that a strong asymmetry is achieved when the flat noise term goes to zero ($\Gamma\to 0$) and the optical vacuum noise imprints the cavity shape onto the mechanical sidebands, which in turn define the mechanical occupancy [13, 8]

$$\frac{\bar{n}+1}{\bar{n}}=\left|\frac{\chi_{\rm c}(\Omega_{\rm eff})}{\chi_{\rm c}(-\Omega_{\rm eff})}\right|^2.$$

It should be clearly stated that the oscillator actually probes the coloured noise at all the frequencies, but it is sensitive to it only close to the mechanical resonance.

In the strong coupling regime, on the other hand, the mechanical modified susceptibility gets broader and is composed of the two polaritonic peaks of width

$\sim \kappa/2$ (see Sec.2.3.3). Here, the mechanical transfer function probes the noisy bath on a bandwidth of the order of $\sim 2g + \kappa/2 > \kappa$ around the mechanical bare frequency on both the positive and negative frequency axes.

In this case, the sideband-asymmetry frequency dependence can be experimentally probed over a wide range and reads (in the limit of $\Gamma \to 0$):

$$\frac{S_{xx}(-\omega)}{S_{xx}(\omega)} = \left| \frac{\chi_{\mathrm{c}}(\omega)}{\chi_{\mathrm{c}}(-\omega)} \right|^2 \tag{5.13}$$

and reaches its maximum around the detuning value.

Now let's go back to the general 2-D case. At low pressure the asymmetry is still defined by the shape of the optical cavity, as in Eq.(5.13) but with the addiction of a peculiarity that comes out from the presence of the two mechanical susceptibilities. Qualitatively, the mechanical motion of the two oscillators is imprinted in the optical fluctuations. As such, each of the mechanical oscillators reacts to a field whose dynamics is set not only by the cavity susceptibility, but also by the mechanical susceptibility of the other oscillator. In a nutshell, in the frequency range between the two bare mechanical resonances the optical fluctuations induced by the two mechanical oscillators add with a π relative phase, thus interfering destructively. In the region where these two contributions have the same amplitude, the overall optomechanically induced fluctuations cancel out thus inhibiting the optomechanical dynamical interaction.

The physics of this process is encoded in the term:

$$g_Y^2 \chi_y^- + g_X^2 \chi_x^- \tag{5.14}$$

of Eq.(5.12). The two mechanical susceptibilities are weighted each with the corresponding coupling strength.

It can be shown that, in the limit of vanishing thermal damping, this term is null at the geometrical Dark mode frequency Ω_{d} (see Eq.(2.14)), whose value is constrained between Ω_X and Ω_Y. Looking closer to Eq.(5.12), this means that at $\omega = \Omega_{\mathrm{d}}$ the optical cavity noise is dynamically inhibited from entering the mechanical system. On the other hand the two mechanical oscillators are directly coupled to their - uncorrelated - thermal baths via their bare mechanical susceptibilities, thus probing the - spectrally flat - noisy bath.

The measured corrected asymmetry is shown in Fig.(34) for the detuning ranging from $-\Delta/2\pi = 100\,\mathrm{kHz}$ (panel a) to $-\Delta/2\pi = 150\,\mathrm{kHz}$ (panel f) in steps of 10 kHz for the same particle of section 5.9.2. As anticipated, the motional side-

band asymmetry that reveals the quantum nature of the dynamics is not limited to mere scale factors between Stokes and anti-Stokes peaks, as customary in quantum optomechanics.

In excellent agreement with the model, the maximal asymmetry occurs close the spectral frequency matching $\omega \sim -\Delta$, where it ranges between ~ 5 and ~ 9, denoting a strong non-classical behavior. The asymmetry in correspondence of the resonance frequencies of the two polaritonic modes, for example in panel d) for the detuning of 130 kHz, is around 5. In the limit of viewing the polaritons as independent quantum harmonic oscillators, this would correspond to polariton occupation numbers $1/(A-1) = 0.25$, but this information is not sufficient to determine the bright mode's thermal occupancy.

The dip at $\sim 119\,\mathrm{kHz}$, resulting from the inhibition of the optomechanically induced dynamic, falls to 1 because of the mechanical coupling to the flat noise forces in that narrow spectral region.

The theoretical curves, evaluated for an efficiency $\eta = 0.23$, show good agreement with the experimental results thus proving that this parameter is properly estimated. In fact in the classical regime very similar spectra are obtained by increasing the noise and decreasing the detection efficiency, or vice-versa. The situation changes close to the quantum regime, where the spectral asymmetry between the Stokes and anti-Stokes motional sidebands in the electromagnetic field, that is independent from the detection efficiency, gives a further crucial indication on the achieved quantum state. The observation of such spectral asymmetry has the dual purpose of demonstrating the achievement of the quantum regime, and confirming the accuracy of the noise evaluation.

5.11 Strong two-dimensional cooling

An important step forward on the route towards the ambitious goal of realizing three-dimensional ground state cooling is the observation and characterization of the 2D quantum motion on the tweezer transverse plane. An optomechanical system with two nearly-degenerate mechanical modes was already considered in the literature [20, 39, 59]. However, here we deal with 2D motion, where its projections along all the directions (i.e., every linear combination of the two modes that are arbitrarily chosen as reference frame) have a clear physical meaning. This requires addressing the problem in a radically different way from what is customary in optomechanics, both in the description of the system and in the analysis of the experimental signals and of the information that can be extracted. The problem is

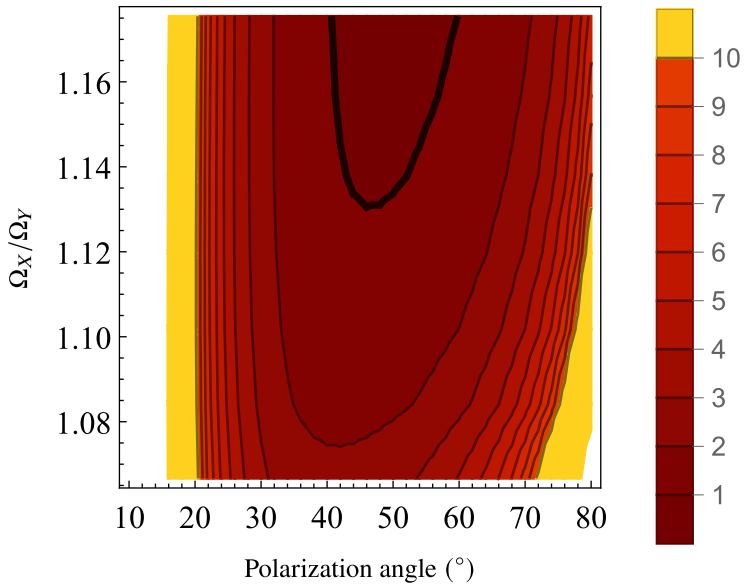

Figure 35: Occupancy as a function of the the mechanical frequencies and the tweezer polarization angle. The simulation is evaluated for typical experimental parameters, with $-\Delta/2\pi = (\Omega_X + \Omega_y)/2(2\pi) = 124$ kHz, $\sqrt{(g_X^2 + g_Y^2)}/2\pi = 25$ kHz, $\kappa/2\pi = 57$kHz and $\Gamma_X = 2\pi$ 5.7 kHz and $\Gamma_Y = 2\pi$ 5.4 kHz. The ground state is achieved as $g_X \sim g_Y$ and the two mechanical frequencies are far enough.

theoretically analysed in [69] where it is shown that for suitable system parameters the particle full planar motion can be strongly coupled to the light and efficiently cooled through coherent scattering. It is observed that the optimal cooling of the 2D motion is achieved when the frequency difference between the two mechanical oscillators is sufficiently large to couple the GDM to the GBM (see Eq.(2.16)) without involving a strong filtering of the cavity.

The simulation of the occupancy along the warmest motional direction is reported in Fig.(35) as a function of the ratio between the two mechanical frequencies (with mean value of 124kHz) and of the tweezer angle for a laser detuning $\Delta/2\pi = -124$kHz and a maximum coupling strength $g_{max}/2\pi = 25$kHz. With realistic experimental parameters the 2D ground state cooling in the Quantum coherent regime is feasible.

In the strongest two dimensional cooling configuration that has been recently achieved in our setup, we have derived an occupancy of 1.5 along the warmest motional direction. In the panels a) and b) of Fig.(36) are reported the Stokes/anti-Stokes sidebands of the heterodyne PSD, while in panel c) is shown the sideband

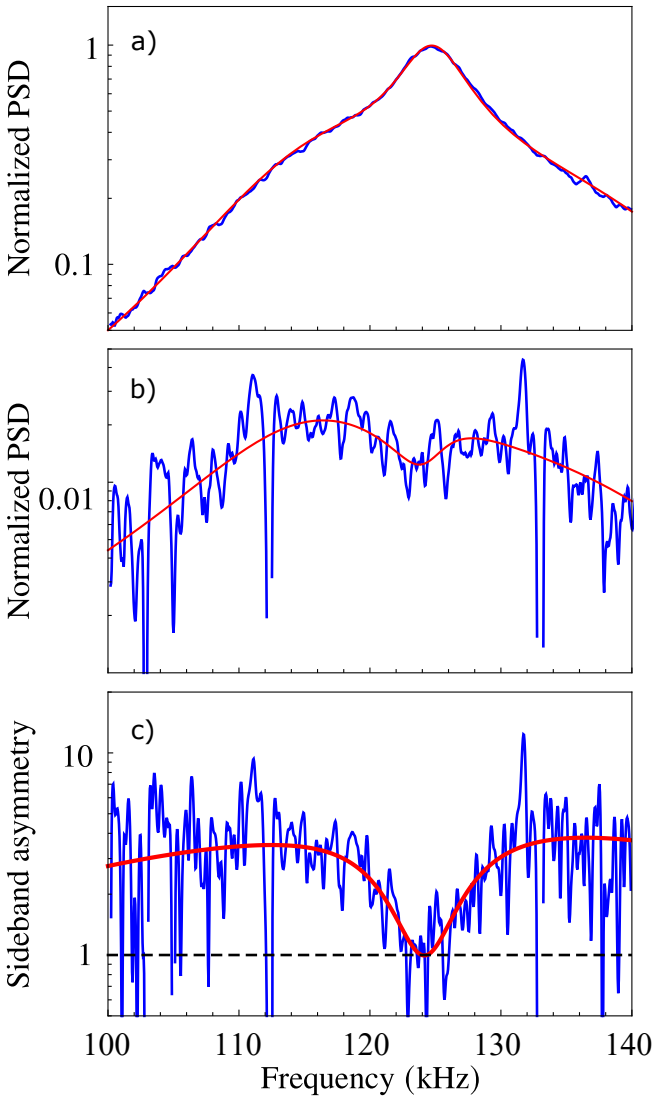

Figure 36: Panels a) and b): heterodyne spectrum (anti-Stokes and Stokes sidebands) normalized to the detection shot noise and with the same shot noise subtracted, for the polarization angle that minimizes the effective thermal occupancy in the whole $X - Y$ plane. Red solid line: fit of the theoretical model. Panel c) asymmetry between the Stokes and anti-Stokes sidebands.

asymmetry.

The measured optomechanical parameters are $g_X/2\pi = 14$ kHz and $g_Y/2\pi = 11$ kHz and the mechanical frequencies are $\Omega_X/2\pi = 131$ kHz, $\Omega_Y/2\pi = 120$ kHz.

The two sidebands have different patterns, with the Stokes band that shows a dip in the region of the dark mode. According to Eq.(5.12) for $\omega < \Omega_Y$ and

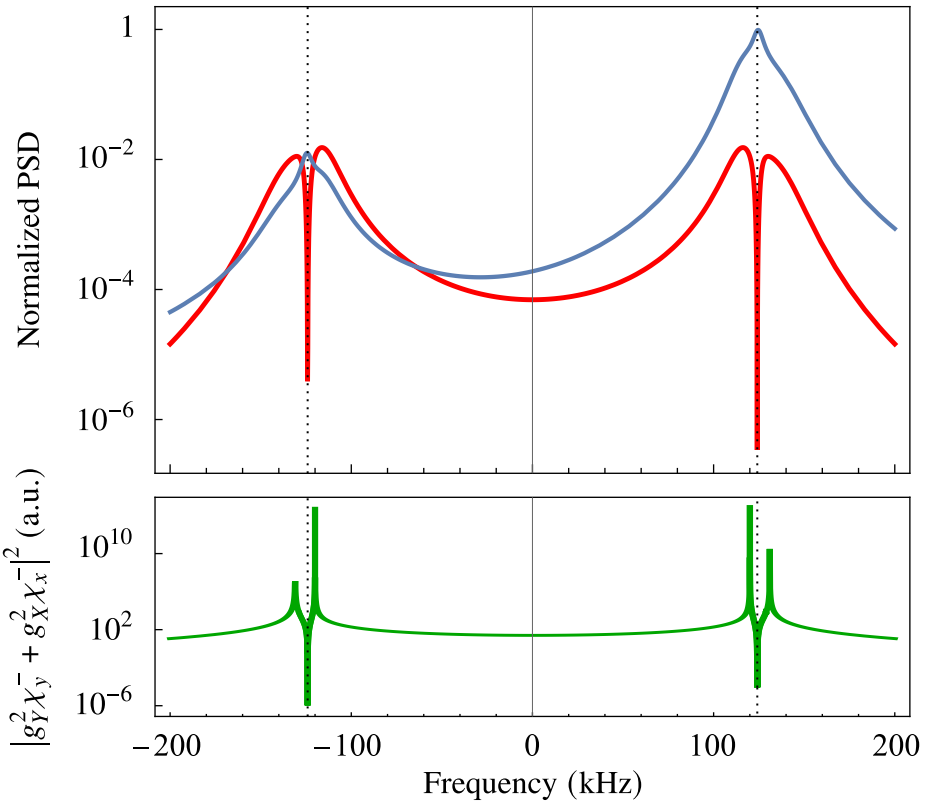

Figure 37: Upper panel: contribution to the normalized PSD from the mechanical (light blue) and optical (red) noise drive for the spectrum in Fig.(36). At the geometrical dark mode frequency (dashed vertical line) the interference term, plotted in the lower panel, goes to zero. On the Stokes sideband, close to $-\Omega_{\rm d}$, the mechanical displacement is mainly due to the cavity back action noise. In contrast, at the spectral frequency matching $-\Omega_{\rm d}$, the cavity mediated force is highly suppressed and the motion is driven by the thermal baths acting on the two mechanical oscillators (here, with *thermal bath* is considered the white noise term composed by the sum of the gas collision term and the dipole scattering heating rate). As such, the dip becomes visible in the PSD which is the sum of the two components. This feature in not visible in the anti-Stokes sideband, where the mechanical displacement is mainly determined by the thermal noise.

$\omega > \Omega_X$ the mechanical motion is driven by the sum of both the white noise and the cavity mediated back action. In the spectral region between the two bare mechanical resonances, on the other hand, the cavity noise term vanishes and the mechanical motion is sensitive to the spectrally flat noise via the bare mechanical susceptibilities of the two oscillators. Moreover, since $g_X \sim g_Y$, the interference

effect is enhanced. So, at sufficiently low pressure where the thermal heating rate becomes negligible with respect to the optical contribution (see Fig.(37)), the interference dip is visible in the spectrum. It should be emphasized that the interference dip would be present even in the Anti-Stokes sideband but it's not observed, since in that spectral region the back action heating rate is strongly suppressed by the cavity filtering and is masked by the large thermal and dipole scattering noises.

To conclude, the sideband asymmetry has the usual shape of a broad peak with a dip that reaches the value of 1 close to the dark mode frequency. The dip is broader compared to Fig.(34) because the weighted susceptibilities of the two oscillators have similar amplitude on a larger bandwidth, since $g_X \sim g_Y$.

5.12 Conclusions and outlook

In this thesis we have demonstrated the experimental realization of a quantum platform based on a macroscopic oscillator coupled to a mode of a high finesse optical cavity. With the protocol developed at the early stage of the doctoral work [11], based on the transfer of a levitated particle between two optical tweezers, we have been able to reproducibly levitate the particle in high vacuum and observe strong non classical signatures in the motional spectrum [51, 50]. Thanks to the coherent scattering setup, the oscillatory motion was strongly coupled to the cavity field thus leading to the observation of the hybrid optomechanical states, whose signature is a double avoided crossing between the three eigenfrequencies of the three-body system. These collective optical-mechanical excitations were then characterized in the quantum coherent regime, where the overall decoherence rate is lower than the system Rabi frequency. Here, we have reached the mean phononic occupation number along the *coldest* motional direction below unity, thus achieving the 1D ground state cooling. Rotating the polarization of the trapping beam with respect to the cavity optical axis, we have strongly cooled the 2D motion achieving an effective occupancy of 1.5 along the *warmest* motional direction. Moreover, the strongly broadened mechanical transfer function has allowed the observation of the quantum asymmetry on a bandwidth larger than the cavity linewidth, thus resolving the cavity mediated quantum back action noise.

We finally comment on the perspectives opened by our results. We demonstrate regimes where quantum polaritons can form. The latter are a pre-requisite for transferring quantum information between photonic and phononic components. The dark mode, weakly interacting with both the photonic field and (at low pressure) the thermal bath, is suitable for its long-term storage. The system eigenfrequencies, when varying the detuning, display two avoided-crossings, as typically observed in tripartite quantum systems. Notably, each avoided crossing acts as a quantum beam splitter of wave functions, driving an input quantum state into a coherent superposition of two output states evolving independently in time [60, 47]. Beam-splitters are basic components to realize a number of quantum operations, such as entanglement [62, 33] and teleportation [73]. The realized system thus paves the way to novel protocols for the quantum coherent control of phononic and photonic modes and represents a key-step towards the demonstration of optomechanical entangled states at room temperature. Furthermore, the phonon-polaritons form an useful basis for developing non-linear quantum optomechanics [36, 34, 7].

A Mathematical definitions

The Fourier transform of a complex classical variable $h(t)$ and its inverse are defined as:

$$\tilde{h}(\omega) = \mathcal{F}[h(t)](\omega) = \int_{-\infty}^{\infty} h(t) e^{i\omega t} dt,$$
$$h(t) = \mathcal{F}^{-1}\left[\tilde{h}(\omega)\right](t) = \int_{-\infty}^{\infty} \tilde{h}(\omega) e^{-i\omega t} \frac{d\omega}{2\pi}.$$

The convention $\tilde{h}^*(\omega) = \mathcal{F}[h^*(t)](\omega)$ is used. The power spectral density $S_{hh}(\omega)$ is defined as:

$$S_{hh}(\omega) = \lim_{\tau\to\infty} \frac{1}{\tau} \langle \tilde{h}_\tau^*(-\omega) \tilde{h}_\tau(\omega) \rangle,$$

where $\tilde{h}_\tau(\omega)$ is the Fourier transform of $h(t)$ sampled over the time period $-\tau/2 < t < \tau/2$. These definitions can be extended to the quantum domain by replacing the classical variable h with the corresponding quantum operator $\hat{h}$.

B Phase and frequency lock box

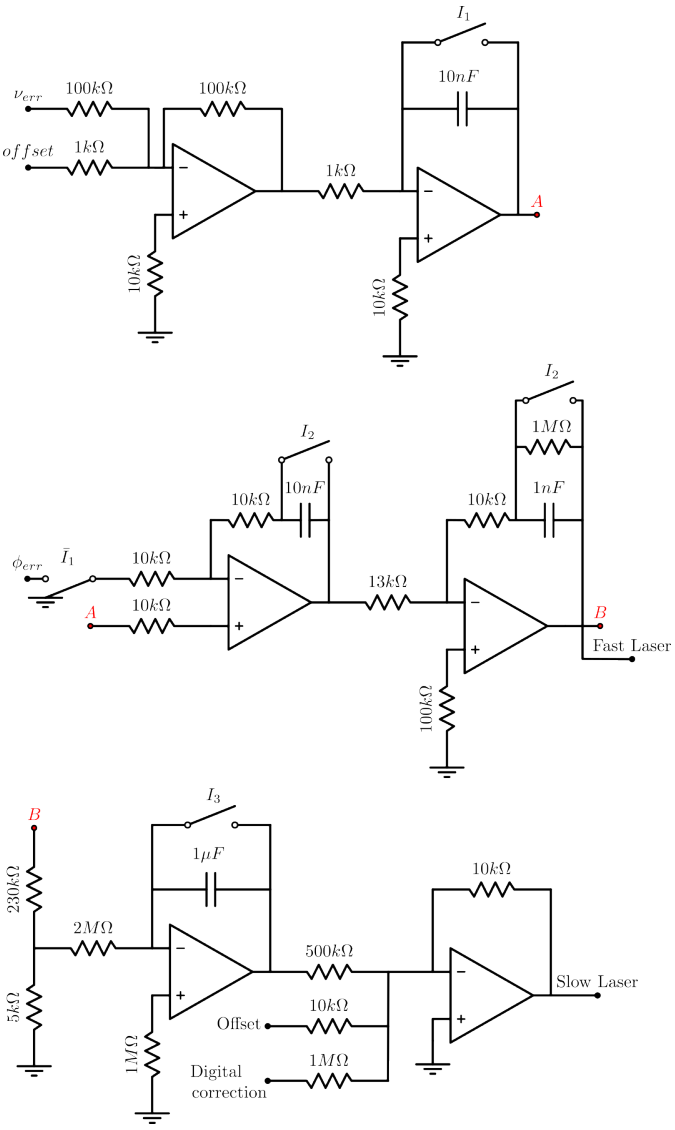

C Cavity lock box

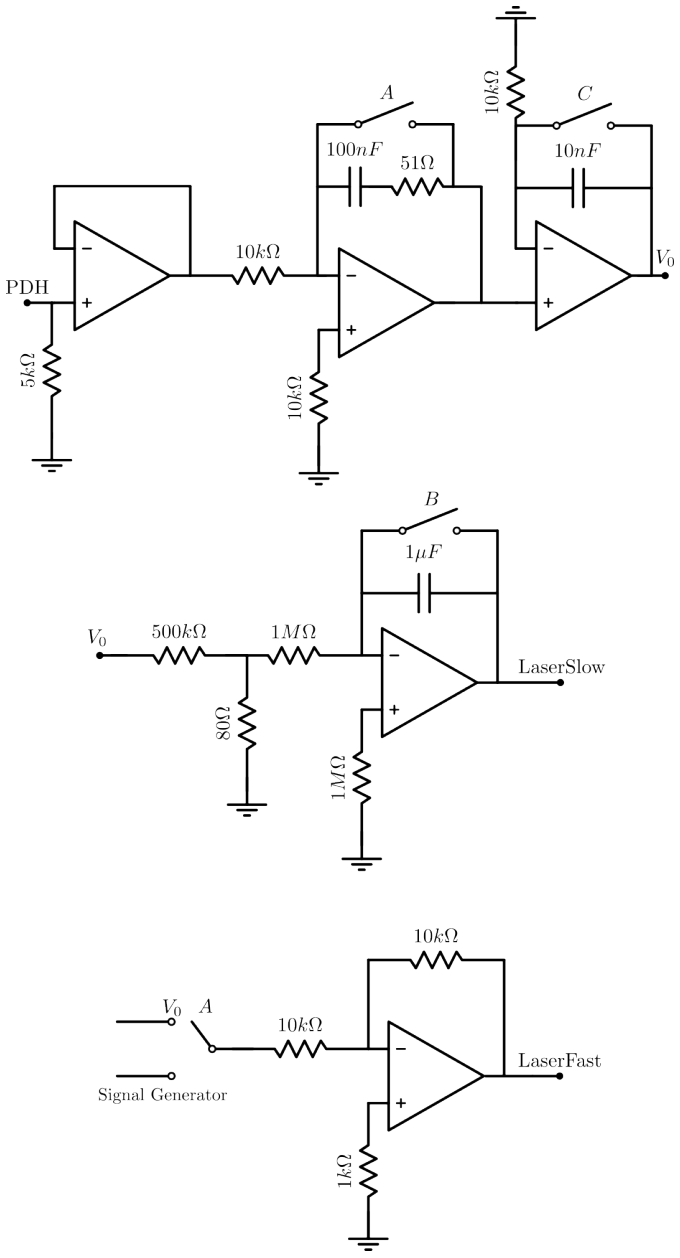

D Mathematica script for the data analysis

written for Wolfram Mathematica 12.2 on Windows 10 Pro 2004;

PREAMBLE;

CONSTANTS;

```
kb = 1.38065 × 10^-23;
ħ = 1.05457 × 10^-34;
```

EXPERIMENTAL PARAMETERS;

```
density = 1950;
radius = 125/2 × 10^-9;
mass = 4/3 π radius^3 density;
Xpf = Sqrt[ħ/(2 mass Ω1)];
Ypf = Sqrt[ħ/(2 mass Ω2)];

Pxpf = Sqrt[mass Ω1 ħ/2];
Pypf = Sqrt[mass Ω2 ħ/2];
```

MODEL;

$$\text{drift} = \begin{pmatrix} -I\Delta + \kappa/2 & 0 & -I\,g1 & -I\,g1 & -I\,g2 & -I\,g2 \\ 0 & +I\Delta + \kappa/2 & I\,g1 & I\,g1 & I\,g2 & I\,g2 \\ -I\,g1 & -I\,g1 & +I\Omega1 + \Gamma m1/2 & 0 & 0 & 0 \\ I\,g1 & I\,g1 & 0 & -I\Omega1 + \Gamma m1/2 & 0 & 0 \\ -I\,g2 & -I\,g2 & 0 & 0 & +I\Omega2 + \Gamma m2/2 & 0 \\ I\,g2 & I\,g2 & 0 & 0 & 0 & -I\Omega2 + \Gamma m2/2 \end{pmatrix};$$

```
(*drift matrix*)
mat[ω_] = -I ω IdentityMatrix[6] + drift;
```

$$\text{Nin} = \begin{pmatrix} \sqrt{\kappa} & 0 & 0 & 0 & 0 & 0 \\ 0 & \sqrt{\kappa} & 0 & 0 & 0 & 0 \\ 0 & 0 & \sqrt{\Gamma 1} & 0 & 0 & 0 \\ 0 & 0 & 0 & \sqrt{\Gamma 1} & 0 & 0 \\ 0 & 0 & 0 & 0 & \sqrt{\Gamma 2} & 0 \\ 0 & 0 & 0 & 0 & 0 & \sqrt{\Gamma 2} \end{pmatrix};\text{(*decoherence rates*)}$$

```
cav[ω_] = Dot[Inverse[mat[ω]], Nin];(*solution for the cavity field & mechanics*)
```

2 |

$$\text{out}[\omega\_] = \text{Dot}\left[\begin{pmatrix} \sqrt{\kappa} & 0 & 0 & 0 & 0 & 0 \\ 0 & \sqrt{\kappa} & 0 & 0 & 0 & 0 \\ 0 & 0 & 1 & 0 & 0 & 0 \\ 0 & 0 & 0 & 1 & 0 & 0 \\ 0 & 0 & 0 & 0 & 1 & 0 \\ 0 & 0 & 0 & 0 & 0 & 1 \end{pmatrix}, \text{cav}[\omega]\right] - \begin{pmatrix} 1 & 0 & 0 & 0 & 0 & 0 \\ 0 & 1 & 0 & 0 & 0 & 0 \\ 0 & 0 & 0 & 0 & 0 & 0 \\ 0 & 0 & 0 & 0 & 0 & 0 \\ 0 & 0 & 0 & 0 & 0 & 0 \\ 0 & 0 & 0 & 0 & 0 & 0 \end{pmatrix};$$

```
(*output field & mechanics*)

Ap = out[ω];(*    operators FT[O(t)]   *)
Am = out[-ω];(*   operators FT[O⁺(t)]   *)

Sij[i_, j_] := Am[[i, 1]]×Ap[[j, 2]] + Am[[i, 3]]×Ap[[j, 4]] + Am[[i, 4]]×Ap[[j, 3]] +
   Am[[i, 5]]×Ap[[j, 6]] + Am[[i, 6]]×Ap[[j, 5]] ;
(*taking only the non-null terms in the input noise correlation functions*)

Sa = Sij[2, 1];(*Saa(ω)*)
Sad = Sij[1, 2];(*Sa⁺a⁺(ω)*)

Sout = ((Sa /. (ω → (ω - ΩLO))) + (Sad /. (ω → (ω + ΩLO)))) η + (1 - η);(*heterodyne spectrum,
ΩLO is the frequency difference between the local oscillator and the signal field,
η is the overall detection efficiency*)


(*spectra of the correlation functions for the position operators of the mechanics*)
Sxx = Sij[3, 3] + Sij[3, 4] + Sij[4, 3] + Sij[4, 4];
Syy = Sij[5, 5] + Sij[5, 6] + Sij[6, 5] + Sij[6, 6];
Sxy = Sij[3, 5] + Sij[3, 6] + Sij[4, 5] + Sij[4, 6];
Syx = Sij[5, 3] + Sij[5, 4] + Sij[6, 3] + Sij[6, 4];

(*spectra of the correlation functions for the momenta operators of the mechanics*)
Spxx = Sij[3, 3] - Sij[3, 4] - Sij[4, 3] + Sij[4, 4];
Spyy = Sij[5, 5] - Sij[5, 6] - Sij[6, 5] + Sij[6, 6];
Spxy = Sij[3, 5] - Sij[3, 6] - Sij[4, 5] + Sij[4, 6];
Spyx = Sij[5, 3] - Sij[5, 4] - Sij[6, 3] + Sij[6, 4];
```

IMPORT DATA;

```
data = Import["E:\\path_to_data\\mydata.dat", "Data"];(*x-axis :frequency;
y-axis:(normalized PSD)-(shot noise) *)
```

FIT;

DEFINITION OF INITIAL VALUES & CONSTANTS FOR THE FIT;

| 3

$$\begin{pmatrix} \text{g1init} \\ \text{g2init} \\ \Omega\text{1init} \\ \Omega\text{2init} \\ \Delta\text{init} \\ \Gamma\text{1init} \\ \Gamma\text{2init} \\ \text{offLinit} \\ \text{offRinit} \\ \eta\text{meas} \\ \Gamma\text{m1} \\ \Gamma\text{m2} \end{pmatrix} = 2\pi \begin{pmatrix} 25\,000 \\ 2000 \\ 127\,000 \\ 116\,000 \\ -160\,000 \\ 10\,000 \\ 10\,000 \\ 0.01 \\ 0.01 \\ \frac{0.295}{2\pi} \\ 970\ \text{pressure} \\ 970\ \text{pressure} \end{pmatrix};$$

$$\begin{pmatrix} \kappa \\ \Omega\text{LO} \\ \text{pressure} \end{pmatrix} = 2\pi \begin{pmatrix} 57\,000 \\ 1.1 \times 10^6 \\ \frac{7.9}{2\pi}\ 10^{-8} \end{pmatrix};$$

DEFINITION OF THE FITTING MODEL;

```
model = 0.5 (offL^2 + offR^2) + (offL^2 - offR^2) (1 / Pi) ArcTan[x] + (Sout - 1) /.
    ω → 2 Pi (x + 1 100 000);
```

CONVERSION FOR LOGARITHMIC FITTING;

```
modlog = Log10[Abs[model]];
datilog = Transpose[{data[[All, 1]], Log10[data[[All, 2]]]}];
```

FITTING;

```
fit = NonlinearModelFit[datilog, (modlog /. {η -> ηmeas}),
    {{g1, g1init}, {Ω1, Ω1init}, {g2, g2init}, {Ω2, Ω2init}, {offL, offLinit},
     {offR, offRinit}, {Γ1, Γ1init}, {Γ2, Γ2init}, {Δ, Δinit}}, x];
```

PLOT OF THE DATA / FITTING FUNCTION;

```
Show[{ListPlot[datilog, PlotRange → All],
  Plot[modlog /. fit["BestFitParameters"] /. {η → ηmeas}, {x, -170 000, 170 000},
   PlotStyle → {Red}, PlotRange → All]}, ImageSize → Full]
```

PRINTING THE BEST FIT PARAMETERS;

```
{Ω1, Ω2, g1, g2, Γ1, Γ2, Δ} / (2 π) /. fit["BestFitParameters"] // Print
```

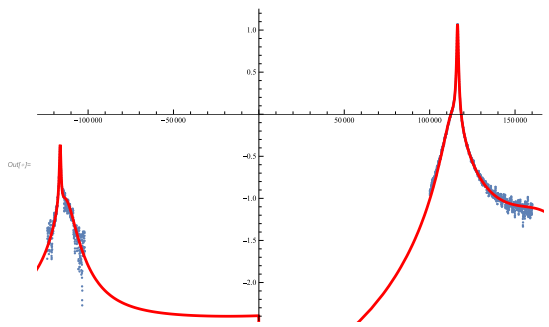

{128 133., 115 944., 25 338.2, 3736.95, 8808.54, 7842.48, −161 050.}

4

EVALUATION OF THE EFFECTIVE PHONONIC OCCUPATION NUMBER;

```
In[•]:= MR = ( Cos[θ]^2          Sin[2 θ]/2
               Sin[2 θ]/2        Sin[θ]^2 );
```

```
(*matrix to get the effective phononic number along any direction*)

SM = ( Sxx Xpf^2     Sxy Xpf Ypf
       Syx Xpf Ypf   Syy Ypf^2 );(*spectra of position correlations*)

SpM = ( Spxx ( i Pxpf)^2          Spxy ( i Pxpf) (i Pypf)
        Spyx ( i Pxpf) ( i Pypf)  Spyy ( i Pypf)^2 );

(*spectra of momenta correlations*)
```

NUMERICAL INTEGRALS;

```
Stemp = (SM /. fit["BestFitParameters"]) /. ω → 2 Pi ν;

IS = NIntegrate[Stemp, {ν, -10^7, -10^6}] + NIntegrate[Stemp, {ν, -10^6, -180000}] +
    NIntegrate[Stemp, {ν, -180000, -140000}] + NIntegrate[Stemp, {ν, -140000, -100000}] +
    NIntegrate[Stemp, {ν, -100000, 0}] + NIntegrate[Stemp, {ν, 0, 100000}] +
    NIntegrate[Stemp, {ν, 100000, 140000}] + NIntegrate[Stemp, {ν, 140000, 180000}] +
    NIntegrate[Stemp, {ν, 180000, 10^6}] + NIntegrate[Stemp, {ν, 10^6, 10^7}] +
    ((Stemp /. ν → 10^7) + (Stemp /. ν → -10^7) ) 10^7;

Clear[Stemp];
Stemp = (SpM /. fit["BestFitParameters"]) /. ω → 2 Pi ν;

ISp = NIntegrate[Stemp, {ν, -10^7, -10^6}] + NIntegrate[Stemp, {ν, -10^6, -180000}] +
    NIntegrate[Stemp, {ν, -180000, -140000}] + NIntegrate[Stemp, {ν, -140000, -100000}] +
    NIntegrate[Stemp, {ν, -100000, 0}] + NIntegrate[Stemp, {ν, 0, 100000}] +
    NIntegrate[Stemp, {ν, 100000, 140000}] + NIntegrate[Stemp, {ν, 140000, 180000}] +
    NIntegrate[Stemp, {ν, 180000, 10^6}] + NIntegrate[Stemp, {ν, 10^6, 10^7}] +
    ((Stemp /. ν → 10^7) + (Stemp /. ν → -10^7) ) 10^7;
```

APPLYING THE ROTATION;

```
i1 = Abs[Total[IS * MR, 2]];
i2 = Abs[Total[ISp * MR, 2]];
```

PHONONIC OCCUPATION NUMBER AS A FUNCTION OF θ

($*\theta$=0 → motion 1;
θ=π/2 → motion 2$*$);

```
nn = ( Abs[ √(i1 i2 (4/ħ^2)) ] - 1 ) * 0.5;
```

E Pictures of the apparatus

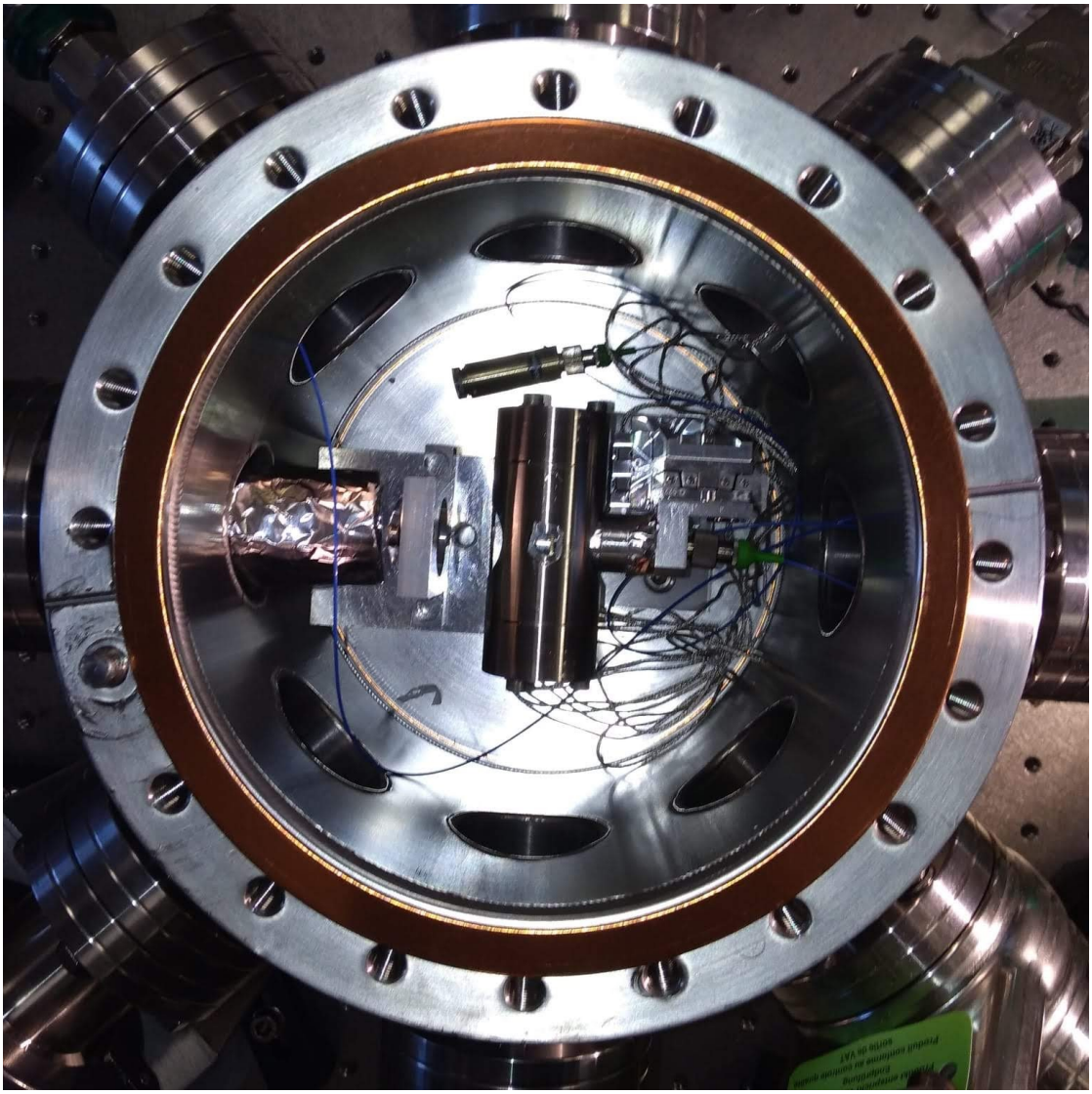

Figure 38: Vacuum chamber, top view.

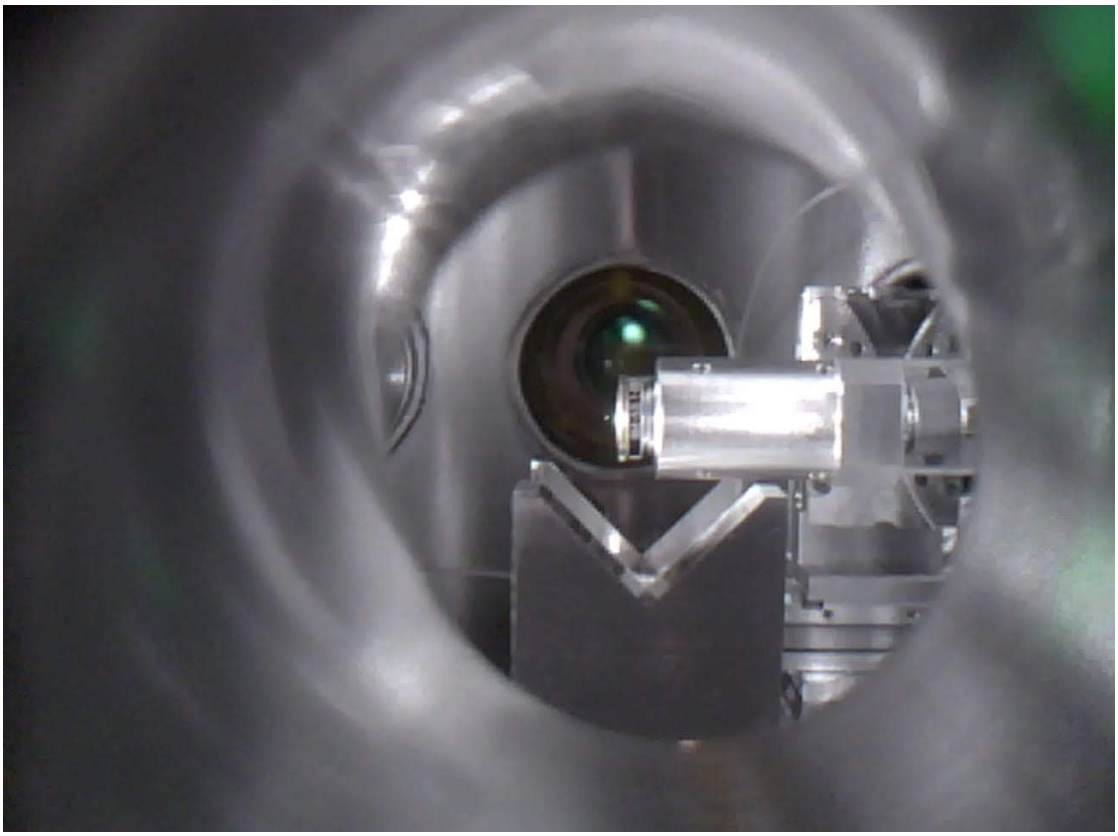

Figure 39: Vacuum chamber without the cavity, side view from the window.

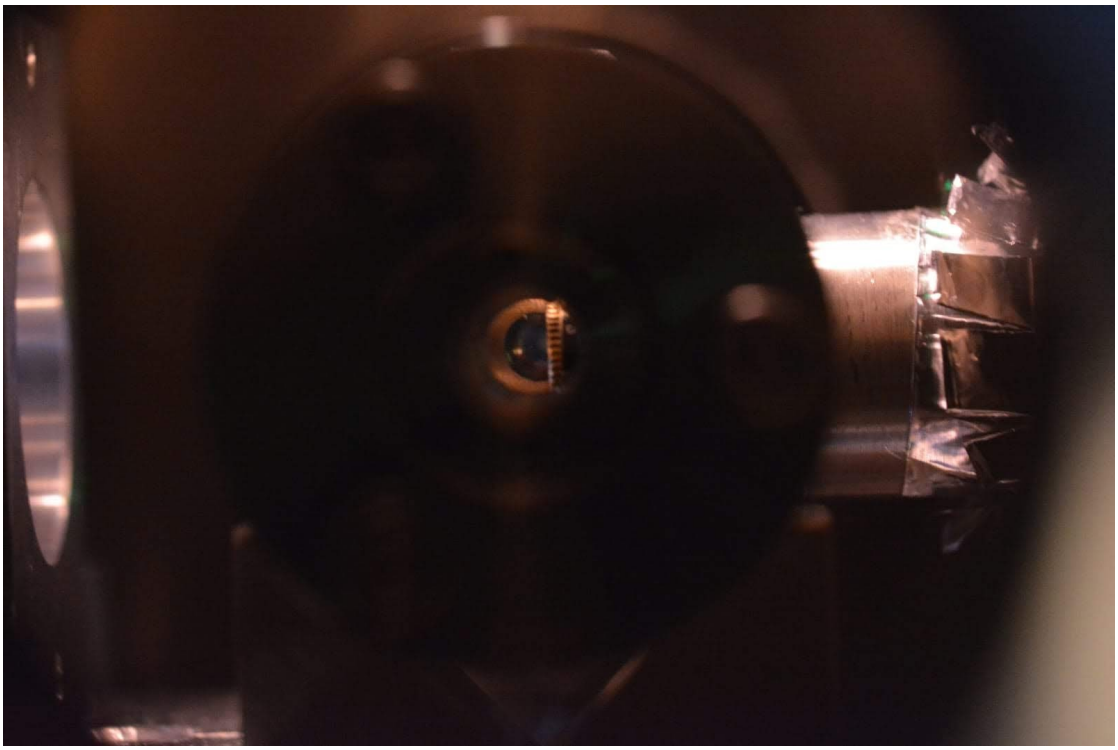

Figure 40: Vacuum chamber, side view showing the tweezer inside the cavity.

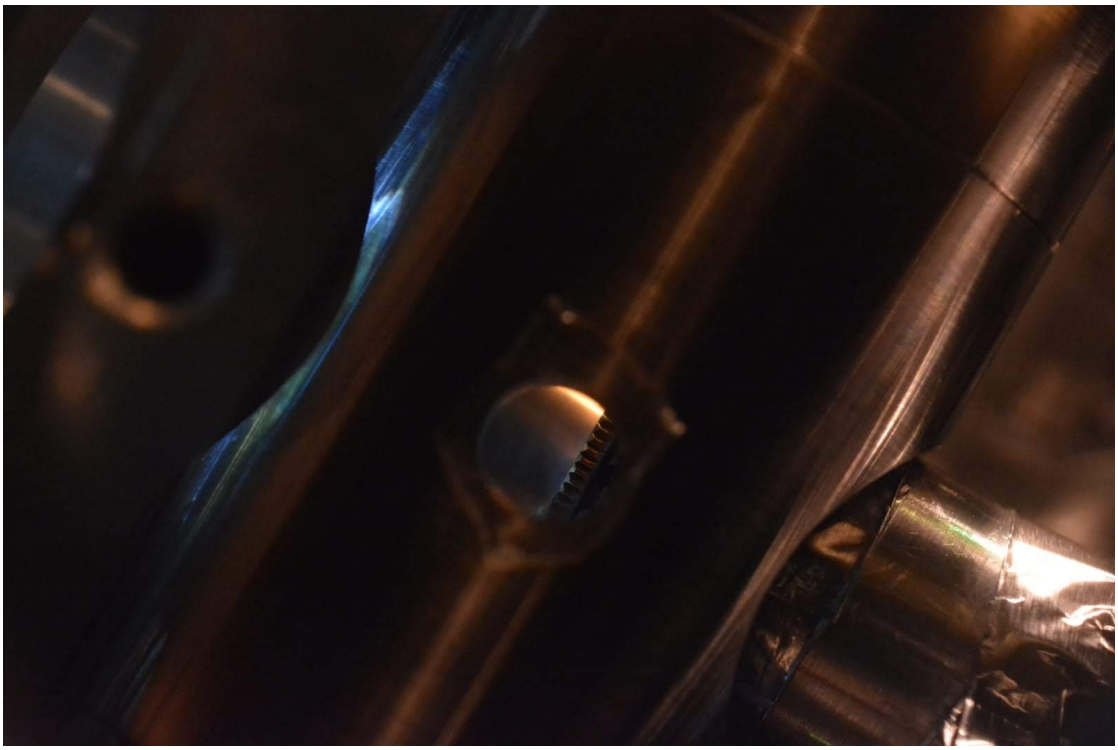

Figure 41: Top view of the cavity and the tweezer.

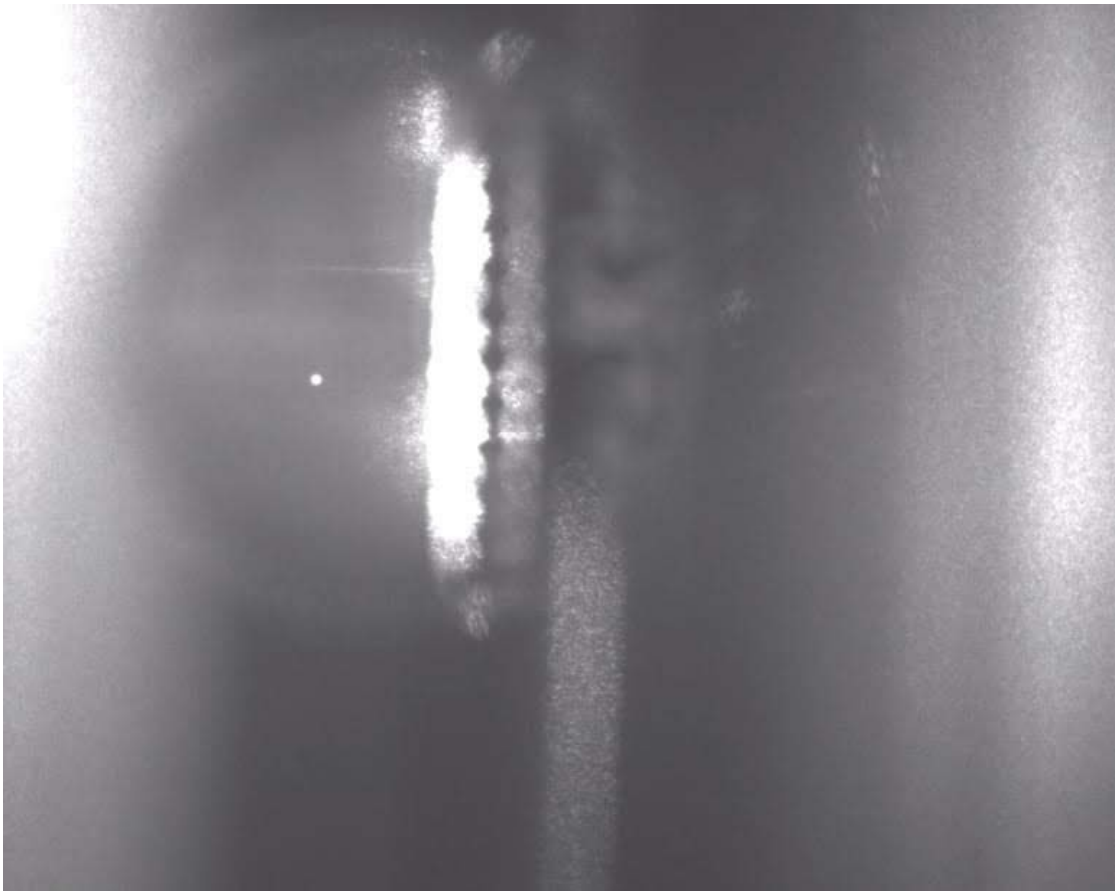

Figure 42: Top view of a nanoparticle levitating on the cavity axis in high vacuum.

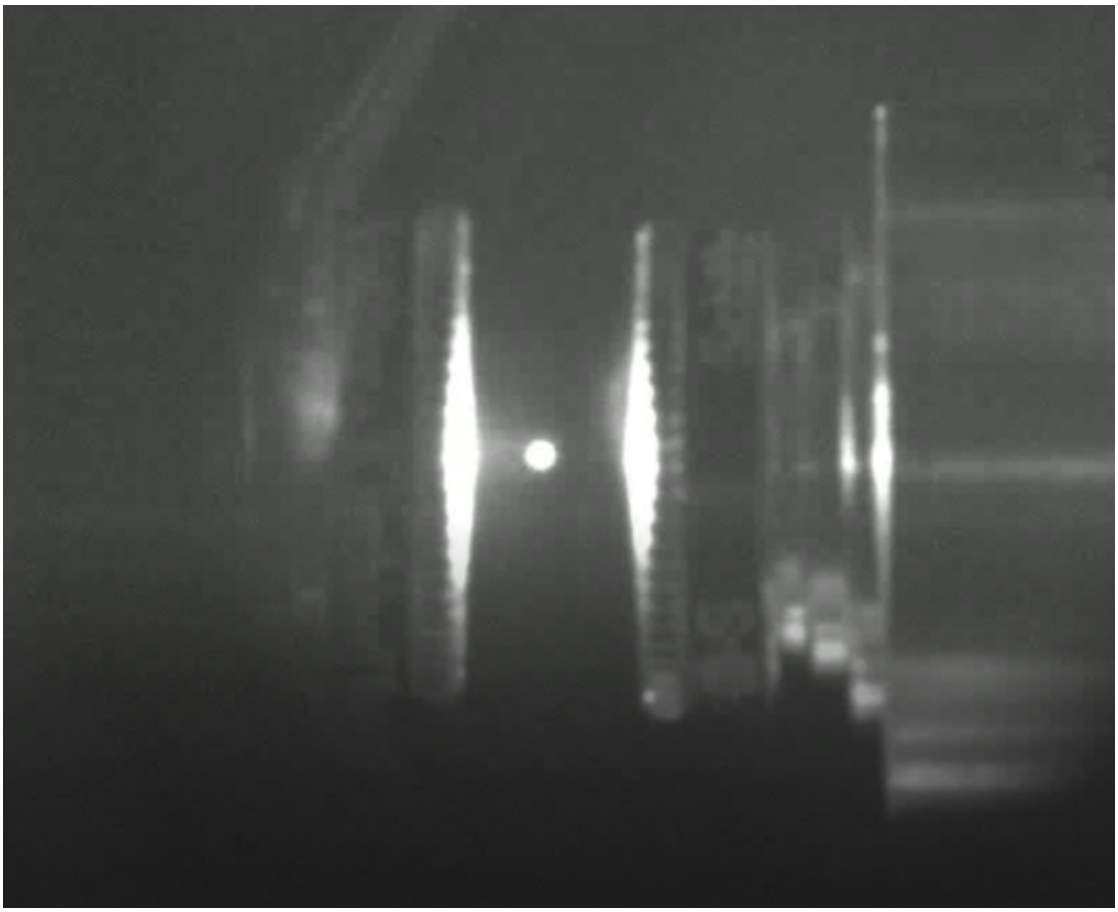

Figure 43: Transfer of a levitated nanoparticle between the two optical tweezers.

References

[1] F. Altomare, J. I. Park, K. Cicak, M. A. Sillanpää, M. S. Allman, D. Li, A. Sirois, J. A. Strong, J. D. Whittaker, and R. W. Simmonds. "Tripartite interactions between two phase qubits and a resonant cavity". In: *Nature Physics* 6.10 (2010), pp. 777–781. ISSN: 1745-2481. DOI: 10.1038/nphys1731. URL: https://doi.org/10.1038/nphys1731.

[2] A. Ashkin. "Acceleration and Trapping of Particles by Radiation Pressure". In: *Phys. Rev. Lett.* 24.4 (1970), pp. 156–159. DOI: 10.1103/PhysRevLett.24.156. URL: https://link.aps.org/doi/10.1103/PhysRevLett.24.156.

[3] M. Aspelmeyer, T. J. Kippenberg, and F. Marquardt. "Cavity optomechanics". In: *Rev. Mod. Phys.* 86.4 (2014), pp. 1391–1452. DOI: 10.1103/RevModPhys.86.1391. URL: https://link.aps.org/doi/10.1103/RevModPhys.86.1391.

[4] P. F. Barker and M. N. Shneider. "Cavity cooling of an optically trapped nanoparticle". In: *Phys. Rev. A* 81.2 (2010), p. 023826. DOI: 10.1103/PhysRevA.81.023826. URL: https://link.aps.org/doi/10.1103/PhysRevA.81.023826.

[5] S. Beresnev, V. Chernyak, and G. Fomyagin. "Motion of a spherical particle in a rarefied gas. Part 2. Drag and thermal polarization". In: *Journal of Fluid Mechanics* 219 (Oct. 1990), pp. 405 –421. DOI: 10.1017/S0022112090003007.

[6] K. Børkje. "Heterodyne photodetection measurements on cavity optomechanical systems: Interpretation of sideband asymmetry and limits to a classical explanation". In: *Physical Review A* 94 (Aug. 2016). DOI: 10.1103/PhysRevA.94.043816.

[7] K. Børkje, A. Nunnenkamp, J. D. Teufel, and S. M. Girvin. "Signatures of Nonlinear Cavity Optomechanics in the Weak Coupling Regime". In: *Phys. Rev. Lett.* 111.5 (2013), p. 053603. DOI: 10.1103/PhysRevLett.111.053603. URL: https://link.aps.org/doi/10.1103/PhysRevLett.111.053603.

[8] W. Bowen and G. Milburn. *Quantum Optomechanics*. CRC Press, 2015. ISBN: 9781482259162. URL: https://books.google.it/books?id=YZDwCgAAQBAJ.

[9] V. B. Braginskiĭ and A. B. Manukin. "Ponderomotive Effects of Electromagnetic Radiation". In: *Soviet Journal of Experimental and Theoretical Physics* 25 (Oct. 1967), p. 653.

[10] V. B. Braginskiĭ, A. B. Manukin, and M. Y. Tikhonov. "Investigation of Dissipative Ponderomotive Effects of Electromagnetic Radiation". In: *Soviet Journal of Experimental and Theoretical Physics* 31 (Jan. 1970), p. 829.

[11] M. Calamai, A. Ranfagni, and F. Marin. "Transfer of a levitating nanoparticle between optical tweezers". In: *AIP Advances* 11.2 (2021), p. 025246. DOI: 10.1063/5.0024432. eprint: https://doi.org/10.1063/5.0024432. URL: https://doi.org/10.1063/5.0024432.

[12] D. E. Chang, C. A. Regal, S. B. Papp, D. J. Wilson, J. Ye, O. Painter, H. J. Kimble, and P. Zoller. "Cavity opto-mechanics using an optically levitated nanosphere". In: *Proceedings of the National Academy of Sciences* 107.3 (2010), pp. 1005–1010. ISSN: 0027-8424. DOI: 10.1073/pnas.0912969107. eprint: https://www.pnas.org/content/107/3/1005.full.pdf. URL: https://www.pnas.org/content/107/3/1005.

[13] A. A. Clerk, M. H. Devoret, S. M. Girvin, F. Marquardt, and R. J. Schoelkopf. "Introduction to quantum noise, measurement, and amplification". In: *Rev. Mod. Phys.* 82.2 (2010), pp. 1155–1208. DOI: 10.1103/RevModPhys.82.1155. URL: https://link.aps.org/doi/10.1103/RevModPhys.82.1155.

[14] Y. Colombe, T. Steinmetz, G. Dubois, F. Linke, D. Hunger, and J. Reichel. "Strong atom–field coupling for Bose–Einstein condensates in an optical cavity on a chip". In: *Nature* 450.7167 (2007), pp. 272–276. ISSN: 1476-4687. DOI: 10.1038/nature06331. URL: https://doi.org/10.1038/nature06331.

[15] U. Delić, M. Reisenbauer, K. Dare, D. Grass, V. Vuletić, N. Kiesel, and M. Aspelmeyer. "Cooling of a levitated nanoparticle to the motional quantum ground state". In: *Science* 367.6480 (2020), pp. 892–895. ISSN: 0036-8075. DOI: 10.1126/science.aba3993. eprint: https://science.sciencemag.org/content/367/6480/892.full.pdf. URL: https://science.sciencemag.org/content/367/6480/892.

[16] U. Delić, M. Reisenbauer, D. Grass, N. Kiesel, V. Vuletic, and M. Aspelmeyer. "Cavity Cooling of a Levitated Nanosphere by Coherent Scattering". In: *Physical Review Letters* 122.12 (Mar. 2019), p. 123602. DOI: 10.1103/PhysRevLett.122.123602. URL: https://link.aps.org/doi/10.1103/PhysRevLett.122.123602.

[17] R. Drever, J. Hall, F. Kowalski, J. Hough, G. Ford, A. Munley, and H. Ward. "Laser Phase and Frequency Stabilization Using an Optical Resonator". In: *Appl. Phys. B* 31 (June 1983), pp. 97–105. DOI: 10.1007/BF00702605.

[18] A. Duri, D. A. Sessoms, V. Trappe, and L. Cipelletti. "Resolving Long-Range Spatial Correlations in Jammed Colloidal Systems Using Photon Correlation Imaging". In: *Phys. Rev. Lett.* 102.8 (2009), p. 085702. DOI: 10.1103/PhysRevLett.102.085702. URL: https://link.aps.org/doi/10.1103/PhysRevLett.102.085702.

[19] P. S. Epstein. "On the Resistance Experienced by Spheres in their Motion through Gases". In: *Phys. Rev.* 23.6 (1924), pp. 710–733. DOI: 10.1103/PhysRev.23.710. URL: https://link.aps.org/doi/10.1103/PhysRev.23.710.

[20] C. Genes, D. Vitali, and P. Tombesi. "Simultaneous cooling and entanglement of mechanical modes of a micromirror in an optical cavity". In: *New Journal of Physics* 10.9 (2008), p. 095009. DOI: 10.1088/1367-2630/10/9/095009. URL: https://doi.org/10.1088/1367-2630/10/9/095009.

[21] J. Gieseler, B. Deutsch, R. Quidant, and L. Novotny. "Subkelvin Parametric Feedback Cooling of a Laser-Trapped Nanoparticle". In: *Phys. Rev. Lett.* 109.10 (2012), p. 103603. DOI: 10.1103/PhysRevLett.109.103603. URL: https://link.aps.org/doi/10.1103/PhysRevLett.109.103603.

[22] C. Gonzalez-Ballestero, P. Maurer, D. Windey, L. Novotny, R. Reimann, and O. Romero-Isart. "Theory for cavity cooling of levitated nanoparticles via coherent scattering: Master equation approach". In: *Phys. Rev. A* 100.1 (2019), p. 013805. DOI: 10.1103/PhysRevA.100.013805. URL: https://link.aps.org/doi/10.1103/PhysRevA.100.013805.

[23] D. Grass, J. Fesel, S. G. Hofer, N. Kiesel, and M. Aspelmeyer. "Optical trapping and control of nanoparticles inside evacuated hollow core photonic crystal fibers". In: *Applied Physics Letters* 108.22 (2016), p. 221103. DOI: 10.1063/1.4953025. eprint: https://doi.org/10.1063/1.4953025. URL: https://doi.org/10.1063/1.4953025.

[24] S. Gröblacher, K. Hammerer, M. R. Vanner, and M. Aspelmeyer. "Observation of strong coupling between a micromechanical resonator and an optical cavity field". In: *Nature* 460.7256 (2009), pp. 724–727. ISSN: 1476-4687. DOI: 10.1038/nature08171. URL: https://doi.org/10.1038/nature08171.

[25] E. Hebestreit, M. Frimmer, R. Reimann, and L. Novotny. "Sensing Static Forces with Free-Falling Nanoparticles". In: *Phys. Rev. Lett.* 121.6 (2018), p. 063602. DOI: 10.1103/PhysRevLett.121.063602. URL: https://link.aps.org/doi/10.1103/PhysRevLett.121.063602.

[26] J. J. Hopfield. "Theory of the Contribution of Excitons to the Complex Dielectric Constant of Crystals". In: *Phys. Rev.* 112.5 (1958), pp. 1555–1567. DOI: 10.1103/PhysRev.112.1555. URL: https://link.aps.org/doi/10.1103/PhysRev.112.1555.

[27] K. Huang and M. Born. "On the interaction between the radiation field and ionic crystals". In: *Proceedings of the Royal Society of London. Series A. Mathematical and Physical Sciences* 208.1094 (1951), pp. 352–365. DOI: 10.1098/rspa.1951.0166. eprint: https://royalsocietypublishing.org/doi/pdf/10.1098/rspa.1951.0166. URL: https://royalsocietypublishing.org/doi/abs/10.1098/rspa.1951.0166.

[28] H. Huebl, C. W. Zollitsch, J. Lotze, F. Hocke, M. Greifenstein, A. Marx, R. Gross, and S. T. B. Goennenwein. "High Cooperativity in Coupled Microwave Resonator Ferrimagnetic Insulator Hybrids". In: *Phys. Rev. Lett.* 111.12 (2013), p. 127003. DOI: 10.1103/PhysRevLett.111.127003. URL: https://link.aps.org/doi/10.1103/PhysRevLett.111.127003.

[29] V. Jain, J. Gieseler, C. Moritz, C. Dellago, R. Quidant, and L. Novotny. "Direct Measurement of Photon Recoil from a Levitated Nanoparticle". In: *Phys. Rev. Lett.* 116.24 (2016), p. 243601. DOI: 10.1103/PhysRevLett.116.243601. URL: https://link.aps.org/doi/10.1103/PhysRevLett.116.243601.

[30] E. T. Jaynes and F. W. Cummings. "Comparison of quantum and semiclassical radiation theories with application to the beam maser". In: *Proceedings of the IEEE* 51.1 (1963), pp. 89–109. ISSN: 1558-2256. DOI: 10.1109/PROC.1963.1664.

[31] F. Y. Khalili, H. Miao, H. Yang, A. H. Safavi-Naeini, O. Painter, and Y. Chen. "Quantum back-action in measurements of zero-point mechanical oscillations". In: *Phys. Rev. A* 86.3 (2012), p. 033840. DOI: 10.1103/PhysRevA.86.033840. URL: https://link.aps.org/doi/10.1103/PhysRevA.86.033840.

[32] N. Kiesel, F. Blaser, U. Delić, D. Grass, R. Kaltenbaek, and M. Aspelmeyer. "Cavity cooling of an optically levitated submicron particle". In: *Proceedings of the National Academy of Sciences* 110.35 (2013), pp. 14180–14185. ISSN: 0027-8424. DOI: 10.1073/pnas.1309167110. eprint: https://www.pnas.org/content/110/35/14180.full.pdf. URL: https://www.pnas.org/content/110/35/14180.

[33] M. S. Kim, W. Son, and P. L. Knight. "Entanglement by a beam splitter: Nonclassicality as a prerequisite for entanglement". In: *Phys. Rev. A* 65.3 (2002), p. 032323. DOI: 10.1103/PhysRevA.65.032323. URL: https://link.aps.org/doi/10.1103/PhysRevA.65.032323.

[34] M.-A. Lemonde, N. Didier, and A. A. Clerk. "Nonlinear Interaction Effects in a Strongly Driven Optomechanical Cavity". In: *Phys. Rev. Lett.* 111.5 (2013), p. 053602. DOI: 10.1103/PhysRevLett.111.053602. URL: https://link.aps.org/doi/10.1103/PhysRevLett.111.053602.

[35] T. Li, S. Kheifets, and M. Raizen. "Millikelvin cooling of an optically trapped microsphere in vacuum". In: *Nature Physics* 7.3 (Jan. 2011), p. 032323. DOI: 10.1038/nphys1952. URL: https://link.aps.org/doi/10.1103/PhysRevA.65.032323.

[36] Y.-C. Liu, Y.-F. Xiao, Y.-L. Chen, X.-C. Yu, and Q. Gong. "Parametric Down-Conversion and Polariton Pair Generation in Optomechanical Systems". In: *Phys. Rev. Lett.* 111.8 (2013), p. 083601. DOI: 10.1103/PhysRevLett.111.083601. URL: https://link.aps.org/doi/10.1103/PhysRevLett.111.083601.

[37] L. Magrini, P. Rosenzweig, C. Bach, A. Deutschmann-Olek, S. G. Hofer, S. Hong, N. Kiesel, A. Kugi, and M. Aspelmeyer. "Real-time optimal quantum control of mechanical motion at room temperature". In: *Nature* 595.7867 (2021), pp. 373–377. ISSN: 1476-4687. DOI: 10.1038/s41586-021-03602-3. URL: https://doi.org/10.1038/s41586-021-03602-3.

[38] F. Marquardt, J. P. Chen, A. A. Clerk, and S. M. Girvin. "Quantum Theory of Cavity-Assisted Sideband Cooling of Mechanical Motion". In: *Phys. Rev. Lett.* 99.9 (2007), p. 093902. DOI: 10.1103/PhysRevLett.99.093902. URL: https://link.aps.org/doi/10.1103/PhysRevLett.99.093902.

[39] F. Massel, S. U. Cho, J.-M. Pirkkalainen, P. J. Hakonen, T. T. Heikkilä, and M. A. Sillanpää. "Multimode circuit optomechanics near the quantum limit". In: *Nature Communications* 3.1 (2012), p. 987. ISSN: 2041-1723. DOI: 10.1038/ncomms1993. URL: https://doi.org/10.1038/ncomms1993.

[40] P. Mestres, J. Berthelot, M. SpasenoviÄ, J. Gieseler, L. Novotny, and R. Quidant. "Cooling and manipulation of a levitated nanoparticle with an optical fiber trap". In: *Applied Physics Letters* 107.15 (2015), p. 151102. DOI: 10.1063/1.4933180. eprint: https://doi.org/10.1063/1.4933180. URL: https://doi.org/10.1063/1.4933180.

[41] P. Meystre. "A short walk through quantum optomechanics". In: *Annalen der Physik* 525.3 (2013), pp. 215–233. DOI: https://doi.org/10.1002/andp.201200226. eprint: https://onlinelibrary.wiley.com/doi/pdf/10.1002/andp.201200226. URL: https://onlinelibrary.wiley.com/doi/abs/10.1002/andp.201200226.

[42] J. Millen, T. Deesuwan, P. Barker, and J. Anders. "Nanoscale temperature measurements using non-equilibrium Brownian dynamics of a levitated nanosphere". In: *Nature Nanotechnology* 9.6 (2014), pp. 425–429. ISSN: 1748-3395. DOI: 10.1038/nnano.2014.82. URL: https://doi.org/10.1038/nnano.2014.82.

[43] J. Millen, T. S. Monteiro, R. Pettit, and A. N. Vamivakas. "Optomechanics with levitated particles". In: *Reports on Progress in Physics* 83.2 (2020), p. 026401. DOI: 10.1088/1361-6633/ab6100. URL: https://doi.org/10.1088/1361-6633/ab6100.

[44] J. Millen, T. S. Monteiro, R. Pettit, and A. N. Vamivakas. "Optomechanics with levitated particles". In: *Reports on Progress in Physics* 83.2 (2020), p. 026401. DOI: 10.1088/1361-6633/ab6100. URL: https://doi.org/10.1088%2F1361-6633%2Fab6100.

[45] N. Nakamura, D. Kato, and S. Ohtani. "Evidence for strong configuration mixing in $n = 3$ excited levels in neonlike ions". In: *Phys. Rev. A* 61.5 (2000), p. 052510. DOI: 10.1103/PhysRevA.61.052510. URL: https://link.aps.org/doi/10.1103/PhysRevA.61.052510.

[46] L. Novotny and B. Hecht. *Principles of Nano-Optics*. 2nd ed. Vol. 65. 3. Cambridge University Press, 2012, p. 032323. DOI: 10.1017/CBO9780511794193. URL: https://link.aps.org/doi/10.1103/PhysRevA.65.032323.

[47] J. R. Petta, H. Lu, and A. C. Gossard. "A Coherent Beam Splitter for Electronic Spin States". In: *Science* 327.5966 (2010), pp. 669–672. ISSN: 0036-8075. DOI: 10.1126/science.1183628. eprint: https://science.sciencemag.org/content/327/5966/669.full.pdf. URL: https://science.sciencemag.org/content/327/5966/669.

[48] J. Piotrowski, D. Windey, J. Vijayan, C. Gonzalez-Ballestero, A. d. l. R. Sommer, N. Meyer, R. Quidant, O. Romero-Isart, R. Reimann, and L. Novotny. "Simultaneous ground-state cooling of two mechanical modes of a levitated nanoparticle". In: *Phys. Rev. A* 65.3 (2022), p. 032323. DOI: 10.48550/ARXIV.2209.15326. URL: https://arxiv.org/abs/2209.15326.

[49] J.-M. Pirkkalainen, E. Damskägg, M. Brandt, F. Massel, and M. A. Sillanpää. "Squeezing of Quantum Noise of Motion in a Micromechanical Resonator". In: *Phys. Rev. Lett.* 115.24 (2015), p. 243601. DOI: 10.1103/PhysRevLett.115.243601. URL: https://link.aps.org/doi/10.1103/PhysRevLett.115.243601.

[50] A. Ranfagni, K. Børkje, F. Marino, and F. Marin. "Two-dimensional quantum motion of a levitated nanosphere". In: *Phys. Rev. Research* 4.3 (2022), p. 033051. DOI: 10.1103/PhysRevResearch.4.033051. URL: https://link.aps.org/doi/10.1103/PhysRevResearch.4.033051.

[51] A. Ranfagni, P. Vezio, M. Calamai, A. Chowdhury, F. Marino, and F. Marin. "Vectorial polaritons in the quantum motion of a levitated nanosphere". In: *Nature Physics* 17.10 (2021), pp. 1120–1124. ISSN: 1745-2481. DOI: 10.1038/s41567-021-01307-y. URL: https://doi.org/10.1038/s41567-021-01307-y.

[52] J. P. Reithmaier, G. Skek, A. Löffler, C. Hofmann, S. Kuhn, S. Reitzenstein, L. V. Keldysh, V. D. Kulakovskii, T. L. Reinecke, and A. Forchel. "Strong coupling in a single quantum dot–semiconductor microcavity system". In: *Nature* 432.7014 (2004), pp. 197–200. ISSN: 1476-4687. DOI: 10.1038/nature02969. URL: https://doi.org/10.1038/nature02969.

[53] A. de los Ríos Sommer, N. Meyer, and R. Quidant. "Strong optomechanical coupling at room temperature by coherent scattering". In: *Nature Communications* 12.1 (2021), p. 276. ISSN: 2041-1723. DOI: 10.1038/s41467-020-20419-2. URL: https://doi.org/10.1038/s41467-020-20419-2.

[54] O. Romero-Isart, M. Juan, R. Quidant, and J. Cirac. "Toward Quantum Superposition of Living Organisms". In: *New Journal of Physics* 12.3 (Mar. 2010), p. 033015. DOI: 10.1088/1367-2630/12/3/033015. URL: https://link.aps.org/doi/10.1103/PhysRevA.65.032323.

[55] A. H. Safavi-Naeini, J. Chan, J. T. Hill, T. P. M. Alegre, A. Krause, and O. Painter. "Observation of Quantum Motion of a Nanomechanical Resonator". In: *Phys. Rev. Lett.* 108.3 (2012), p. 033602. DOI: 10.1103/PhysRevLett.108.033602. URL: https://link.aps.org/doi/10.1103/PhysRevLett.108.033602.

[56] T. A. Savard, K. M. O'Hara, and J. E. Thomas. "Laser-noise-induced heating in far-off resonance optical traps". In: *Phys. Rev. A* 56.2 (1997), R1095–R1098. DOI: 10.1103/PhysRevA.56.R1095. URL: https://link.aps.org/doi/10.1103/PhysRevA.56.R1095.

[57] J. Schwinger. "Brownian Motion of a Quantum Oscillator". In: *Journal of Mathematical Physics* 2.3 (1961), pp. 407–432. DOI: 10.1063/1.1703727. eprint: https://doi.org/10.1063/1.1703727. URL: https://doi.org/10.1063/1.1703727.

[58] T. Seberson and F. Robicheaux. "Distribution of laser shot-noise energy delivered to a levitated nanoparticle". In: *Phys. Rev. A* 102.3 (2020), p. 033505. DOI: 10.1103/PhysRevA.102.033505. URL: https://link.aps.org/doi/10.1103/PhysRevA.102.033505.

[59] A. B. Shkarin, N. E. Flowers-Jacobs, S. W. Hoch, A. D. Kashkanova, C. Deutsch, J. Reichel, and J. G. E. Harris. "Optically Mediated Hybridization between Two Mechanical Modes". In: *Phys. Rev. Lett.* 112.1 (2014), p. 013602. DOI: 10.1103/PhysRevLett.112.013602. URL: https://link.aps.org/doi/10.1103/PhysRevLett.112.013602.

[60] G. Sun, X. Wen, B. Mao, J. Chen, Y. Yu, P. Wu, and S. Han. "Tunable quantum beam splitters for coherent manipulation of a solid-state tripartite qubit system". In: *Nature Communications* 1.1 (2010), p. 51. ISSN: 2041-1723. DOI: 10.1038/ncomms1050. URL: https://doi.org/10.1038/ncomms1050.

[61] Y. Tabuchi, S. Ishino, T. Ishikawa, R. Yamazaki, K. Usami, and Y. Nakamura. "Hybridizing Ferromagnetic Magnons and Microwave Photons in the Quantum Limit". In: *Phys. Rev. Lett.* 113.8 (2014), p. 083603. DOI: 10.1103/PhysRevLett.113.083603. URL: https://link.aps.org/doi/10.1103/PhysRevLett.113.083603.

[62] S. M. Tan, D. F. Walls, and M. J. Collett. "Nonlocality of a single photon". In: *Phys. Rev. Lett.* 66.3 (1991), pp. 252–255. DOI: 10.1103/PhysRevLett.66.252. URL: https://link.aps.org/doi/10.1103/PhysRevLett.66.252.

[63] F. Tebbenjohanns, M. L. Mattana, M. Rossi, M. Frimmer, and L. Novotny. "Quantum control of a nanoparticle optically levitated in cryogenic free space". In: *Nature* 595.7867 (2021), pp. 378–382. ISSN: 1476-4687. DOI: 10.1038/s41586-021-03617-w. URL: https://doi.org/10.1038/s41586-021-03617-w.

[64] J. D. Teufel, T. Donner, D. Li, J. W. Harlow, M. S. Allman, K. Cicak, A. J. Sirois, J. D. Whittaker, K. W. Lehnert, and R. W. Simmonds. "Sideband cooling of micromechanical motion to the quantum ground state". In: *Nature* 475.7356 (2011), pp. 359–363. ISSN: 1476-4687. DOI: 10.1038/nature10261. URL: https://doi.org/10.1038/nature10261.

[65] J. D. Teufel, D. Li, M. S. Allman, K. Cicak, A. J. Sirois, J. D. Whittaker, and R. W. Simmonds. "Circuit cavity electromechanics in the strong-coupling regime". In: *Nature* 471.7337 (2011), pp. 204–208. ISSN: 1476-4687. DOI: 10.1038/nature09898. URL: https://doi.org/10.1038/nature09898.

[66] R. J. Thompson, G. Rempe, and H. J. Kimble. "Observation of normal-mode splitting for an atom in an optical cavity". In: *Phys. Rev. Lett.* 68.8 (1992), pp. 1132–1135. DOI: 10.1103/PhysRevLett.68.1132. URL: https://link.aps.org/doi/10.1103/PhysRevLett.68.1132.

[67] K. Tolpygo. "Physical properties of a rock salt lattice made up of deformable ions". In: *Zh. Eksp. Teor. Fiz* 20.3 (1950), pp. 497–509. DOI: 10.1103/PhysRevA.65.032323. URL: https://link.aps.org/doi/10.1103/PhysRevA.65.032323.

[68] M. Toroš and T. S. Monteiro. "Quantum sensing and cooling in three-dimensional levitated cavity optomechanics". In: *Phys. Rev. Research* 2.2 (2020), p. 023228. DOI: 10.1103/PhysRevResearch.2.023228. URL: https://link.aps.org/doi/10.1103/PhysRevResearch.2.023228.

[69] M. Toroš, F. Hales, and T. S. Monteiro. "Coherent-scattering two-dimensional cooling in levitated cavity optomechanics". In: *Phys. Rev. Research* 3.2 (2021), p. 023071. DOI: 10.1103/PhysRevResearch.3.023071. URL: https://link.aps.org/doi/10.1103/PhysRevResearch.3.023071.

[70] E. Verhagen, S. Deléglise, S. Weis, A. Schliesser, and T. J. Kippenberg. "Quantum-coherent coupling of a mechanical oscillator to an optical cavity mode". In: *Nature* 482.7383 (2012), pp. 63–67. ISSN: 1476-4687. DOI: 10.1038/nature10787. URL: https://doi.org/10.1038/nature10787.

[71] V. Vuletić and S. Chu. "Laser Cooling of Atoms, Ions, or Molecules by Coherent Scattering". In: *Phys. Rev. Lett.* 84.17 (2000), pp. 3787–3790. DOI: 10.1103/PhysRevLett.84.3787. URL: https://link.aps.org/doi/10.1103/PhysRevLett.84.3787.

[72] A. Wallraff, D. I. Schuster, A. Blais, L. Frunzio, R.-. S. Huang, J. Majer, S. Kumar, S. M. Girvin, and R. J. Schoelkopf. "Strong coupling of a single photon to a superconducting qubit using circuit quantum electrodynamics". In: *Nature* 431.7005 (2004), pp. 162–167. ISSN: 1476-4687. DOI: 10.1038/nature02851. URL: https://doi.org/10.1038/nature02851.

[73] X.-L. Wang, X.-D. Cai, Z.-E. Su, M.-C. Chen, D. Wu, L. Li, N.-L. Liu, C.-Y. Lu, and J.-W. Pan. "Quantum teleportation of multiple degrees of freedom of a single photon". In: *Nature* 518.7540 (2015), pp. 516–519. ISSN: 1476-4687. DOI: 10.1038/nature14246. URL: https://doi.org/10.1038/nature14246.

[74] C. Weisbuch, M. Nishioka, A. Ishikawa, and Y. Arakawa. "Observation of the coupled exciton-photon mode splitting in a semiconductor quantum microcavity". In: *Phys. Rev. Lett.* 69.23 (1992), pp. 3314–3317. DOI: 10.1103/PhysRevLett.69.3314. URL: https://link.aps.org/doi/10.1103/PhysRevLett.69.3314.

[75] D. Windey, C. Gonzalez-Ballestero, P. Maurer, L. Novotny, O. Romero-Isart, and R. Reimann. "Cavity-Based 3D Cooling of a Levitated Nanoparticle via Coherent Scattering". In: *Phys. Rev. Lett.* 122.12 (2019), p. 123601. DOI: 10.1103/PhysRevLett.122.123601. URL: https://link.aps.org/doi/10.1103/PhysRevLett.122.123601.

[76] E. E. Wollman, C. U. Lei, A. J. Weinstein, J. Suh, A. Kronwald, F. Marquardt, A. A. Clerk, and K. C. Schwab. "Quantum squeezing of motion in a mechanical resonator". In: *Science* 349.6251 (2015), pp. 952–955. ISSN: 0036-8075. DOI: 10.1126/science.aac5138. eprint: https://science.sciencemag.org/content/349/6251/952.full.pdf. URL: https://science.sciencemag.org/content/349/6251/952.

[77] T. Yoshie, A. Scherer, J. Hendrickson, G. Khitrova, H. M. Gibbs, G. Rupper, C. Ell, O. B. Shchekin, and D. G. Deppe. "Vacuum Rabi splitting with a single quantum dot in a photonic crystal nanocavity". In: *Nature* 432.7014 (2004), pp. 200–203. ISSN: 1476-4687. DOI: 10.1038/nature03119. URL: https://doi.org/10.1038/nature03119.